THE UNIVERSITY OF CHICAGO

THERAPEUTIC ULTRASOUND: IMPROVED IMAGE GUIDANCE AND COMBINATORIAL TREATMENTS FOR RECURRENT PROSTATE CANCER

A DISSERTATION SUBMITTED TO
THE FACULTY OF THE DIVISION OF THE BIOLOGICAL SCIENCES
AND THE PRITZKER SCHOOL OF MEDICINE
IN CANDIDACY FOR THE DEGREE OF
DOCTOR OF PHILOSOPHY

COMMITTEE ON MEDICAL PHYSICS

BY
GREGORY JONATHAN ANTHONY

CHICAGO, ILLINOIS
AUGUST 2019

To my family.

Contents

LIST OF FIGURES vii

LIST OF TABLES xv

ACKNOWLEDGMENTS xvii

ABSTRACT xx

CHAPTER 1: INTRODUCTION 1
- 1.1 Treatment of radio-recurrent prostate cancer 1
- 1.2 Therapeutic ultrasound ablation: mechanisms and applications 2
- 1.3 Sonodynamic therapy: mechanisms and applications 3
- 1.4 Transurethral ultrasound ablation as a standalone vs. combinatorial therapy 4
- 1.5 Improving image guidance and evaluation of TULSA 6
- 1.6 Histotripsy as a standalone vs. combinatorial therapy for prostate cancer 7
- 1.7 Improving image guidance and evaluation of histotripsy 8
- 1.8 Innovation and clinical significance 9
  - *1.8.1 Theranostic silica microshell-enhanced TULSA* 9
  - *1.8.2 Histotripsy for Prostate Cancer Ablation with Quantitative Image Guidance* 9
  - *1.8.3 Histotripsy for Sonodynamic Therapy* 10
- 1.9 Dissertation Outline 11

CHAPTER 2: ENHANCEMENT OF MRI-GUIDED TRANSURETHRAL ULTRASOUND ABLATION OF THE PROSTATE WITH SILICA-SHELL PHASE-SHIFT EMULSIONS 13
- 2.1 Introduction 13
- 2.2 Materials and methods 15
  - *2.2.1 Ultrasound phase-shift emulsion formulation* 15
  - *2.2.2 In vitro magnetic resonance imaging* 16
  - *2.2.3 Therapeutic ultrasound therapy system* 17
  - *2.2.4 Pre-treatment procedure* 19
  - *2.2.5 Therapy planning and monitoring* 20
  - *2.2.6 3T image analysis and treatment evaluation* 25
  - *2.2.7 Ex vivo 9.4 T MRI* 27
  - *2.2.8 Histopathological analysis* 28
  - *2.2.9 Statistical analysis* 30
- 2.3 Results 31
  - *2.3.1 In vitro magnetic resonance imaging* 31
  - *2.3.2 Insonation* 32
  - *2.3.3 Histopathology* 33
  - *2.3.4 3T MRI and iSuite* 34

2.3.5 Ex vivo 9.4 T MRI ... 38
2.3.6 Comparison of sUPEs, sUPEs with Optison, and saline sham ... 40
2.3.7 Comparison of lesion areas using histology, DCE MRI, and MR thermometry ... 42
2.4 Discussion ... 44
2.4.1 Transition of sUPEs and MR contrast ... 44
2.4.2 Enhancement of thermal therapy with sUPEs ... 46
2.4.3 MR imaging and thermometry for evaluation of treatment ... 48
2.4.4 Limitations of study ... 51
2.5 Conclusions and future work ... 53

CHAPTER 3: ASSESSMENT OF HISTOTRIPSY-INDUCED LIQUEFACTION WITH DIAGNOSTIC ULTRASOUND AND MAGNETIC RESONANCE IMAGING IN VITRO AND EX VIVO ... 54
3.1 Introduction ... 54
3.2 Materials & Methods ... 55
3.2.1 In vitro phantom preparation ... 55
3.2.2 Phantom preparation with ex vivo liver samples ... 56
3.2.3 Phantom preparation with in vitro blood clot samples ... 57
3.2.4 Insonation and monitoring bubble activity ... 57
3.2.5 Post hoc assessment of liquefaction: Conventional B-mode and MR imaging ... 61
3.2.6 Image registration ... 63
3.2.7 Image analysis ... 65
3.3 Results ... 67
3.3.1 Observation of histotripsy-induced liquefaction ... 67
3.3.2 Monitoring bubble activity with PCI/plane-wave imaging ... 69
3.3.3 Post hoc conventional B-mode imaging: RBC phantoms ... 73
3.3.4 Post hoc conventional B-mode imaging: clot and liver samples ... 73
3.3.5 Post hoc 3T MRI of RBC phantoms ... 73
3.3.6 Post hoc 3T MRI of clot and liver samples ... 74
3.3.7 Image analysis/spatial correlation of red blood cell phantoms ... 77
3.3.8 Image analysis/spatial correlation of clot and liver samples ... 78
3.3.9 Receiver Operating Characteristic (ROC) Analyses ... 82
3.3.10 ROC Analysis: RBC phantoms ... 83
3.3.11 ROC Analysis: Liver samples ... 85
3.3.12 Dice Similarity Coefficient Analysis ... 87
3.4 Discussion ... 88
3.4.1 Observations of phantom/tissue liquefaction ... 88
3.4.2 Prediction of liquefaction via bubble activity ... 89
3.4.3 Post hoc evaluation of liquefaction with MR and conventional B-mode imaging ... 91
3.4.4 Relationship between diagnostic ultrasound, MRI, and liquefaction ... 93
3.4.5 Limitations of study ... 95

3.5 Conclusions and future work 97

CHAPTER 4: ASSESSMENT OF HISTOTRIPSY-MEDIATED PRODUCTION OF REACTIVE OXYGEN SPECIES IN VITRO 99
4.1 Introduction 99
4.2 Materials & Methods 101
4.2.1 Chemical solutions 101
4.2.2 Experimental setup and ultrasound exposure 102
4.2.3 Monitoring and quantification of cavitation 104
4.2.4 Fluorescence measurement 104
4.2.5 Cavitation measurement, correlation with ROS production, and statistical analysis 105
4.3 Results 106
4.3.1 Observation of bubble activity 106
4.3.2 ROS production with varying PNP 108
4.3.3 ROS production with varying sonication parameters 111
4.4 Discussion 113
4.4.1 Generation of ROS by ultrasound exposure 113
4.4.2 Histotripsy exposure of TiO_2 115
4.4.3 Limitations 118
4.5 Conclusions and Future Work 119

CHAPTER 5: CONCLUSIONS 121
5.1 Overview of Work 121
5.2 Enhancement of TULSA Therapy with sUPEs 122
5.3 Multi-modal imaging assessment of histotripsy ablation 123
5.4 Histotripsy-mediated production of ROS 124
5.5 Future work 125

REFERENCES 128

LIST OF FIGURES

Figure 1.1. Diagram of TULSA thermal therapy.[35] A rotating unfocused array delivers acoustic energy to thermally ablate the entire prostate gland. MR thermometry feedback automatically modulates the device output and rotational speed. 5

Figure 1.2. Diagram of formulation and activation of sUPE. Ultrasound exposure transitions the internal perfluorocarbon to a gas, causing expansion and rupturing of the silica shell. If the sUPE carries a payload (in this case, an MR contrast agent Gd_2O_3), it is then released to interact with the surrounding medium.[82].. 6

Figure 1.3. Diagram summarizing the work presented in this dissertation. 12

Figure 2.1. (A) Top down schematic of the ultrasound therapy system components inside the MRI scanner room, and dimensions of TULSA applicator. Device output and rotation was controlled from the scanner control area to apply static insonations to injection sites. The coolant hoses connect to a pump in the scanner control area. The RF filter box connects to the ultrasound generator and controller PC. (B) Photograph of scanner room just prior to TULSA procedure. An anterior body surface coil was used in conjunction with the posterior coil embedded in the scanner table.. 18

Figure 2.2. Orthogonal *in vivo* 3T MR images [(A) axial, (B) coronal and (C) sagittal] showing placement of ultrasound applicator using iSuite interface. MR scan parameters for this 2D bTFE sequence are given in Table 2.1. iSuite guidance was used to ensure positioning of the applicator at the proper depth in the prostatic urethra. The colored lines in each image indicate the cross-sections of the orthogonal image planes. Orientation is denoted by the colored square in the upper-left corner of each frame (red=axial, green=coronal, blue=sagittal). The three image planes are centered on the ultrasound applicator, as indicated in (D) the 3D reconstruction of the dataset. 21

Figure 2.3. Orthogonal *in vivo* 3T MR images [(A) axial, (B) coronal and (C) sagittal] from iSuite interface showing insertion of biopsy needle for particle injection into the prostate. MR scan parameters for this 2D bTFE sequence are given in Table 2.1. iSuite was used to guide needle insertion and confirm accurate placement of the needle tip in the prostate. The three image planes are centered on the needle tip, indicated by the yellow arrow in (C). A 3D reconstruction of the dataset (D) is also rendered... 23

Figure 2.4. *In vivo* treatment planning, monitoring, and evaluation using the iSuite interface at 3T. MR scan parameters for (A, D) the 2D bTFE sequence and (B, C, E, F) the 2D FFE temperature mapping sequence are given in Table 2.1. (A, D) Placement of treatment marker

(red sphere) at injection site using bTFE images, (B, E) real-time thermography images acquired during therapy (scale = 37–80°C), and (C, F) post-treatment thermal dose maps (scale = 0–240 CEM_{43}) for a lesion in (A, B, C) axial and (D, E, F) oblique-sagittal planes. The crosshairs in frames B and E are centered on the transducer, whose elements are aimed upward in frames B and C and to the left in frames E and F. 24

Figure 2.5. Timeline of typical canine experiment, including setup, injections, treatments, and image acquisitions. All post-treatment images were acquired 5 minutes after temperatures in the treatment zone had returned to 37–39°C. 3T MR scan parameters are given in Table 2.1. 25

Figure 2.6. T_1-map of agarose suspensions of UPEs in intact and ruptured states, at the same overall Gd concentrations. A reference dilution series of the clinical Gd contrast agent (Omniscan) in agarose is included for reference. Intact UPEs show minimal T_1-relaxivity, while ruptured UPEs show even greater T_1-relaxivity than clinical MR contrast agent. 32

Figure 2.7. H&E stained histologic slides from central slices of (A) subject 5 and (C) subject 6. Coagulative necrosis zones (outlined with dashed blue marker) were apparent as pale regions (yellow arrow in D) that sometimes surrounded heat-fixed areas, where little to no epithelial sloughing or cell death was apparent (red arrow in D). Near-complete cell death and epithelial sloughing were visible in non-heat-fixed coagulative necrosis zones. A hemorrhagic area is visible as a magenta-stained region (yellow arrow in B). 34

Figure 2.8. 3T *in vivo* T_1W and T_2W images of the prostate before and after therapy. MR scan parameters for (A, B) the T_1W TSE sequence and (C-F) the T_2W TSE sequence are given in Table 2.1. T_1W images acquired immediately (A) before and (B) after treatment and cooldown period, and T_2W images acquired immediately (C) before and (D) after treatment and cooldown period for a different insonation are shown. Some enhancement is visible in the treatment area in the post-therapy T_1W image, as indicated by the yellow arrow in (B). Signal enhancement is seen in the inflamed periphery of the treatment zone in the post-therapy T_2W image (D, yellow arrow), while the center of the lesion is relatively hypointense (D, red arrow). (E) Post-injection T_2W image showing the injection bolus of sUPEs with Optison as a small hyperintense region (yellow arrow). All post-therapy imaging was acquired 5 minutes after MR thermometry indicated the treatment zone had returned to 37-39°C. 37

Figure 2.9. 3T *in vivo* post-treatment imaging and histology for evaluation of therapy. MR scan parameters for (A) the DCE 3D FFE sequence, (B) the DWI EPI sequence, and (D) the 2D FFE temperature mapping sequence are given in Table 2.1. (A) DCE image: Region of non-perfusion is noted via a red arrow. Enhancing rim surrounding the lesion is noted via a yellow arrow. (B) ADC map (scale 0 - 3 mm^2/ms): Restricted diffusion is marked by a yellow arrow. Small region of unaffected diffusion (possibly indicating thermal fixation) is marked by a red arrow. (C) H&E

stained prostate section: Area of thermal fixation at center of lesion with normal stained appearance is indicated by a red arrow. The area of apparent coagulative necrosis (non-heat-fixed) is characterized by a pale color and exhibits epithelial cell sloughing and death, indicated by a yellow arrow. (D) Thermal dose map (scale 0 - 240 CEM_{43}): Dark red corresponds to a dose of 240 CEM_{43} or greater. Treatment arm is sUPEs only. All post-therapy imaging was acquired 5 minutes after MR thermometry indicated the treatment zone had returned to 37-39°C............... 38

Figure 2.10. 9.4T *ex vivo* MRI images of canine prostate after *in vivo* treatment. MR scan parameters for (A) the T_2W TURBO-RARE sequence, (B) the T_2 mapping MSME sequence, (C) the DWI sequence, (D) the T_1W FLASH sequence, and (E) the T_1 mapping VTR RARE sequence are given in Table 2.2. (A) T_2W TURBO-RARE image, (B) T_2 map (scale 0 – 120 ms), (C) ADC-map (scale 0 - 2 mm^2/ms), (D) T_1W FLASH image, (E) T_1 map (scale 0 - 2,500 ms), and (F) H&E stained histological slide of the same axial prostate section. The three lesions are located roughly at the 5 o’ clock (sUPE with Optison injection), 7 o’ clock (sUPE injection), and 11 o’ clock (saline sham injection) positions in the prostate, indicated by the red arrows in panel F. The red arrows in panel C indicate lesions with rims of reduced ADC surrounding central regions of unchanged ADC; the yellow arrow indicates a lesion with uniformly reduced ADC. 40

Figure 2.11. Comparison of treatments administered with saline, sUPEs only, and sUPEs with Optison. (A) Largest CNR in lesion ROI over all axial slices, as defined in equation (1). (B) Histological lesion size at most prominent axial slice. Red lines indicate medians, and blue boxes indicate interquartile ranges for each treatment group. Data points from the same canine are connected with black lines. No significant differences were observed between the three groups for CNR or lesion size. Only canines receiving all three treatments are included. 41

Figure 2.12. Comparison of $\boldsymbol{TEq}$ as defined in equation (3) for treatments administered with saline, sUPEs only, and sUPEs with Optison. Red lines indicate medians, and blue boxes indicate interquartile ranges for each treatment group. Data points from the same canine are connected with black lines. No significant differences were observed between the three groups. Only canines receiving all three treatments are included. 41

Figure 2.13. Correlation of measured ablative areas from histology and 3T *in vivo* MR imaging estimates. (A) Non-perfused area in DCE images as a function of histological lesion area. (B) Area within 55°C isotherm as a function of histological lesion area. (C) Area of thermal dose ≥ 240 CEM_{43} as a function of histological lesion area. Slopes of linear fits are given as the fitted slope and 95% confidence interval (in brackets). Error bars in histological areas and NPAs are standard deviations of triplicate measurements. Error bars in 55°C isotherms and thermal dose measurements were computed by propagating the temperature uncertainty, as described in the methods. Only canines receiving all three treatments are included.. 44

Figure 3.1. Top-down view of experimental setup for phantoms containing (a) red blood cell layers, (b) liver samples, and (c) clot samples. Three locations were targeted with the therapy source (shown in gray on the left) in each phantom, separated by 1.5 cm. In red blood cell phantoms, agarose was poured in layers, with thin blood cell layers (red lines) applied via pipette on top of each solidified agarose layer. Additional fiducial markers (indicated by blue dotted lines) were used to orient the diagnostic ultrasound images, magnetic resonance (MR) images, and collected histologic samples parallel to the direction of ultrasound propagation. 59

Figure 3.2. (a) Side view of experimental setup for red blood cell (RBC) phantom insonation with a therapeutic ultrasound transducer. RBC layers of the phantoms were oriented parallel to the direction of ultrasound propagation from the histotripsy source. Fiducial markers embedded within the agarose were used to register diagnostic ultrasound and magnetic resonance (MR) images to digital photographs of phantoms post-insonation. The imaging plane of the L11-4v imaging array was registered to the RBC layers and visualized bubble activity along the acoustic axis of the histotripsy source. (b) Timeline of all image data acquisition. Passive and plane wave acquisitions were acquired every tenth histotripsy pulse due to data transfer rate limitations. Post hoc conventional B-mode images were acquired within 1 min of the histotripsy insonation. Samples were transferred to the MR scanner within 10 min, and MR images were acquired over the course of 1 hour... 60

Figure 3.3. Demonstration of Otsu thresholding to generate binary mask of liquefaction zone. Red-green-blue images (a) are converted to grayscale and a global threshold is determined based on the gray level histogram to generate a binary image (b)... 64

Figure 3.4. Gross observations (top row) and post hoc visualizations of liquefaction zones with conventional B-mode images (middle row) and T_2-weighted images (bottom row). Insonations consisted of 13 (left) 17 (middle-left), 21 (middle-right), or 25 (right) MPa peak negative pressure pulses of 5-μs pulse duration and 1-MHz fundamental frequency in red blood cell phantoms. Therapeutic ultrasound pulses propagated from left to right in all images. In post-insonation conventional B-mode images, fiducial markers have been removed to allow better grayscale windowing for visualization of hypoechoic liquefaction zones. 68

Figure 3.5. Plane wave ultrasound images (top row) and passive cavitation images (bottom row) acquired during histotripsy insonation with 13 (left) 17 (middle-left), 21 (middle-right), and 25 (right) MPa peak negative pressure pulses of 5-μs pulse duration and 1-MHz fundamental frequency in red blood cell phantoms. Therapeutic ultrasound pulses propagated from left to right in all images.. 70

Figure 3.6. Registration of imaging with gross observation of red blood cell phantom liquefaction. (a) Gross observation of liquefaction generated by histotripsy in a red blood cell

phantom with the liquefaction zone outlined in green, (b) coregistration of passive cavitation imaging (PCI) acoustic power and red blood cell liquefaction, (c) coregistration of plane wave grayscale and red blood cell liquefaction, (d) parametric T_2 map of red blood cell liquefaction, (e) coregistration of PCI acoustic power and T_2 map, and (f) coregistration of plane wave grayscale and T_2 map. The liquefaction zone outline is shown in panels (a), (b), and (c). The histotripsy pulse (1-MHz fundamental frequency, 5-µs pulse duration, 17-MPa peak negative pressure) propagated from left to right in the image. The azimuth/range dimensions of the diagnostic ultrasound imaging plane are indicated in panel (a). 70

Figure 3.7. Registration of imaging with histologic observation of blood clot sample liquefaction. (a) H&E-stained treated blood clot sample, (b) coregistration of passive cavitation imaging (PCI) acoustic power and H&E-stained clot sample, (c) coregistration of plane wave grayscale and H&E-stained clot sample, (d) parametric T_2 map of treated clot sample, (e) coregistration of PCI acoustic power and T_2 map, (f) coregistration of plane wave grayscale and T_2 map, (g) parametric T_1 map of treated clot sample, (h) coregistration of PCI acoustic power and T_1 map, and (i) coregistration of plane wave grayscale and T_1 map. The histotripsy pulse (1-MHz fundamental frequency, 5-µs pulse duration, 18-MPa peak negative pressure) propagated from left to right in the image. The azimuth/range dimensions of the diagnostic ultrasound imaging plane are indicated in the panel (a). The most hyperechoic pixels in the plane wave images, corresponding to reflections from the top and bottom of the clot, have been removed for better windowing and visualization of the histotripsy bubble cloud. 71

Figure 3.8. Registration of imaging with histologic observation of liver sample liquefaction. (a) Hematoxylin and eosin (H&E) stain of liver sample exposed to histotripsy with the ablation zone indicated by the dotted black outline, (b) coregistration of passive cavitation imaging (PCI) acoustic power and H&E-stained liver sample, (c) coregistration of plane wave grayscale and H&E-stained liver sample, (d) parametric T_2 map of treated liver sample, (e) coregistration of PCI acoustic power and T_2 map, (f) coregistration of plane wave grayscale and T_2 map, (g) parametric apparent diffusion coefficient (ADC) map of treated liver sample, (h) coregistration of PCI acoustic power and ADC map, and (i) coregistration of plane wave grayscale and ADC map. The histotripsy pulse (1-MHz fundamental frequency, 5-µs pulse duration, 25-MPa peak negative pressure) propagated from left to right in the image. The azimuth/range dimensions of the diagnostic ultrasound imaging plane are indicated in the panel (a). Reflections from connective tissue in (c), (f), and (i) have been removed for better windowing and visualization of the histotripsy bubble cloud. 72

Figure 3.9. (a) Hematoxylin and eosin (H&E) stain, (b) post hoc conventional B-mode image, and (c) T_2-weighted image of liquefaction in the same liver sample. The liquefaction zone (dotted black dotted outline in (a), red arrows) can be distinguished as hypoechoic in (b) and hyperintense in (c). Regions of more thorough liquefaction exhibit minimal H&E staining,

(yellow arrow in (a)). Small hyperechoic structures can be seen in the post hoc conventional B-mode image (yellow arrows in (b)), possibly indicating residual bubbles or accumulations of cellular debris. The histotripsy pulse (1-MHz fundamental frequency, 5-µs pulse duration, 25-MPa peak negative pressure) propagated from left to right in each image. 76

Figure 3.10. Examples of parametric (a) T_1, (b) T_2, and (c) apparent diffusion coefficient (ADC) maps for red blood cell phantoms. The liquefaction zone is indicated by a red arrow in (a) and (b). The red blood cell layer (dark area) is indicated by yellow arrows in (a) and (b). The histotripsy pulse (1-MHz fundamental frequency, 5-µs pulse duration, 17-MPa peak negative pressure) propagated from left to right in each image. 77

Figure 3.11. Normalized amplitudes of passive cavitation imaging (PCI) acoustic power, plane wave grayscale, and change in T_2 from background along the central axis of the liquefaction zone (dashed blue line in top images) for (a) a red blood cell (RBC) phantom, and (b) a liver sample. The locations of liquefaction are binarized for the bottom plots, with values of 1 indicating liquefaction and 0 indicating intact media. The areas of greatest change in T_2 in the RBC phantom (black arrows) correspond to areas of relatively low PCI power and plane wave grayscale intensity (red arrow) within the liquefaction zone. In the liver sample, locations of T_2 and apparent diffusion coefficient maxima (black dashed arrows) correspond with more thorough liquefaction as indicated by Hematoxylin and eosin staining (yellow dashed arrow). Two maxima are present for PCI power (red dashed arrows) and plane wave grayscale (gray dashed arrows). The proximal (leftmost) plane wave grayscale peak is small compared with the distal (rightmost) peak, while the larger proximal PCI peak more accurately reflects the increased liquefaction and magnetic resonance parameter changes in this location. The histotripsy pulse (1-MHz fundamental frequency, 5-µs pulse duration, 17-MPa peak negative pressure for RBC phantom, 25-MPa peak negative pressure for liver sample) propagated from left to right in each image. 80

Figure 3.12. Normalized amplitudes of passive cavitation imaging (PCI) acoustic power, plane wave grayscale, and change in T_2 from background at the azimuth position of maximum PCI power (vertical dashed blue lines in right-side images) for (a) a red blood cell phantom, and (b) a liver sample. Apparent diffusion coefficient signals in red blood cell phantoms and T_1 and plane wave grayscale signals in all samples were dominated by noise and thus excluded from this figure. The locations of liquefaction are binarized for the plots, with values of 1 indicating liquefaction and 0 indicating intact media. The azimuthal location of maximum PCI power in the liver sample corresponds with more thorough liquefaction as indicated by hematoxylin and eosin staining (yellow dashed arrow). The histotripsy pulse (1-MHz fundamental frequency, 5-µs pulse duration, 17-MPa peak negative pressure for RBC phantom, 25-MPa peak negative pressure for liver sample) propagated from left to right in each image. 81

Figure 3.13. Azimuthal position of proximal edge of liquefaction zone (solid black bars), maximum passive cavitation imaging (PCI) acoustic power (solid red bars), plane wave grayscale (checkered blue bars), and maximum (striped orange bars) and minimum (cross-hatched green bars) T_2 for all pressures applied to red blood cell phantoms. Colored bars cover 25% to 75% quantiles, and error bars extend to maximum and minimum azimuthal positions recorded for each parameter. 90 mm corresponds to the geometric focus of the histotripsy source. Locations of maximum PCI acoustic power and T_2 shift proximally with increasing pressure, while plane wave maxima and T_2 minima shift distally. 82

Figure 3.14. Receiver Operating Characteristic (ROC) curves obtained from (a) red blood cell phantoms and (b) liver samples. Quantitative plane wave grayscale (gray dotted line), passive cavitation imaging acoustic power (red solid line), apparent diffusion coefficient (black dashed line), T_1, (gray solid line), T_2, (brown dash-dot line), and post hoc conventional B-mode grayscale (blue dotted line) were used to predict presence of liquefaction/necrosis along azimuth dimension of histotripsy lesions across all peak negative pressures of the histotripsy pulse (only 1 pressure level was employed in the liver studies). The black dotted line indicates the resulting ROC curve from random guessing (area under the curve = 0.5). 83

Figure 3.15. Gross digital photograph of liquefaction zone in a red blood cell phantom. The histotripsy pulse (1-MHz fundamental frequency, 5-μs pulse duration, 13-MPa peak negative pressure) propagated from left to right in the image. Discontinuous liquefaction regions along the periphery of the focal zone (white arrows) may indicate sites of persistent bubble clouds. 89

Figure 4.1. Top-down diagram of experimental setup for sonication and imaging of pipette sample. The histotripsy source is focused on the center of the disposable polyethylene pipette, which translates vertically (in and out of the page) between each set of pulses. The imaging array is positioned orthogonally to the therapeutic source to capture a cross-sectional image of the pipette. A conventional scan line B-mode image was acquired prior to each set of pulses. During sonication, passive cavitation images were acquired every 10th trigger pulse........................... 103

Figure 4.2. Calibration curve (black fitted line) for fluorescence measurement of 2-hydroxyterephthalic acid (HTA) over the range of concentrations observed in this study. 105

Figure 4.3. (a) Scan line B-mode image acquired prior to sample sonication showing the polyethylene pipette outline (total TA volume 1 mL, Thermo Scientific; bulb dimensions: diameter = 12 mm, length = 15.4 cm, thickness = 0.35 ± 0.05 mm); (b) Coregistration of B-mode image of the pipette with passive cavitation image. 107

Figure 4.4. Total PCI acoustic power measured from passive cavitation images as a function of peak negative pressure for sonicated TA solutions with (red bars) and without (blue bars) TiO_2 particles. 108

Figure 4.5. Emission spectra of 2 mM terephthalic acid samples with (dashed lines) and without (solid lines) TiO_2 particles, sonicated with pulses of 24–39 MPa peak negative pressure (5-cycle pulse duration, 1-MHz fundamental frequency, 20 Hz pulse repetition frequency). Spectra were averaged over n = 3–5 samples per pressure level (see table 4.1). The spectra of corresponding control samples (unsonicated 2 mM TA or unsonicated, centrifuged 2 mM TA with 0.35 mg/mL TiO_2) were subtracted to better visualize the emission peak. 109

Figure 4.6. 2-hydroxyterephthalic acid (HTA) generation as a function of peak negative pressure for sonicated TA solutions with (red bars) and without (blue bars) TiO_2 particles. No significant differences in HTA concentration between particle and non-particle samples were observed at any pressure level. HTA concentration increased significantly with each change in peak negative pressure. 110

Figure 4.7. Concentration of 2-hydroxyterephthalic acid (HTA) as a function of the total acoustic power measured from passive cavitation images. Samples with (blue stars) and without (red circles) TiO_2 sonicated with 5-cycle, 20 Hz PRF pulses of 24–39 MPa peak negative pressure. 110

Figure 4.8. Emission spectra of 2 mM terephthalic acid samples with (dashed lines) and without (solid lines) TiO_2 particles, sonicated with 5- or 20-cycle (5 C, 20 C) pulses of 20 or 100 Hz PRF and 29 MPa peak negative pressure. Spectra were averaged over n = 3–5 samples per pressure level (see table 4.1). The spectra of corresponding control samples (unsonicated 2 mM TA or unsonicated, centrifuged 2 mM TA with 0.35 mg/mL TiO_2) were subtracted to better visualize the emission peak. 112

Figure 4.9. 2-hydroxyterephthalic acid (HTA) generation as a function of sonication parameters for sonicated TA solutions with (red bars) and without (blue bars) TiO_2 particles. When considering particle and non-particle samples individually, each set of sonication parameters resulted in a significantly different concentration of HTA. The asterisk (*) indicates a significant difference between particle and non-particle samples. 112

LIST OF TABLES

Table 2.1: MR imaging sequence scan parameters for treatment planning, monitoring, and evaluation acquired on a 3T MRI scanner. 22

Table 2.2: MRI scan parameters for *ex vivo* imaging at 9.4T. 28

Table 2.3: Errors in histological lesion size (standard deviation of triplicate measurements), T_1 CNR (standard deviation in CNR over slices with apparent T_1 enhancement), and fitted parameter T_{Eq} (standard deviation over all fitted pixels). 29

Table 2.4: Lesion areas as determined by thermal dose, 55°C isotherms, DCE NPAs, and histology. 30

Table 2.5: Details of experimental and injection parameters for each procedure. 33

Table 2.6: Key qualitative observations from histology, *in vivo* post-therapy imaging, and *ex vivo* imaging for each treatment. 36

Table 2.7: Lesion areas as determined by histology, DCE NPAs, 55°C isotherms, and thermal dose. 42

Table 2.8: Pearson correlation coefficients (r) from tests of correlation between lesion sizes from histology, DCE NPAs, 55°C isotherms, and thermal dose measurements. 43

Table 3.1: MR scan parameters used for 3T imaging and parametric mapping of T1, T2, and ADC. 63

Table 3.2: Diagnostic ultrasound and MR parameter values measured within liquefaction zones for RBC phantoms insonated at peak negative pressures of 13, 17, 21 and 25 MPa, liver samples insonated at 25 MPa, and clot samples insonated at 18 MPa. 75

Table 3.3: Area under the Curve (AUC) values calculated for all RBC phantom data, and sensitivities, specificities, accuracies, positive predictive values (PPV), and negative predictive values (NPV) at optimal threshold points for all ROC curves. 84

Table 3.4: Area under the Curve (AUC) values calculated for all liver sample data, and sensitivities, specificities, accuracies, positive predictive values (PPV), and negative predictive values (NPV) at optimal threshold points for all ROC curves. 86

Table 3.5: DSC values ± standard deviations as a function of peak negative pressure and tissue/phantom type. 87

Table 4.1: Number of samples for each insonation condition. 2 mM TA solutions were prepared with and without 0.354 mg/mL of TiO_2 nanoparticles. 103

Table 4.2: Total 2-hydroxyterephthalic acid (HTA) concentrations and HTA generation rates for the two pulse durations and two pulse repetition frequencies tested. All sonications were performed at 29 MPa peak negative pressure. Errors are given as standard deviations. 111

ACKNOWLEDGMENTS

I would like to thank my co-advisors, Dr. Steffen Sammet and Dr. Kenneth Bader, for their unwavering support and confidence. This work would not have been possible without their guidance. The insight and encouragement they provided has helped immeasurably in my growth into a rigorous, independent, and clinically oriented researcher. I am truly grateful for the opportunity to work alongside such outstanding advisors. I also want to thank the members of my thesis committee: Dr. Gregory Karczmar, Dr. Aytekin Oto, and Dr. Patrick La Riviere. Dr. Karczmar provided invaluable insight into the magnetic resonance imaging aspects of this work. Dr. Oto's clinical expertise was instrumental for carrying out such a clinically focused project and for ensuring that the end goals were clinically relevant. Dr. La Riviere provided very helpful insight into the design of the studies described herein, and was a terrific sounding board for developing ideas and presenting research findings coherently.

I acknowledge and thank the iSAIRR Core Facility, the MRIS Research facility, the MRIRC research core, the University of Chicago Animal Resource Center, the Carlson Facility, Bracco Diagnostics, the HTRC core facility, and the BioPhysics core facilities for their support on this project. This work was supported in part by the National Institutes of Health Grants R01HL133334, R25CA132822, R25NS080949, S10OD018448, K12CA139160, U54CA132379, T32EB002103 (Greg Anthony), and T32CA153915 (James Wang), the National Institutes of Health National Cancer Institute under Grant R33CA177449, the Cancer Research Foundation, Nanocyte Medical, the University of Chicago Comprehensive Cancer Center under Grant P30CA014599, a grant of Philips Healthcare, and the Paul C. Hodges Alumni Society of the Department of Radiology at the University of Chicago.

I also wish to acknowledge the many other members of the University of Chicago community for their crucial support in this work. I thank our collaborators, Dr. Andrew Kummel and James Wang, for their effort toward developing and testing our theranostic sUPE particles, and for providing the impetus from which this dissertation developed. I thank Dr. Viktor Bollen for his brilliant expertise and code development, and for helping me through the hands-on work during our *in vitro* histotripsy studies. I would also like to thank Dr. Jeffrey Souris profusely for his invaluable assistance and expertise in planning, executing, and analyzing the sonodynamic therapy experiments. I am especially grateful to Marta Zamora, Dr. Allison Ostdiek, and their veterinary staff for ensuring our canine studies went smoothly. I owe a great deal to Stan Peters, Bruce Jamieson, Dr. Milica Medved, and Dr. Xiaodong Guo for their training and help with operating the clinical MR scanners. I thank Dr. Ari Partanen, Dr. Sascha Krueger, and Steffen Weiss for their technical support throughout our canine studies. I also thank Dr. Tatjana Antic, Terri Li, and the HTRC for the immeasurable help they offered in processing and interpreting our tissue samples. Thank you to Dr. Sean Foxley, Dr. Xiaobing Fan, and Dr. Aritrick Chatterjee for their help in acquiring and processing quantitative MR images. I thank Elena Solomaha for her instruction on using the spectrofluorometer as well. I am grateful to Rene Maldonado for helping to pave the way for the third aim of this dissertation, and to Jane Kelleher and Hunter Thompson for their help in completing and continuing it. Fan Yang taught a wonderful course in biostatistics that greatly helped inform the choice of statistical analysis in this dissertation. I thank the biostatistics core and Chuanhong Liao in particular, as well as Dr. Karen Drukker for their help in refining and confirming my choice of statistical analyses. I also wish to thank Dr. Samuel Armato and Dr. Hania Al-Hallaq for their encouragement and help in turning my first rotation project into a complete, published manuscript.

Finally, I wish to thank my family and friends for their support. I am forever grateful for my parents, Larry and June Anthony, for never failing to remind me of how proud they are and what an impact I have had on their lives. My brother Geoff, sister in-law Mary Beth, and niece Madelyn are a constant source of love, encouragement, and laughter. I thank all of my friends in the GPMP, especially my classmates Corey, Eyjólfur, and Natasha, and my labmate Sam for always brightening the day and offering sound advice. I lastly thank the Histones for giving me an incredible musical outlet and some of the greatest friends I could ask for.

ABSTRACT

Cases of radio-recurrent prostate cancer (PCa) are difficult to treat effectively and would benefit from the advancement of non-invasive, image-guided alternative therapies. Therapeutic ultrasound is a minimally or non-invasive method of tissue ablation. Thermal therapeutic ultrasound can be used to necrose tissue via heat deposition, while mechanical ultrasound ablation, or histotripsy, induces liquefaction of tissue through violent bubble cloud activity. Both thermal and mechanical ultrasound ablation have been applied to treatment of prostate tissue, but with limited therapeutic efficacy. Ultrasound exposure can be used to non-invasively improve the uptake and distribution of therapeutics, and can act on sonodynamic therapy (SDT) agents to generate cytotoxic reactive oxygen species (ROS). The combination of therapeutic ultrasound with therapeutic agents may improve treatment outcomes in radio-recurrent PCa patients. Clinical translation of therapeutic ultrasound is also limited by the image-guidance methods currently available. Improved imaging metrics are needed to better plan, treat, and evaluate thermal ultrasound ablation and histotripsy, as well as to quantify the release of drugs or generation of ROS during SDT.

The first aim of this dissertation examined a novel theranostic nanoparticle for improved image guidance and therapeutic efficacy in thermal ultrasound ablation of the prostate. This particle’s capacity for accelerating ultrasound-induced heating, delivery of a therapeutic payload, and magnetic resonance (MR) image contrast were explored. This dissertation’s second aim evaluated multi-modal image guidance methods for histotripsy therapy using agarose phantom, porcine liver, and human blood clot models. The ability of several diagnostic ultrasound and MR image modalities to assess liquefaction of phantoms or tissue was evaluated. Finally, the third aim of this dissertation explored the use of histotripsy to generate sonochemical reactions for

SDT. In addition to quantifying the amount of ROS produced by histotripsy exposure with and without sonosensitizing agents, passive cavitation imaging (PCI) was tested as a quantitative dose metric for SDT.

The theranostic nanoparticle explored in Aim 1 was found to enhance heating, but did not adequately release its contrast payload, indicating limited utility as an MR contrast agent or drug-delivery vehicle. The particle did not confound guidance and evaluation of the therapy with MR imaging. The second aim of this dissertation showed PCI to best predict the location of sample liquefaction, whereas MR imaging provided the most accurate delineation of the ablation zone. MR imaging parameters exhibited more drastic changes following liquefaction of tissue compared with agarose phantom. The third aim of this thesis demonstrated that ROS production increased with the peak negative pressure of ultrasound exposures, and scaled linearly with the acoustic power measured via PCI. Exposure of titanium dioxide (TiO_2) nanoparticles to histotripsy did not significantly increase the amount of cavitation emissions observed or the quantity of ROS produced, suggesting limited efficacy of histotripsy in sonoactivation of TiO_2. The studies carried out in this thesis have indicated several potential improvements of therapeutic efficacy and image guidance in therapeutic ultrasound and sonodynamic therapy. These contributions may help facilitate the clinical translation of therapeutic ultrasound technologies for treatment of PCa and other pathologies.

CHAPTER 1

INTRODUCTION

1.1 Treatment of radio-recurrent prostate cancer

Prostate cancer is a major burden on global health. Approximately 1,276,000 new cases and nearly 400,000 deaths were anticipated globally in 2018.[1] Treatment plans for prostate cancer range from whole-gland surgical resection or irradiation[2, 3] to active surveillance,[4] depending on the disease stage and prognosis. Cases of localized (T1–T3), but aggressive (i.e. Gleason score ≥ 7) prostate cancer typically warrant intervention, and prostate whole-gland radiotherapy is employed as the primary treatment in 60,000 new prostate cancer diagnoses in the United States annually.[5–7] Up to 20,000 of these patients will experience locally recurrent disease after treatment,[6–10] in addition to possible treatment comorbidities affecting urinary, sexual, or bowel function.[11] Hormonal therapy is the treatment of choice for radio-recurrent prostate cancer,[12, 13] but only acts to delay disease progression.[14] Even in the short term, hormone therapy is ineffective for 20% of patients, and is associated with deleterious effects such as osteoporosis and cardiovascular disease.[5, 7] Radical prostatectomy is another option for salvage treatment of recurrent prostate cancer, but is highly invasive and concurrent with significant treatment comorbidities.[15, 16] Cryoablation has been employed as a focal salvage treatment for recurrent prostate cancer,[9] but incidences of incontinence and erectile dysfunction remain high with this modality.[17] Recurrent prostate cancer is often chemo-resistant, and clinically effective doses of chemotherapy are prohibited by systemic side effects and toxicities.[18–20] Chemotherapy is thus generally reserved for castration-resistant, metastatic disease.[21] Encapsulation of chemotherapeutics in nanocarriers such as liposomes, micelles, polymers, or silica particles is an attractive non-invasive treatment approach because it enables targeted treatment of cancerous tissue, decreasing systemic side effects and increasing antitumor activity compared to non-encapsulated formulations.[22–27] However, drugs encapsulated in nanocarriers do not permeate throughout the entire target volume, reducing treatment efficacy.[28, 29] The optimal treatment strategy for recurrent prostate cancer remains a subject of debate, and a paucity of safe, reliable therapies strongly motivates the development of alternative or adjuvant therapeutic options.

1.2 Therapeutic ultrasound ablation: mechanisms and applications

Minimally invasive procedures aim to reduce morbidity and complications involved in the treatment of disease. Therapeutic ultrasound is a non-invasive or minimally invasive treatment modality that can achieve these goals to generate bioeffects in tissue, including ablation. Continuous wave insonations achieve thermal necrosis of target tissue via deposition of ultrasound energy as heat.[30] Thermal ablation with therapeutic ultrasound has been used in the treatment of malignant and benign tissues in the prostate, uterus, liver, breast, kidney, bone, pancreas, and soft-tissue sarcoma.[31–33] Real-time temperature feedback with MR thermometry[34] allows automation of treatment delivery.[35, 36] However, thermal ultrasound ablation techniques are limited by long treatment times[37] and imprecise or inconsistent ablation of highly perfused tissue.[38, 39] Histotripsy is an alternative form of therapeutic ultrasound that achieves ablation via short-duration, nonlinear pulses that nucleate energetic bubble clouds.[40–42] The mechanical action of these bubbles disintegrates cell nuclei and the extracellular matrix, resulting in a precise zone of liquefied tissue.[43–46] Furthermore, histotripsy-induced bubble activity can be monitored in real time with diagnostic ultrasound, and the resulting tissue homogenization can be evaluated with diagnostic ultrasound and MR imaging.[47–56] Although primarily in pre-clinical stages, histotripsy applications include treatment of prostate tissue, liver cancers, thrombosis, renal carcinomas and calculi, and stimulation of anti-tumor immune responses.[44]

1.3 Sonodynamic therapy: mechanisms and applications

Sonodynamic therapy (SDT) is an emerging therapeutic modality involving the exposure of sonosensitizing agents to cavitational ultrasound, inducing the generation of cytotoxic reactive oxygen species (ROS).[57] Upon ultrasound sonication of sufficient rarefactional pressure in a target, bubbles are formed via expansion of nanoscale gas nuclei in the medium (or exogenous microbubbles introduced into the medium), then collapse violently in a process known as inertial cavitation.[58, 59] The collapsing bubbles act on sonosensitizing agents through unknown mechanisms to stimulate substantial production of ROS. One theory suggests that sonoluminescence, or the emission of light pulses likely caused by recombination of the reactive oxygen species generated by cavitation activity, stimulates the photosensitivity of the sensitizing agents. SDT is a promising therapeutic modality due to the simple transformation of photosensitizers used in photodynamic therapy (PDT) into sonosensitizers. SDT is also better suited to treating non-superficial tumors, owing to the improved penetration of ultrasound in tissue compared with light. The ROS generated by SDT are lethal to cells through a range of mechanisms, depending on the half-life of the specific ROS. Hydroxyl radicals (•OH) and hydrogen atoms (•H) react quickly with dissolved organic compounds, whereas peroxyl and alkoxyl radicals are more likely to diffuse into cells and react within. These reactions can cause protein denaturation and disruption of cellular or mitochondrial membranes, inducing apoptosis.

Sonodynamic therapy has been applied pre-clinically in a number of tumor models, including colon,[60] mammary,[61, 62] and prostate cancers.[63] Further case studies in human subjects indicate extended survival for most patients and minimal toxicity from sonosensitizing agents. Collectively, these studies suggest an ultrasound pressure threshold, indicating inertial cavitation plays a major role in the SDT mechanism, as well as antiangiogenic and antitumor immune responses to the therapy.[57] Some of the major limitations of SDT include insufficient tumor-specific accumulation of sensitizers and inconsistent cavitation effects, even when using the same sonication parameters. Targeted sensitizers conjugated with microbubbles could improve accumulation (and visualization via ultrasound imaging) of sensitizers in target tissue. Manganese, gadolinium, or iron-oxide sensitizers allow for visualization with MRI; alternatively, PET tracers can be conjugated to sensitizers and microbubbles for visualization. Ultrasound imaging techniques may also provide better monitoring and quantification of cavitation bubble activity during SDT, enabling more repeatable treatments.

1.4 Transurethral ultrasound ablation as a standalone vs. combinatorial therapy

Magnetic resonance (MR) imaging-guided transurethral ultrasound ablation (TULSA) is a method of thermal ablation of prostate tissue (Figure 1.1).[64, 65] The unfocused sources used in TULSA are capable of treating entire prostates in less than one hour. MR thermometry feedback allows automation of the procedure and ensures accurate delivery of the ultrasound energy.[35, 36, 66] Furthermore, TULSA is better suited to treating anteriorly located lesions and large prostates when compared with transrectal ultrasound treatment approaches.[67] Application of TULSA to healthy prostate tissue in pre-clinical studies has proven effective, with minimal damage to critical structures adjacent to the prostate.[35, 68, 69] However, the use of TULSA in a pivotal trial has noted residual cancer in 35% of patients[70]. One attractive option to enhance the efficacy of TULSA is a combinatorial therapy using encapsulated chemotherapeutics. Compared with single-modality approaches, treatments combining therapeutic ultrasound with chemotherapeutic agents have been shown to improve the treatment profile *in vitro*[71, 72] and *in vivo*.[73–75] Heat deposition from TULSA insonation can also increase blood perfusion, vascular permeability, and interstitial micro-convection in the tissue, improving delivery of encapsulated drugs.[76] Ultrasound-triggered phase-shift emulsions (sUPEs) are composed of a stabilizing silica shell surrounding a metastable perfluorocarbon liquid that transitions to a gas bubble upon ultrasound exposure (Figure 1.2). Phase shift emulsions can act as drug-delivery vesicles,[77] as well as enhance the effects of therapeutic ultrasound.[77–80] Increased stability and longevity *in vivo*[81] and enhanced retention time in tumor tissue[77, 78] were observed for sUPEs compared with microbubbles or other nanodroplet formulations. As such, sUPEs have great potential as a therapeutic agent to combine with TULSA.

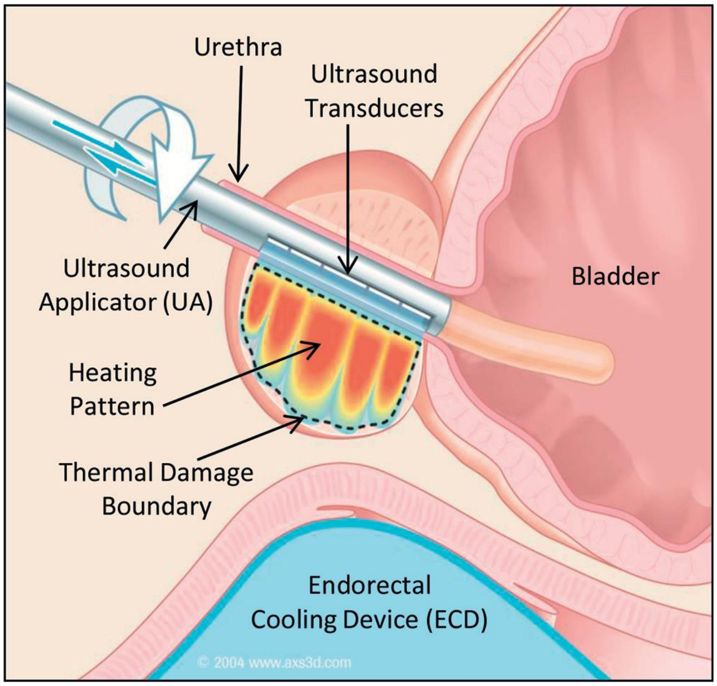

Figure 1.1. Diagram of TULSA thermal therapy.[35] A rotating unfocused array delivers acoustic energy to thermally ablate the entire prostate gland. MR thermometry feedback automatically modulates the device output and rotational speed.

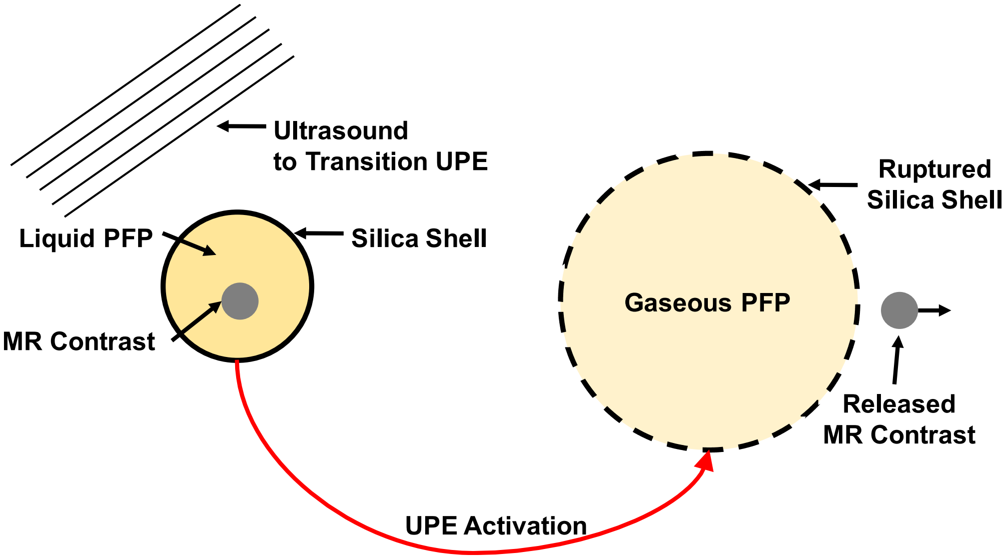

Figure 1.2. Diagram of formulation and activation of sUPE. Ultrasound exposure transitions the internal perfluorocarbon to a gas, causing expansion and rupturing of the silica shell. If the sUPE carries a payload (in this case, an MR contrast agent Gd_2O_3), it is then released to interact with the surrounding medium.[82]

1.5 Improving image guidance and evaluation of TULSA

TULSA ablation relies on a gold standard of MR thermometry and contrast-enhanced imaging for guidance and assessment. However, proton resonance frequency-based MR thermometry is not reliable in fatty tissues surrounding the prostate, preventing assessment of off-target ablation, and is also sensitive to motion, perfusion, and susceptibility changes.[34, 83] MR thermometry has been shown in previous studies[68] and in our own preliminary data to overestimate the area of TULSA-induced ablation by as much as a factor of two. Contrast-enhanced MR imaging often contains an enhancing rim around TULSA-induced lesions that complicates interpretation of the treated area,[84, 85] and tends to more accurately reflect the extent of ablation at later time points (3-14 days post-treatment), making the decision to apply immediate secondary treatments difficult.[86–89] sUPEs may offer a unique solution to inaccurate imaging-based estimates of TULSA ablation. Such particles can act as multi-modality contrast agents for MR and ultrasound imaging,[77, 79, 90] helping to localize non-palpable tumors.[90–92] Certain formulations can also alter contrast in MR images (if encapsulating paramagnetic substances) or ultrasound images (if transitioned into bubbles) upon fractionation, enabling imaging-based assessments of drug release or cavitation activity.[93, 94] Thus**,** sUPEs loaded with Gd_2O_3 nanoparticles could provide a high-contrast delineation of the treated zone or area of drug delivery immediately following TULSA insonation without the need for an additional intravenous MR contrast injection. sUPEs may therefore offer additional benefits for image-guidance of TULSA-mediated drug delivery and ablation.

1.6 Histotripsy as a standalone vs. combinatorial therapy for prostate cancer

Histotripsy has been developed pre-clinically as a standalone therapy to treat prostate pathologies,[95–100] including the ablation of ACE-1 PCa tumors, a metastatic cell line derived from the Labrador Retriever, implanted in a canine prostate model.[101] These studies indicate that histotripsy offers improved efficacy and reduced comorbidity over surgery, hormone therapy, and focal thermal techniques for treatment of localized recurrent prostate cancer.[36, 102, 103] Unlike thermal forms of therapeutic ultrasound or cryotherapy, the efficacy of histotripsy is not limited in large or well-vascularized tumors.[38, 39] Pre-clinical data indicate differential sensitivity of prostatic structures to histotripsy, with the urethra, nerves, and blood vessels being more resistant than the parenchyma.[96, 98] The resistance of these structures to mechanical ablation will alleviate comorbidities associated with thermal high-intensity focused ultrasound (HIFU) and cryoablation of prostate tissue.[17, 65] Histotripsy thus offers several unique advantages over other focal prostate cancer therapies, but its use as a standalone therapy neglects the known effects of ultrasound as a sonodynamic adjuvant. The mechanical action that accompanies ultrasound-mediated bubble activity increases the penetration of exogenous agents such as sonosensitizers into tumor tissue.[72, 104, 105] Fluid streaming induced by histotripsy bubble cloud oscillations[106] could also homogenize oxygen content and increase sensitizer distribution throughout the target tissue.[107–109] Thus, combining histotripsy with sonodynamic agents could greatly improve treatment outcomes in salvage treatments of localized, recurrent prostate cancer. Using ultrasound-guided histotripsy to mechanically ablate tumor tissue in combination with sonosensitizing agents to improve treatment homogeneity and control of tumor margins could provide a cost-efficient, highly efficacious treatment strategy in conditions where access to MR guidance equipment is limited.

1.7 Improving image guidance and evaluation of histotripsy

Histotripsy-induced bubble clouds appear hyperechoic on B-mode ultrasound (US) imaging. Liquefied tissue appears hypoechoic following treatment.[48, 49] Passive cavitation imaging (PCI)[50, 110, 111] is a diagnostic ultrasound technique under development that spatially maps the power of acoustic emissions from bubble cloud oscillations, a surrogate for the mechanical action of histotripsy. We have shown the spatial extent of histotripsy liquefaction to correlate better with acoustic emissions mapped via PCI than hyperechogenicity on plane wave B-mode ultrasound imaging in a prostate-mimicking tissue phantom.[51] In addition, PCI quantifies the strength of acoustic emissions generated by cavitation bubble clouds, which have been shown to correlate with the degree of ROS generation in SDT applications.[57, 112] Magnetic resonance (MR) imaging is an attractive supplement to diagnostic ultrasound in histotripsy guidance due to its excellent soft-tissue contrast, isotropic resolution, and high sensitivity to histotripsy-induced changes in tissue structure.[52–56] The prospect of reliable, multi-modality, real-time image guidance gives histotripsy a distinct advantage over other focal therapies. The improvement of PCI and MR imaging methods for histotripsy guidance would substantially facilitate clinical translation.

1.8 Innovation and clinical significance

1.8.1 Theranostic silica microshell-enhanced TULSA

This research plan combines recent advances in multiple fields to develop and evaluate novel approaches for treatment of recurrent prostate cancer. Chemotherapy can improve both palliation and overall survival in the treatment of metastatic recurrent prostate cancer,[44] but has also been hypothesized to offer survival benefit in cases of localized, radio-recurrent prostate cancer.[72, 113] Encapsulation of chemotherapeutics reduces dose-limiting systemic toxicities, significantly improving therapeutic indices.[22–24, 114] The first aim of the proposed research involves novel sUPEs containing gadolinium MR contrast to serve as a model drug and an indicator of cavitation activity during TULSA ablation (**Fig. 1**). UPEs have been transitioned primarily with focused, high amplitude ultrasound sources,[78–80, 115] although imaging pulses with intravascular ultrasound sources have also been used.[116] TULSA induces tissue ablation at a moderate acoustic output (up to 4 W acoustic power, typically between 1.1 and 1.8 W acoustic power)[35, 68] and has yet to be utilized to transition sUPEs. Although the use of MRI to delineate the TULSA-induced ablation zone has been established,[34, 35, 66, 68, 117, 118] the accuracy of MRI in the presence of exogenous UPEs has yet to be explored. The proposed studies will evaluate the MR contrast properties of these novel sUPEs and test their response to TULSA insonation in terms of payload release and enhancement of thermal ablation.

1.8.2 Histotripsy for Prostate Cancer Ablation with Quantitative Image Guidance

Histotripsy ablation has been applied in the treatment of several disease pathologies.[44] The ability of histotripsy to treat radio-recurrent disease has yet to be explored. Radio-recurrent prostate cancer exhibits resistance to many conventional approaches, whereas histotripsy has demonstrated safe, effective prostate cancer ablation in addition to significant improvement in chemotherapeutic efficacy. Thermal applications of HIFU utilize a gold standard of proton resonance frequency-based MR thermometry[34] for real-time assessment of treatment efficacy. There are no dose-defined metrics to quantify tissue liquefaction via the mechanical action of histotripsy. Passive cavitation imaging presents one potential method of defining a "mechanical dose" metric to enable real-time feedback of histotripsy. The use of such a metric would lead to safer, more precise delivery of histotripsy therapy. While qualitative descriptions of MR contrast change following histotripsy ablation have been documented,[53–56] quantitative descriptions are still lacking. Furthermore, quantitative measurements of histotripsy-induced changes in MR parameters have not been performed *in vivo*. In this dissertation, we study the correlation of tissue liquefaction and cell death as assessed histologically with fully registered MR and diagnostic ultrasound data sets *in vitro* and *ex vivo*. Using a variety of spatial correlation metrics, we thoroughly characterize these relationships and the information provided by each imaging modality.

1.8.3 Histotripsy for Sonodynamic Therapy

Thus far, microbubble contrast agents are the primary nucleation agents for sonochemically induced ROS generation.[57] The micrometer size of conventional microbubbles prevents extravasation for penetration beyond the tumor vasculature and restricts permeation of tumor regions with low vascularity. Histotripsy has yet to be implemented as a SDT trigger, despite its ability to produce strong cavitational activity in both vascular and hypoxic tissues. Ablation and homogenization of the oxygen content of the tissue with bubble activity may improve the spatial uniformity of ROS generation in SDT. Sonosensitizing particles can be fabricated at a size amenable to extravasation and diffusion beyond the tumor vasculature. Hydrophobic areas on the nanoparticulate surfaces may also serve as bubble nucleation sites, reducing the necessary tensile pressure required to initiate inertial cavitation. In previous *in vitro* and pre-clinical studies of SDT, a quantitative assessment of the inertial cavitation activity has been lacking.[57] Passive cavitation imaging (PCI) can quantitatively map the strength (i.e. acoustic power) and type (i.e. stable or inertial) of emissions from bubble activity in real time.[50] Previous studies have shown correlation between quantitative measures of cavitation (although not spatially mapped) and delivery of encapsulated chemotherapeutics.[112] PCI may therefore be an ideal modality for monitoring and quantitative dosing of SDT, as well as dose-mapping in drug delivery applications.

1.9 Dissertation Outline

This dissertation explores combinatorial approaches for the treatment of radio-recurrent prostate cancer involving three modalities: thermal ultrasound ablation, histotripsy, and sonodynamic therapy (Figure 1.3). Chapter 2 describes a combination of thermal ultrasound ablation and novel drug delivery vesicles (sUPEs) containing MR contrast as a model drug. Chapter 3 explores improved image guidance and evaluation methods for mechanical histotripsy ablation. Chapter 4 explores a combinatorial ultrasound therapy involving histotripsy ablation and sonodynamic therapy, as well as diagnostic ultrasound methods for quantitation of this treatment. In summary, we have performed a pre-clinical study of several combinatorial therapies that have yet to be explored or applied to treatment of prostate cancer. We have further explored several novel methods of image guidance and assessment for these therapies that have not been thoroughly investigated or developed. We believe that this work will help advance the clinical translation of therapeutic ultrasound ablation and sonodynamic therapy for the treatment of prostate cancer.

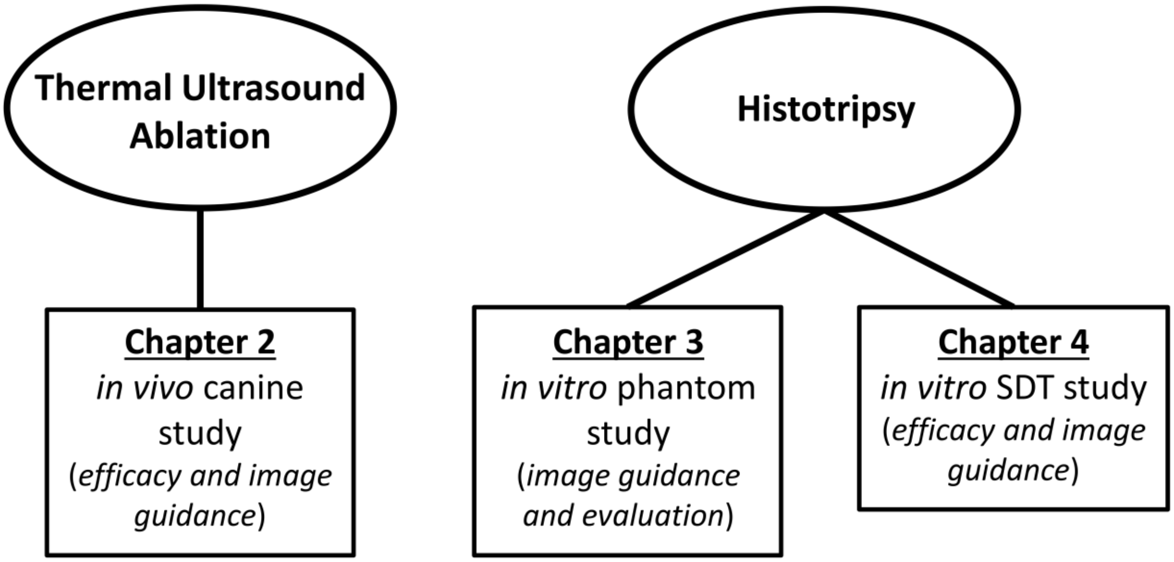

Figure 1.3. Diagram summarizing the work presented in this dissertation.

CHAPTER 2

ENHANCEMENT OF MRI-GUIDED TRANSURETHRAL ULTRASOUND ABLATION OF THE PROSTATE WITH SILICA-SHELL PHASE-SHIFT EMULSIONS

The work presented in this chapter has been published as: G.J. Anthony, K.B. Bader, J. Wang, *et al.*, MRI-guided transurethral insonation of silica-shell phase-shift emulsions in the prostate with an advanced navigation platform, Med Phys **46**(2), 774–788 (2019).

2.1 Introduction

Prostate cancer (PCa) is the second most common cause of cancer-related death in men, with an estimated 175,000 new cases and 32,000 deaths in the United States in 2019.[119] Prostate-specific antigen (PSA) screening indicates a large number of these cases are low- or intermediate-risk diagnoses.[120] Conservative approaches including active surveillance and watchful waiting can preserve quality of life, but with an increased risk of cancer progression and mortality.[121] Higher rates of cancer control can be achieved with whole gland surgical resection[2] or radiotherapy,[3] but these approaches are associated with a high incidence of treatment comorbidities such as incontinence, impotence, and bowel dysfunction.[11, 122] The development of local treatments for PCa is therefore an attractive compromise between conservative and radical treatments.

Magnetic resonance (MR)-guided therapeutic ultrasound is a localized, minimally or non-invasive ablative therapy.[64, 65] Transurethral ultrasound ablation (TULSA) administers acoustic energy directly into the prostate without having to traverse intervening tissue. MR imaging (MRI) enables real-time temperature monitoring to assess the treatment progress.[35, 36, 66] TULSA sources utilize an unfocused transducer, which enables bulk heating of prostate tissue. Pre-clinical studies have shown TULSA to be an effective and safe means of prostate ablation in healthy tissue with minimal side effects.[35, 68, 69] The chosen safety margin of 3 mm inside the prostate capsule minimizes side effects,[36] but spares an average of 10% of the prostate volume in the periphery, where many cancerous tissues are located.[36] Ablation of PCa in a Phase I trial has noted clinically significant residual cancer in 31% of patients,[123] indicating that refinement of TULSA techniques are necessary. In addition, the immediate physiological response of tissue to therapeutic insonation masks the full extent of tissue ablation,[84, 86, 87, 124, 125] necessitating novel imaging techniques to assess the treatment zone.

Silica-shell ultrasound-triggered phase-shift emulsions (sUPEs) can be transitioned to microbubbles to enhance the effects of therapeutic ultrasound[77–80] and act as multi-modality contrast agents.[77, 79, 90] sUPEs also exhibit increased stability and longevity *in vivo* compared with microbubbles or other nanoparticle formulations.[77, 78, 90, 92, 126] Transition of sUPEs containing MR contrast agents may increase MR image intensity for clearer delineation of the ablation zone.[93] Furthermore, bubble-enhanced heating has been demonstrated via droplet transition.[127, 128] Droplet accumulation in cancerous tissue would preferentially enhance heating of the target, allowing extension of TULSA treatment margins to peripheral zones with potentially reduced risk of damage to extracapsular structures.

To date, focused sources have been utilized to instigate droplet transition. The goal of this preclinical study was to assess sUPEs as therapeutic sensitizing agents and as ultrasound-activated MR contrast agents for monitoring TULSA prostate ablation. A secondary goal of this study is to evaluate dynamic contrast enhanced (DCE) MRI and MR thermometry as metrics of prostate ablation in the presence of sUPEs. sUPEs were filled with perfluorocarbon and an MR contrast agent, gadolinium-oxide (Gd_2O_3), to assess sUPE transition. To aid the cavitation process necessary for sUPE transition, an additional treatment arm combined sUPEs and a lipid-shell microbubble. Differences in therapeutic effects for each treatment arm were assessed with histology and MR imaging. Ablated areas were assessed using multiple imaging-based metrics and compared to measured lesion sizes from histological slides. In addition to 3 Tesla (3T) *in vivo* MR imaging before, during, and after the application of therapeutic ultrasound, *ex vivo* scanning of the prostate was performed at 9.4T to further assess the ablation zone.[129]

2.2 Materials and methods

2.2.1 Ultrasound phase-shift emulsion formulation

Tetramethyl orthosilicate (TMOS), trimethylphenylsilane (TMPheS), N-[3-(trimethoxysilyl)propyl]ethylenediamine (DETA), diethylene glycol, n-hexane, sodium hydroxide, methanol, sodium bicarbonate and Gadolinium (III) chloride hexahydrate were purchased from Sigma-Aldrich (St. Louis, MO). Oleic acid was procured from Tokyo Chemical Industry (Tokyo, Japan). Spherical polystyrene templates of 2-µm diameter were obtained from Polysciences (Warrington, PA). Perfluoropentane (PFP) was purchased from Strem Chemicals (Newburyport, MA). Milli-Q purified water was obtained from a Millipore SuperQ Plus Water Purification System (Billerica, MA). The 2-µm microshells used in this study were synthesized with methods previously developed by Liberman *et al*.[126] To visualize transition of the particles, an MR contrast agent, Gd_2O_3, was incorporated into the PFP liquid. Gadolinium oxide nanoparticles (2-nm diameter) were manufactured following a modified polyol method.[130] Briefly, gadolinium chloride hexahydrate was dissolved in diethylene glycol at 90–100°C for four hours. Sodium hydroxide was added to the solution to form precipitates. The solution was heated to 140°C for one hour, subsequently heated to 180°C for four hours, and finally cooled to 140°C. Oleic acid was added to the solution to displace the surface diethylene glycol for 24 hours. Methanol was added to precipitate the oleic acid coated gadolinium oxide, which was washed three times in methanol. The pellets were then suspended in hexane. Sodium bicarbonate was used to remove excess oleic acid. The remaining purified oleic acid coated gadolinium oxide nanoparticles were stored in hexane solution.

To incorporate gadolinium oxide nanoparticles, the polystyrene templates were initially swollen in 10% hexane in ethanol for one hour. Gadolinium oxide nanoparticles were also suspended in the hexane solution. After one hour of incubation, the polystyrene templates were centrifuged and the solution was replaced with ethanol for polymer contraction of at least 24 hours. After contraction, the templates returned to their original size and could be used for silica synthesis. To incorporate the PFP, the shells were first subjected to a vacuum-refill cycle to clean the surface. PFP gas was then injected into a vacuumed vial containing the shells and placed on ice to condense the gas. Additional PFP gas was then introduced, followed by an injection of degassed water. The PFP remained trapped within the shells due to its hydrophobicity and Laplace pressure.

2.2.2 *In vitro magnetic resonance imaging*

In vitro measurements of the MR signals generated by the Gd_2O_3-sUPEs were performed on a 3T Ingenia dStream MRI system (Philips Healthcare, Best, The Netherlands) using the body transmit coil and a 16-channel head coil. The relaxivities of Gd_2O_3-doped sUPEs were measured by comparing signal intensities in T_1- and T_2-weighted images of sUPEs in fully intact and transitioned states. sUPEs with and without Gd_2O_3 doping, and with or without ultrasound-induced transition, were suspended in a 1% agarose mixture at Gd concentrations ranging from 0.05 to 1.0 mMol (~0.05 to 1.5 mg/mL of particles). Inversion-recovery spin echo (IR-SE) sequences (TI = 50, 100, 250, 500, 750, 1000, 2500, 5000 ms) and turbo-spin echo (TSE) sequences (TE = 6.4, 8, 10, 12, 15, 17.5, 20, 25, 30 ms) were acquired to quantitatively measure the relaxation times T_1 and T_2, respectively. For each pixel of the IR-SE images, the pixel magnitude, S, was fit using a least squares method to an exponential recovery equation:[131]

$$S = \left|M_0\left(1 - 2e^{-TI/T_1}\right)\right|, \tag{2.1}$$

where TI is the inversion time, S is the measured signal magnitude for inversion time (TI), M_0 is the fitted maximum signal magnitude as a function of TI, and T_1 is the fitted T_1 time. Similarly, for each pixel of the TSE images, the magnitude was fit using a least squares method to an exponential decay:[132]

$$S = M_0 e^{-TE/T_2}, \tag{2.2}$$

where TE is the echo time, S is the measured signal magnitude at echo time (TE), M_0 is the fitted maximum signal magnitude, and T_2 is the fitted T_2 time. A long TR (> 5000 ms) was used in both sequences to ensure sufficient magnetization recovery.[133] Uncertainty in the measured values for T_1 and T_2 was taken as the average 95% confidence interval of the fitted T_1 and T_2 values over each sUPE suspension. T_1 and T_2 relaxivities (r_1 and r_2) are reported as the linear slope of $1/T_1$ and $1/T_2$, respectively, as a function of Gd concentration.

2.2.3 Therapeutic ultrasound therapy system

A prototype transurethral ultrasound therapy system (Philips, Vantaa, Finland)[68] was used for transurethral insonation, as illustrated in Figure 2.1. The therapy system includes a rigid applicator [5 mm (15 French) diameter] with an unfocused array of eight laterally aimed transducer elements (4 mm x 5 mm area/element) with a 3.75-MHz center frequency. The acoustic field of the transurethral device was measured with a 400-μm needle hydrophone (HNP-0400, Onda Corporation, Sunnyvale, CA, USA) mounted on a computer-controlled, three-axis positioning system (MN-10, Velmex, Inc, Bloomfield, NY, USA).

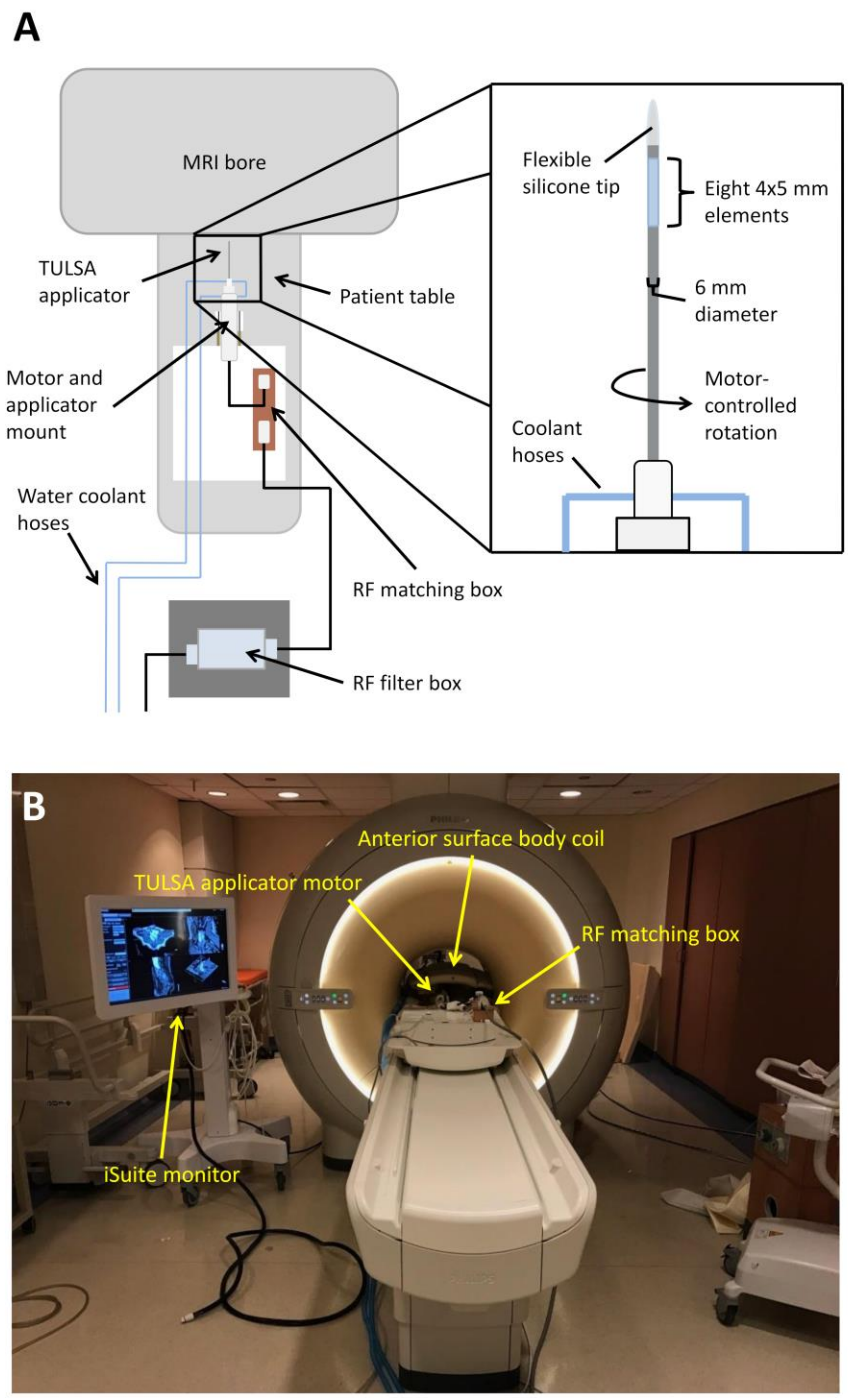

Figure 2.1. (A) Top down schematic of the ultrasound therapy system components inside the MRI scanner room, and dimensions of TULSA applicator. Device output and rotation was controlled from the scanner control area to apply static insonations to injection sites. The coolant hoses connect to a pump in the scanner control area. The RF filter box connects to the ultrasound generator and controller PC. (B) Photograph of scanner room just prior to TULSA procedure. An anterior body surface coil was used in conjunction with the posterior coil embedded in the scanner table.

Insonations of 3.7–4.2 W acoustic power per element were initiated with the transurethral device. The free field (underated) peak negative pressure of the acoustic field was approximately 2.5–2.8 MPa (spatial peak, temporal peak). To target desired locations within the prostate, a motorized mount was used to rotate the applicator around its central axis. During insonation, degassed, room temperature water (20°C) was circulated through a closed loop over the transducer elements to prevent thermal damage to the urethra and overheating of the transducer elements.

2.2.4 Pre-treatment procedure

This study included a total of six male mixed-breed healthy canines aged 3-4 years. The canines were housed in accordance with all federal policies and the Guide for the Care and Use of Laboratory Animals. All work was done under an IACUC-approved protocol and under the supervision of a veterinarian in an AAALAC-accredited facility. A perineal urethrostomy was performed on the canine subjects at least 12 months prior to the procedure to allow insertion of the ultrasound applicator into the prostatic urethra. Following the urethrostomy, animals were monitored to prevent infection or re-closing of the stoma during the healing process. Canines maintained normal activity and were monitored several times per day by the veterinary staff. No medical issues occurred during the post-surgical period. Prior to insertion of the transurethral device, animals were sedated intramuscularly with buprenorphine (10.9-15 µg/kg), ketamine (2.4-3.6 mg/kg) and dexdomitor (13.4-18 µg/kg). The animals were intubated and placed on isoflurane gas anesthesia with a ventilator over the course of the procedure. A Foley catheter was inserted in the stoma to void bladder fluid prior to insertion of the ultrasound applicator. A plastic tube was also inserted in the rectum to prevent flatulence during the procedure. Throughout the procedure, animals were given a physiological saline solution intravenously.

Heart rate, body temperature, blood pressure, respiratory rate, SPO_2, and end tidal CO_2 were monitored by a certified veterinary technician. Perineal incision had to be performed in two of the six animals to enlarge the urethrostomy for insertion of the ultrasound applicator. The applicator was lubricated with aqueous gel (Aquasonic 100, Parker Laboratories Inc., Fairfield, NJ, USA) to facilitate insertion into the urethrostomy and achieve acoustic coupling with the urethra wall.

2.2.5 Therapy planning and monitoring

All MRI scans of the canines during the TULSA procedure were performed on a commercial 3T Achieva dStream MRI system (Philips Healthcare, Best, The Netherlands) using the body transmit coil, a 16-channel anterior receive coil placed on the abdomen, and a 16-channel posterior receive coil embedded in the scanner table (Figure 2.1b). The ultrasound applicator was positioned using real-time feedback from a balanced turbo field echo (bTFE) sequence via a Philips interventional imaging system prototype (Interventional MRI Suite (iSuite), Philips Research Labs, Hamburg, Germany) (Figure 2.2). Three orthogonal imaging planes were acquired and updated in real time to guide the applicator through the urethra and position the elements at the level of the prostate. Baseline T_1-weighted spin echo (T_1W SE), T_2-weighted spin echo (T_2W SE) and diffusion-weighted images (DWI) were acquired prior to the treatment protocol. The number of image slices varied from 12-20 for all pre- and post-insonation imaging sequences, depending on prostate size. Table 2.1 summarizes the scan parameters for each sequence performed for therapy planning, monitoring, and evaluation.

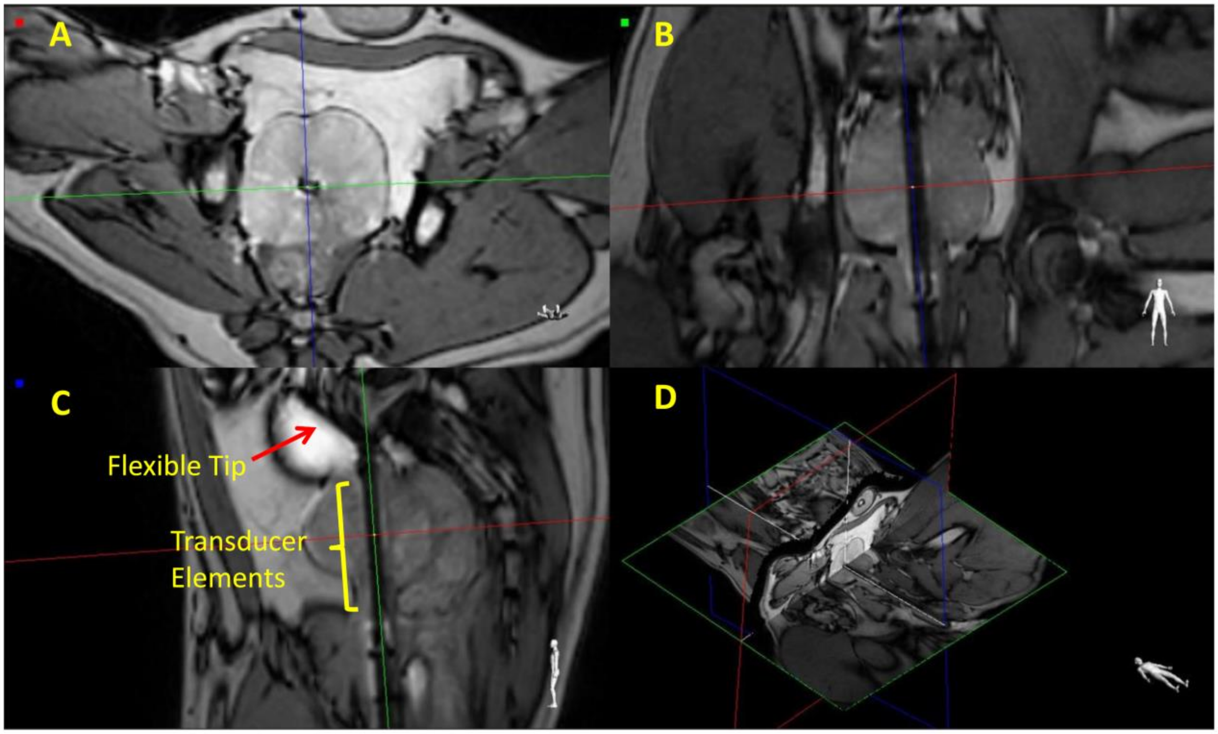

Figure 2.2. Orthogonal *in vivo* 3T MR images [(A) axial, (B) coronal and (C) sagittal] showing placement of ultrasound applicator using iSuite interface. MR scan parameters for this 2D bTFE sequence are given in Table 2.1. iSuite guidance was used to ensure positioning of the applicator at the proper depth in the prostatic urethra. The colored lines in each image indicate the cross-sections of the orthogonal image planes. Orientation is denoted by the colored square in the upper-left corner of each frame (red=axial, green=coronal, blue=sagittal). The three image planes are centered on the ultrasound applicator, as indicated in (D) the 3D reconstruction of the dataset.

Table 2.1: MR imaging sequence scan parameters for treatment planning, monitoring, and evaluation acquired on a 3T MRI scanner.

Sequence	TR/TE (ms)	In-plane resolution (mm^2)	Array size	Slice thickness (mm)	Slice gap (mm)	NSA	TSE/TFE/EPI factor	Temporal resolution (s)	b-values (s/mm^2)
T_2W TSE	4,500/115	0.75 x 0.75	528 x 528	3	0	2	16	N/A	N/A
T_1W TSE	559/16	0.7 x 0.7	512 x 512	3	0	1	5	N/A	N/A
2D bTFE	3.5/1.21	1.33 x 1.32	288 x 288	5	N/A	1	428	1.5	N/A
Temperature Mapping 2D FFE	14/8.0	2.0 x 2.0	176 x 176	4	N/A	1	1	1.3	N/A
DWI EPI	3884/65	1.25 x 1.25	288 x 288	3	0	6	59	N/A	50, 100, 500, 1000
DCE 3D FFE	5.2/1.52	1.16 x 1.16	128 x 128	5	-2.5	1	N/A	7.3	N/A

TSE/TFE = turbo spin echo/turbo field echo; bTFE = balanced turbo field echo; FFE = fast field (gradient) echo; DWI = diffusion-weighted imaging; EPI = echo planar imaging; DCE = dynamic contrast enhanced; TR = repetition time; TE = echo time; NSA = number of signal averages.

For each canine, an MR-compatible biopsy needle was used to guide the insertion of a semi-rigid plastic sheath to a target location within the prostate under guidance with the iSuite system. Through the sheath, a 1 mL solution of either physiological saline solution alone (sham), saline and sUPEs (1.2 to 2.0 mg/mL, 4% to 5.4% Gd by weight), or saline, sUPEs, and Optison^{TM} (10 μL/mL, consistent with the manufacturer's recommended dose, General Electric (GE) Healthcare, Marlborough, MA, USA) was injected directly into the prostate (Figure 2.3). Administered injections were separated by 10.0 to 25.9 mm to prevent overlapping insonation zones. The concentration of sUPEs was chosen to approximate physiologic concentrations of clinical MR contrast in the prostate.[134] The order and location of each applied treatment arm were randomized for each subject. Following each injection, the same T_1W and T_2W sequences as used prior to injection were repeated to assess any change in contrast.

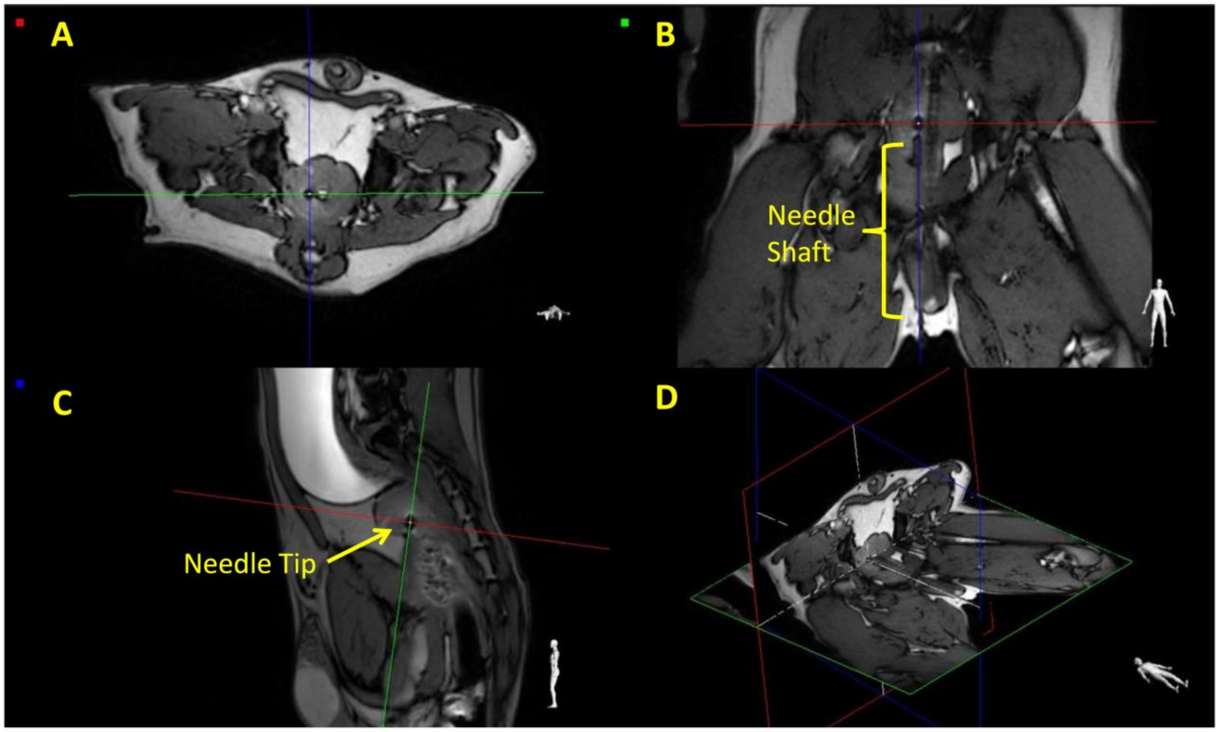

Figure 2.3. Orthogonal *in vivo* 3T MR images [(A) axial, (B) coronal and (C) sagittal] from iSuite interface showing insertion of biopsy needle for particle injection into the prostate. MR scan parameters for this 2D bTFE sequence are given in Table 2.1. iSuite was used to guide needle insertion and confirm accurate placement of the needle tip in the prostate. The three image planes are centered on the needle tip, indicated by the yellow arrow in (C). A 3D reconstruction of the dataset (D) is also rendered.

A test sonication (2.1 W acoustic power/element, 20 s duration) was applied to verify the correct angular position, required number of active elements for full coverage of the injection, and acoustic coupling quality. Once proper targeting was verified, thermometry images were monitored until the insonified zone returned to baseline temperature (37°C). An insonation with 3.7–4.2 W acoustic power/element was then applied. Multiple injections were performed in each animal. Thus, all insonations were applied statically (i.e. without rotating the TULSA device) in the direction of one injection. Tissue temperature was monitored using the proton resonance frequency (PRF) shift method (0.0094 ppm/°C).[34] Temperature maps were acquired at 0.5-3 Hz and overlaid on the anatomical MR images using the iSuite system. The first insonation in each subject was stopped once the temperature reached 56°C[68] at a control point placed 3 mm inside the edge of the prostate capsule, or once five minutes of insonation had elapsed. This cutoff temperature induces a lethal thermal dose of 240 CEM_{43} within the approximate two-second temporal resolution of the temperature mapping sequence.[135] The subsequent treatments were applied following each injection, using the same insonation time and parameters to maintain consistency in the injections' ultrasound exposure. Figure 2.4 illustrates the treatment planning and monitoring process, including marker placement, temperature mapping, and thermal dose map calculation.

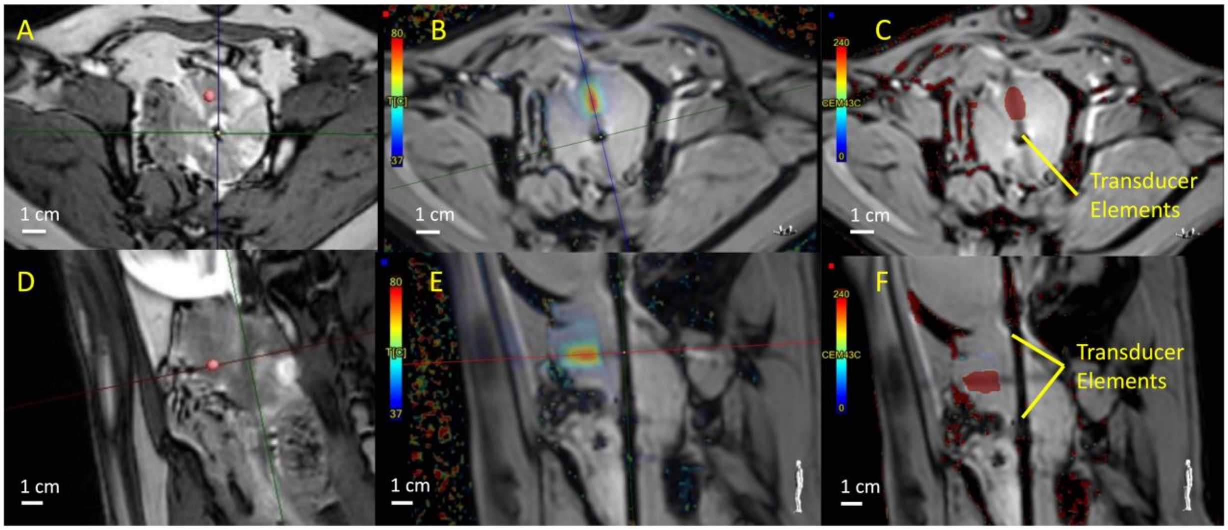

Figure 2.4. *In vivo* treatment planning, monitoring, and evaluation using the iSuite interface at 3T. MR scan parameters for (A, D) the 2D bTFE sequence and (B, C, E, F) the 2D FFE temperature mapping sequence are given in Table 2.1. (A, D) Placement of treatment marker (red sphere) at injection site using bTFE images, (B, E) real-time thermography images acquired during therapy (scale = 37–80°C), and (C, F) post-treatment thermal dose maps (scale = 0–240 CEM_{43}) for a lesion in (A, B, C) axial and (D, E, F) oblique-sagittal planes. The crosshairs in frames B and E are centered on the transducer, whose elements are aimed upward in frames B and C and to the left in frames E and F.

After each insonation, thermometry images were monitored until the insonated region returned to baseline temperature (37–39°C), and an additional five-minute period was allotted to ensure the tissue temperature had equilibrated. The T_1W and T_2W SE sequences were then repeated to assess contrast change. Following completion of all insonations and post-therapy

T_1W and T_2W images, a final DWI sequence was acquired. An FDA-approved chelated gadolinium MRI contrast agent (Multihance, Bracco Diagnostics, 0.1 mmol/kg) was then injected intravenously, and the uptake and washout within the prostate was monitored with DCE images acquired with a fast field echo (FFE) T_1W sequence over the course of 10 min. Contrast injection proceeded after at least 5 baseline T_1W acquisitions. Following the procedure, canines were euthanized by giving pentobarbital (100 mg/kg) intravenously. A prostatectomy was performed, and the prostate and surrounding tissues were examined for gross abnormalities. The excised prostates were placed into 10% buffered formalin (Fisher Scientific, Hampton, NH, USA) following removal of surrounding fatty tissues and seminal vesicles. Figure 2.5 gives the timeline of a typical experiment.

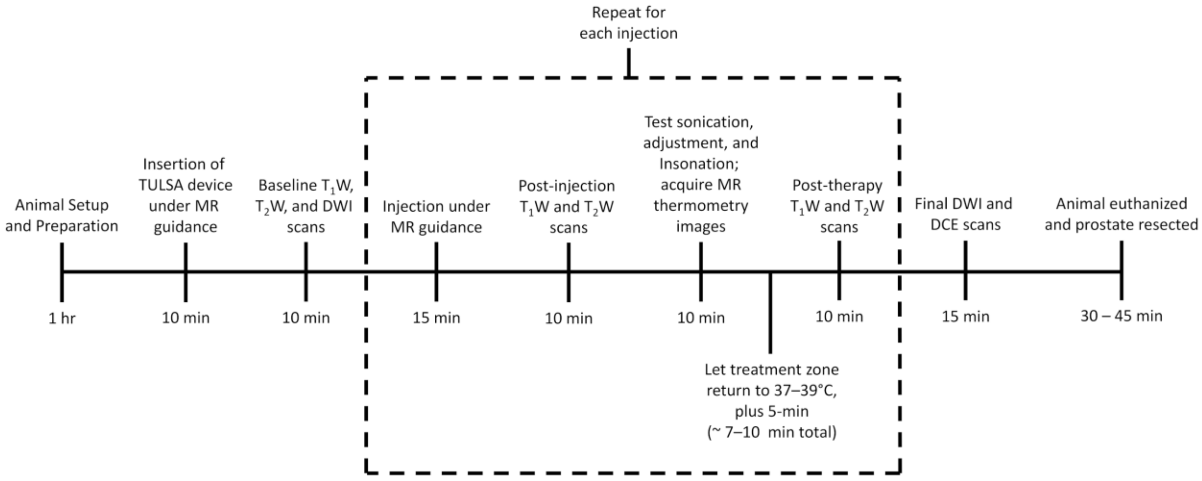

Figure 2.5. Timeline of typical canine experiment, including setup, injections, treatments, and image acquisitions. All post-treatment images were acquired 5 minutes after temperatures in the treatment zone had returned to 37–39°C. 3T MR scan parameters are given in Table 2.1.

2.2.6 3T image analysis and treatment evaluation

Pre- and post-therapy T_1W images were evaluated to determine the change in MR contrast after insonation of each treatment arm. Regions of interest (ROIs) encompassing the treated area (lesion ROIs) and ROIs in the prostate but completely outside the treated area (noise ROIs) were drawn in 8-10 slices for each canine prostate. Pre-and post-therapy images were registered using custom-scripted landmark-based affine registration, and subtraction images (post-therapy minus pre-therapy) were calculated. Contrast-to-noise ratios (CNRs) for each lesion were then computed from the subtraction images as

$$CNR = \sqrt{2}\,\frac{\mu_L}{\sigma_N}, \tag{2.3}$$

where μ_L is the mean pixel value in the lesion ROI, σ_N is the standard deviation in the noise ROI, and the factor of $\sqrt{2}$ accounts for Gaussian error propagation causing additive noise in the subtraction image.[136] Following treatment, diffusion-weighted images were analyzed to calculate apparent diffusion coefficient (ADC) maps by fitting signal intensities as a function of b-value to an exponential decay on a pixel-wise basis.[137]

Phase images acquired from the temperature mapping sequence were processed to compute temperature changes from an assumed baseline of 37°C. Phase drift was corrected to zero-order by computing the shift in the largest temperature histogram peak and subtracting this value from the entire map. The boundary of pixels reaching 55°C (55°C isotherm) was determined for each insonation.[66, 117] Thermal dose maps were calculated from temperature data via the Sapareto-Dewey equation.[135] The areas of pixels receiving thermal doses of at least 240 cumulative equivalent minutes at 43°C (CEM_{43}) were measured to estimate the extent of delayed cell kill.[35, 118, 138, 139] Before the thermometry sequence was optimized, some temperature maps generated by iSuite had erroneous discontinuities due to high phase image noise that prevented accurate phase unwrapping. Therefore, all thermometry data were subjected to a deterministic phase unwrapping algorithm[140] to recompute the temperature data offline prior to analysis. Temperature drift was corrected for these cases as described above. Temperature uncertainty was taken as the temporal standard deviation in an area of prostate completely outside the heated zone, after correcting for global phase drift over the duration of the procedure. This uncertainty was propagated through calculations of 55°C isotherms and 240 CEM_{43} dose boundaries to compute an estimate of the error in these metrics.

In order to analyze the time dependent thermometry data, temperature map pixels within the prostate that received 240 CEM_{43} or greater were fit (least-squares) to an exponential recovery of the form:

$$T(t) = T_{Eq}\left(1 - e^{-\alpha(t+t_0)}\right) , \tag{2.4}$$

where $T(t)$ is the temperature at time t, T_{Eq} is a fitting parameter that represents the equilibrium temperature approached in the tissue, α is a rate coefficient of heat increase, and t_0 is a fitting parameter that represents the onset time of tissue heating. For each lesion, the average coefficients α and T_{Eq} were obtained over the top 25% of fitted pixels in terms of R^2 values (approximately $R^2 \geq 0.9$). Contrast-enhanced images were analyzed to assess non-perfused areas (NPAs) within the prostate. Regions of interest encompassing the non-perfused tissue were manually drawn and compared with the areas of lesions measured from stained histological slides. The areas within the 55°C isotherm and the 240 CEM_{43} thermal dose boundary were calculated for each treatment and compared with histology.

2.2.7 *Ex vivo 9.4 T MRI*

In order to visualize the fine structure of the ultrasound lesions, *ex vivo* canine prostate samples were imaged with a 9.4 Tesla Bruker BioSpec 33-cm horizontal bore scanner with a Bruker 72-mm birdcage volume coil (Billerica, MA). Samples were submerged in Fluorinert (3M Co., St. Paul, MN) and oriented to approximately replicate the *in vivo* orientation for the supine canines. Imaging protocols were tested on a phantom prior to prostate imaging. Fast low-angle shot

(FLASH) tri-pilot images were acquired in three orthogonal planes to verify correct positioning of the sample and determine angulation of axial slices for subsequent scans. T_1W and T_2W images were acquired, and sequences for T_1, T_2, and ADC mapping were performed as outlined in Table 2.2. ADC maps were computed from diffusion-weighted images by fitting to an exponential decay as described above.[137] T_1 maps were computed from variable-TR rapid acquisition with refocused echoes (VTR RARE) images by fitting each voxel magnitude in a least squares sense to an exponential recovery.[141] Similarly, T_2 maps were computed from multi-slice mutli-echo (MSME) images by fitting each voxel magnitude in a least squares sense to an exponential decay.[142]

Table 2.2: MRI scan parameters for *ex vivo* imaging at 9.4T.

Sequence	TR/TE (ms)	In-plane resolution (μm^2)	Array size	Slice thickness (mm)	Slice gap (mm)	NSA	RARE factor	b-values (s/mm^2)
FLASH Tri-Pilot	100 /2.2	312.5 x 312.5	256 x 256	1	N/A	1	N/A	N/A
T_2W Turbo-RARE	5000/30	215 x 215	256 x 256	0.5	0	2	4	N/A
T_1W FLASH	420/3.0	215 x 215	256 x 256	1	0	4	N/A	N/A
T_2 Mapping MSME	10,000/10* (32 TEs)	430 x 430	128 x 128	2	0	1	N/A	N/A
T_1 Mapping VTR RARE	280*/5.95 (10 TRs)	430 x 430	128 x 128	2	0	1	2	N/A
DWI	4,000/40	430 x 430	128 x 128	2	0	1	N/A	0, 150, 500, 1000, 1500

FLASH = fast low-angle shot; RARE = rapid acquisition with refocused echoes; MSME = multi-slice multi-echo; VTR = variable TR; DWI = diffusion-weighted imaging; TR = repetition time; TE = echo time; NSA = number of signal averages. *Smallest TR/TE

2.2.8 Histopathological analysis

Prostate specimens were submitted for gross and histologic examination. All prostates were fixed in 10% buffered formalin (Fisher Scientific, Hampton, NH, USA) and sectioned axially at 4-mm thickness to match 9.4T MRI slices. Processed paraffin blocks were sliced at 4-µm thickness and stained with hematoxylin and eosin (H&E). Slides of the whole mount prostate sections were reviewed by a board-certified pathologist, who delineated the outer boundary of the thermal coagulation zone. Slides were then imaged with a high-resolution desktop scanner and lesion sizes were computed as the entire area within the thermal coagulation boundary. Errors in lesion size, T_1 CNR, and T_{Eq} are given in Table 2.3. Errors in lesion sizes determined via thermal dose, 55°C isotherms, DCE NPAs, and histology are given in Table 2.4.

Table 2.3: Errors in histological lesion size (standard deviation of triplicate measurements), T_1 CNR (standard deviation in CNR over slices with apparent T_1 enhancement), and fitted parameter T_{Eq} (standard deviation over all fitted pixels).

Treatment	**Canine**	**Histological lesion area (mm^2)**	**T_1-CNR**	**T_{Eq} (°C)**
Saline	**1**	5.6 ± 0.5	0.82 ± 0.22	56.6 ± 2.7
	2	48.4 ± 1.7	1.12 ± 0.38	59.4 ± 5.1
	4	20.2 ± 0.8	4.00 ± 0.53	57.0 ± 5.0
	5	34.5 ± 1.2	2.02 ± 0.34	60.1 ± 2.9
	6	31.7 ± 1.4	1.99 ± 0.29	54.2 ± 0.4
sUPEs Only	**1**	0.0[a]	0.33 ± 0.32	47.7 ± 3.4
	2	104.8 ± 3.5	2.86 ± 0.45	97.1 ± 15.3
	4	15.0 ± 2.6	0.57 ± 0.25	53.4 ± 2.4
	5	23.2 ± 2.5	0.00 ± 0.41[b]	58.4 ± 2.6
	6	89.7 ± 2.4	1.23 ± 0.11	59.7 ± 3.7
sUPEs + Optison	**2**	93.2 ± 3.0	0.36 ± 0.38	102.5 ± 17.1
	4	2.7 ± 0.2	3.55 ± 0.72	56.1 ± 2.1
	5	48.2 ± 1.0	1.23 ± 0.31	68.3 ± 4.1
	6	69.2 ± 2.3	2.32 ± 0.77	78.0 ± 7.2

Canine 3 is excluded, as it was only administered one injection with a notably higher Gd_2O_3 concentration than the other subjects.

[a] No lesion was apparent for this treatment.

[b] No positive post-treatment change in T_1 signal was observed for this lesion.

Table 2.4: Lesion areas as determined by thermal dose, 55°C isotherms, DCE NPAs, and histology.

Treatment	Canine	Histological lesion area (mm^2)	Non-perfused area (mm^2)	55°C isotherm area (mm^2)	240 CEM$_{43}$ area (mm^2)
Saline	**2**	48.4 ± 1.7	41.4 ± 4.0	85 [78–96]	127 [113–142]
	4	20.2 ± 0.8	28.5 ± 1.5	34 [22–43]	60 [48–71]
	5	34.5 ± 1.2	27.2 ± 2.8	103 [88–103]	164 [149–176]
	6	31.7 ± 1.4	21.4 ± 2.3	1 [0–8]	15 [12–18]
sUPEs Only	**2**	104.8 ± 3.5	103.8 ± 4.1	148 [134–164]	197 [177–221]
	4	15.0 ± 2.6	12.9 ± 3.4	22 [16–29]	49 [44–57]
	5	23.2 ± 2.5	35.7 ± 2.8	30 [29–31]	37 [28–40]
	6	89.7 ± 2.4	84.2 ± 3.5	100 [96–104]	105 [99–115]
sUPEs + Optison	**2**	93.2 ± 3.0	105.6 ± 11.9	166 [152–173]	189 [181–199]
	4	2.7 ± 0.2	2.7 ± 0.0	0 [0–0]	4 [3–6]
	5	48.2 ± 1.0	64.2 ± 3.5	88 [74–96]	105 [93–116]
	6	69.2 ± 2.3	111.0 ± 3.5	128 [115–133]	148 [139–159]

Errors in lesion size measurement and non-perfused areas were calculated as the standard deviation of triplicate measurements. Errors in 55°C isotherms and 240 CEM$_{43}$ dose boundaries were calculated by propagating the temperature uncertainty (approximately ± 1°C) through the computation of these areas. Only canines receiving all three treatments are included.

2.2.9 *Statistical analysis*

Maximum CNRs across axial sections, lesion areas determined from histology, and equilibrium temperatures (T_{Eq}) calculated as described above were compared between lesions generated at saline, sUPE, and sUPE with Optison injection sites using Wilcoxon signed-rank tests. Correlation between areas measured with histological visualization of the lesion, DCE NPAs, 55°C isotherms, and thermal dose maps was assessed using Pearson's correlation coefficient. Differences between areas measured using imaging metrics and the ground truth area measured via histology (i.e., bias in the imaging estimates) were assessed using Wilcoxon signed-rank tests. Correlation between related variables (such as α and T_{Eq}) was also assessed using Pearson's correlation coefficient, and variables found to be significantly correlated with another were excluded from Wilcoxon tests. Canine 3 was excluded from all analysis as a notably higher Gd_2O_3 concentration was employed than in other subjects. The overall significance level for statistical analysis was chosen as $\alpha = 0.05$. Bonferroni correction for multiple comparisons was applied to all pairwise tests among the three treatment arms and the repeated comparisons between histology and methods of ablation measurement (NPAs, 55°C isotherms, and thermal dose boundaries), resulting in a corrected significance level of $\alpha = 0.0167$ for these tests.

2.3 Results

2.3.1 In vitro magnetic resonance imaging

Figure 2.6 shows a T_1-map reconstructed using Equation (2.1) of the intact and transitioned UPE batches with internal Gd_2O_3 nanoparticles in 1% agarose, as well as a series of clinical gadolinium concentrations (gadodiamide, Omniscan, GE Healthcare) in 1% agarose, and a pure 1% agarose control. The T1-relaxivity for the non-transitioned UPEs was 0.09 L/mmol·s. T_1-relaxivity (r_1) of the transitioned UPEs was found to be of 9.9 L/mmol·s, which was higher than the measured r_1 of Omniscan in agarose (3.7 L/mmol·s). For the UPEs that were not transitioned, the r_2 was 17.4 L/mmol·s. T_2-relaxivity (r_2) of the transitioned UPEs was 119.0 L/mmol·s, and was considerably higher than the r_2 measured for Omniscan (18.1 L/mmol·s). The undoped silica shells filled with perfluorocarbon alone had T_1-relaxivities of 0.002 mL/mg·s and -0.08 mL/mg·s in transitioned and non-transitioned states, respectively, and T_2-relaxivities of 1.9 mL/mg·s and 0.55 mL/mg·s in transitioned and non-transitioned states, respectively.

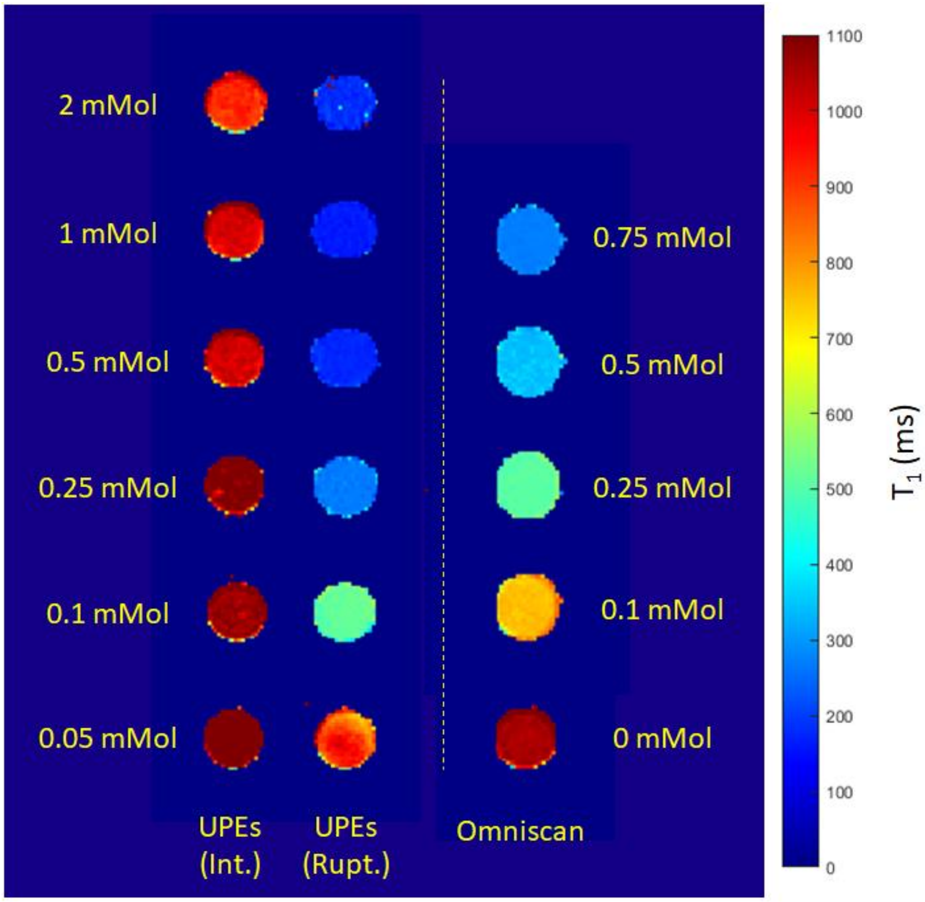

Figure 2.6. T_1-map of agarose suspensions of UPEs in intact and ruptured states, at the same overall Gd concentrations. A reference dilution series of the clinical Gd contrast agent (Omniscan) in agarose is included for reference. Intact UPEs show minimal T_1-relaxivity, while ruptured UPEs show even greater T_1-relaxivity than clinical MR contrast agent.

2.3.2 Insonation

A total of 15 insonations (one per administered injection listed in Table 2.5) were performed in six canines. Three to five active elements were utilized with 3.7 W to 4.2 W acoustic power per element (spatial peak, temporal peak negative pressures of 2.5–2.8 MPa). The pulse duration was between two and ten minutes depending on the prostate size and tissue heating rate. The time required to heat the control point to 56°C for the first excitation was set as the pulse duration for a given canine. Pulse durations were capped at five minutes to avoid wear on the applicator for subjects 2–6.

Table 2.5: Details of experimental and injection parameters for each procedure.

Canine	**sUPE % Gd by weight**	**sUPE injection concentration (mg/mL)**	**sUPE-only injection administered?**	**sUPE+Optison injection administered?**	**Sham (saline) injection administered?**
1	5.4%	1.2	Yes	No	Yes
2	5.4%	1.5	Yes	Yes	Yes
4	5.4%	1.2	Yes	Yes	Yes
5	5.0%	1.6	Yes	Yes	Yes
6	4.0%	2.0	Yes	Yes	Yes

All injections were 1 mL in volume. sUPE with Optison and sUPE-only injections had the same sUPE concentration when both were administered. Canine 1 was administered only saline and sUPE-only injections. Canine 3 was excluded from all analysis, as it was only administered one injection with a notably higher Gd_2O_3 concentration than the other subjects.

2.3.3 Histopathology

Ultrasound induced lesions were clearly demarcated in stained histological slides of the prostates (Figure 2.7). Treatments including sUPEs often exhibited a thermally coagulated rim of nearly complete epithelial sloughing and cell death surrounding a heat-fixed central area[118, 143, 144] that showed little to no epithelial sloughing, where all cells appeared nucleated. The frequency of thermal fixation among different treatment arms was compared using Fisher's exact test. Fisher's exact test was also used to assess the relationship between incidence of thermal fixation, hypointensity on *in vivo* T_2W imaging, and ring-shaped restricted diffusion on *ex vivo* diffusion-weighted imaging. Differences in T_1-contrast, the temperature parameter T_{Eq}, and the histological lesion size between non-heat-fixed and heat-fixed lesion groups were analyzed using Mann-Whitney U tests. Although thermal fixation was more common in the two experimental treatment arms, no significant difference in frequency of thermal fixation was observed between the three arms ($p > 0.0167$). Heat-fixed lesions had significantly larger histologic areas ($p = 0.002$) and greater temperature parameters T_{Eq} ($p = 0.004$) but did not differ significantly in T_1-contrast ($p > 0.05$).

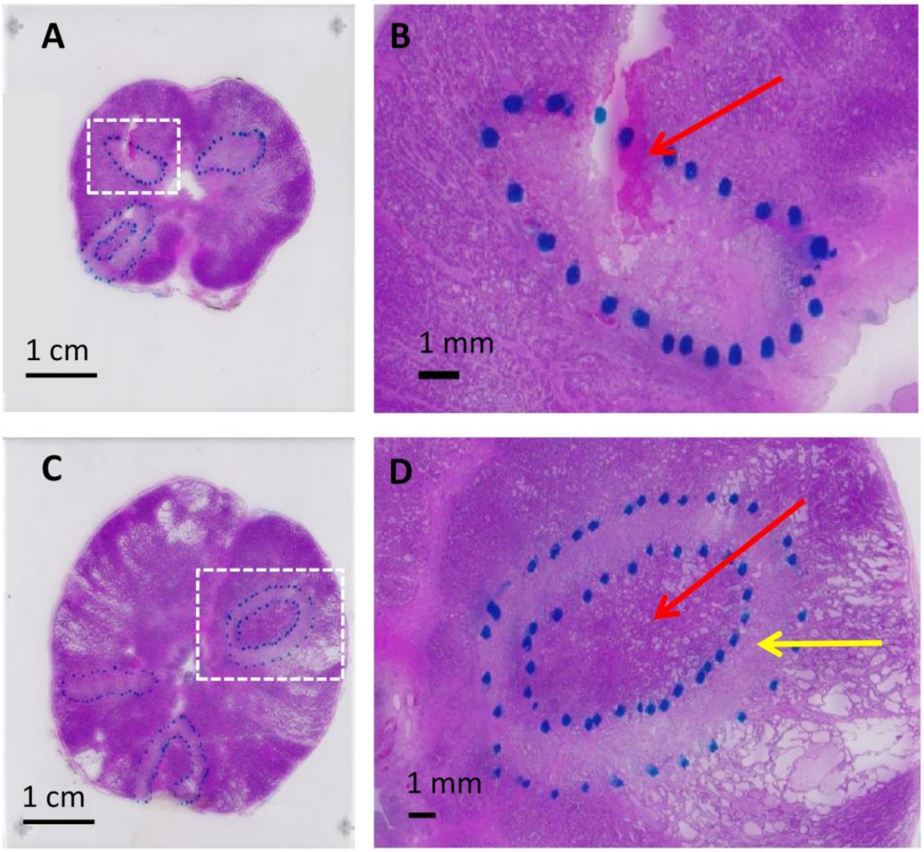

Figure 2.7. H&E stained histologic slides from central slices of (A) subject 5 and (C) subject 6. Coagulative necrosis zones (outlined with dashed blue marker) were apparent as pale regions (yellow arrow in D) that sometimes surrounded heat-fixed areas, where little to no epithelial sloughing or cell death was apparent (red arrow in D). Near-complete cell death and epithelial sloughing were visible in non-heat-fixed coagulative necrosis zones. A hemorrhagic area is visible as a magenta-stained region (yellow arrow in B).

2.3.4 3T MRI and iSuite

The alternating real-time acquisition of orthogonal image planes via the iSuite interface enabled accurate placement of both the US applicator and the needle tip in the prostate (Figures 2.2 and 2.3). Treatment monitoring via the iSuite interventional imaging system allowed real-time tracking of temperature and thermal dose. Interactive adjustment of image slice positions and orientations enabled easy alignment of image planes with the applicator and ultrasound beam path. Placement of reference markers at injection sites and control points allowed tracking of exact temperatures and thermal doses in real time, ensuring timely shutoff of the applicator. MR thermography images and dose maps showed that heated areas corresponded well to the positions of therapy markers placed prior to treatment (Figure 2.4). Temperature uncertainty was ± 1°C.

Injection boluses were not visible on T_2W-imaging in 12 of the 15 insonations (Figure 2.8e) or on T_1W-imaging post-injection for any insonation. The appearance of treatment zones on post-insonation MR images varied with treatment arm. Table 2.6 summarizes the qualitative observations from 3T imaging, 9.4T imaging, and histological assessment of treated tissue. Uniform hyperintensity or no change was observed in insonation zones in post-treatment T_1W images for all treatment arms (Figures 2.8a and 2.8b). Hyperintensity or no change was observed in T_2W images for saline sham treatments. T_2W image hypointensity at the centers of ablation zones only occurred in the experimental arms and was more frequent among lesions with heat-fixed tissue (Figures 2.8c and 2.8d). In the saline sham arm, ADC was either uniformly decreased within the treatment zone or unchanged after insonation. In some experimental treatments, small areas of unchanged diffusion (red arrow in Figure 2.9b) could be seen at the center of regions of restricted diffusion (yellow arrow in Figure 2.9b). This feature tended to correspond with heat-fixed lesions. Uniform areas of restricted diffusion exhibited ADC values of 1.0 ± 0.1 mm^2/ms, compared with 1.6 ± 0.2 mm^2/ms in uniform areas of untreated tissue. In all treatment arms, regions of non-perfusion were clearly delineated in DCE images through a distinct lack of contrast uptake (Figure 2.9a). Delayed enhancement was often seen in the periphery of NPAs as the DCE sequence progressed. Areas surrounding the non-perfused tissue showed increased contrast agent uptake compared with untreated prostate tissue, suggesting a hyperemic rim surrounding the acute area of thermal necrosis.[84] Good agreement was observed qualitatively between the positions of lesions in histological slides, NPAs on DCE imaging, areas of reduced diffusion on DWI, and thermal dose maps produced by iSuite (Figure 2.9). There was no qualitative difference in detectability of the treated region between treatment arms for any post-therapy 3T MR imaging modality.

Table 2.6: Key qualitative observations from histology, *in vivo* post-therapy imaging, and *ex vivo* imaging for each treatment.

		Histological observation		
		Untreated tissue	**Non-heat-fixed lesions**	**Heat-fixed lesions**
Appearance on H&E stain		Nucleated cells, intact epithelium	Contiguous region of near-complete epithelial sloughing and cell death	Heat-fixed area resembling untreated tissue, surrounded by boundary of near-complete epithelial sloughing and cell death
Appearance on 3T post-therapy imaging (compared with pre-therapy imaging)	**T_1W imaging**	No change	Hyperintense, or no change	Hyperintense
	T_2W imaging	Slightly hyperintense, or no change	Hyperintense, or no change	Hypointense (or hypo- and hyperintense), or no change
	ADC	No change	Decreased, or no change	Decreased; central area of unchanged ADC in some cases
Appearance on 9.4T Imaging, (compared with untreated tissue)	**T_1**	N/A	Decreased; spatially varying changes in some cases	Decreased; spatially varying changes in some cases
	T_2	N/A	Increased, or no change; spatially varying changes in some cases	Increased, or no change; spatially varying changes in some cases
	ADC	N/A	Decreased, or no change	Decreased, or no change; ring-shaped area of reduced ADC in most cases*

All 3T post-therapy imaging was acquired 5 minutes after MR thermometry indicated the treatment zone had returned to 37–39°C. MR scan parameters for 3T and 9.4T imaging are given in Tables 2.1 and 2.2, respectively.

* Feature is significantly more frequent in heat-fixed lesions.

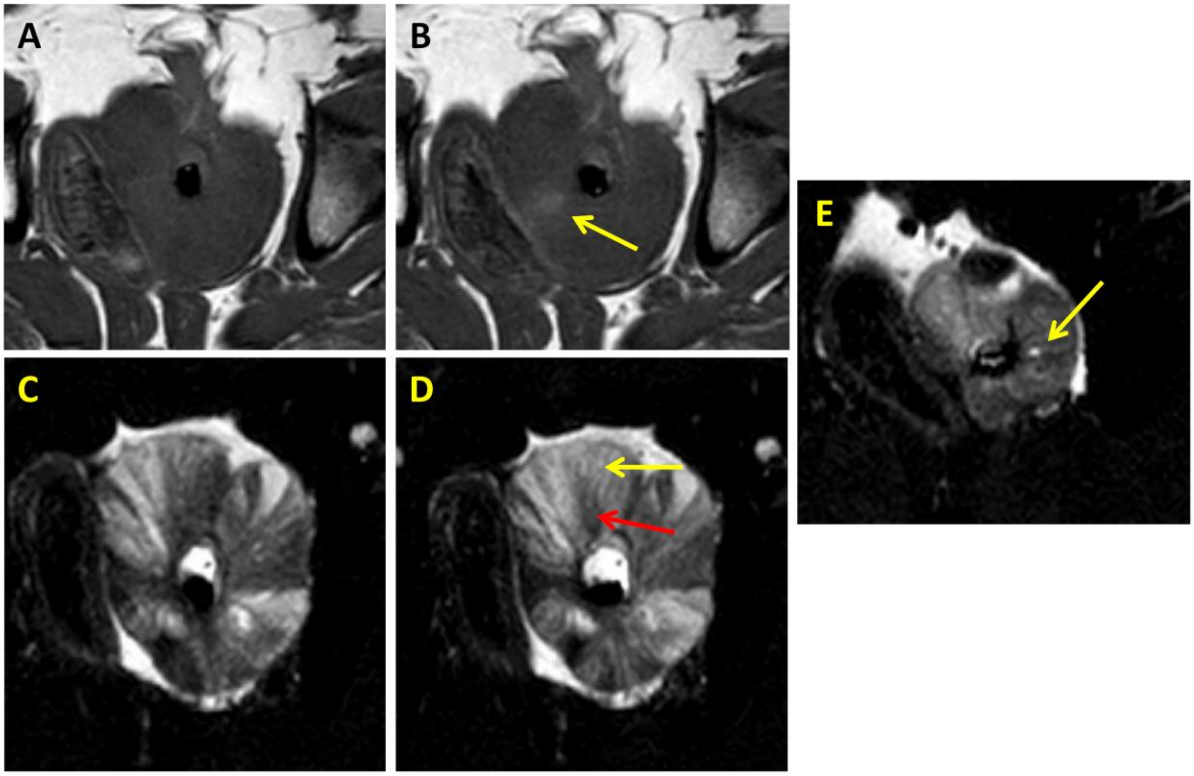

Figure 2.8. 3T *in vivo* T_1W and T_2W images of the prostate before and after therapy. MR scan parameters for (A, B) the T_1W TSE sequence and (C-F) the T_2W TSE sequence are given in Table 2.1. T_1W images acquired immediately (A) before and (B) after treatment and cooldown period, and T_2W images acquired immediately (C) before and (D) after treatment and cooldown period for a different insonation are shown. Some enhancement is visible in the treatment area in the post-therapy T_1W image, as indicated by the yellow arrow in (B). Signal enhancement is seen in the inflamed periphery of the treatment zone in the post-therapy T_2W image (D, yellow arrow), while the center of the lesion is relatively hypointense (D, red arrow). (E) Post-injection T_2W image showing the injection bolus of sUPEs with Optison as a small hyperintense region (yellow arrow). All post-therapy imaging was acquired 5 minutes after MR thermometry indicated the treatment zone had returned to 37-39°C.

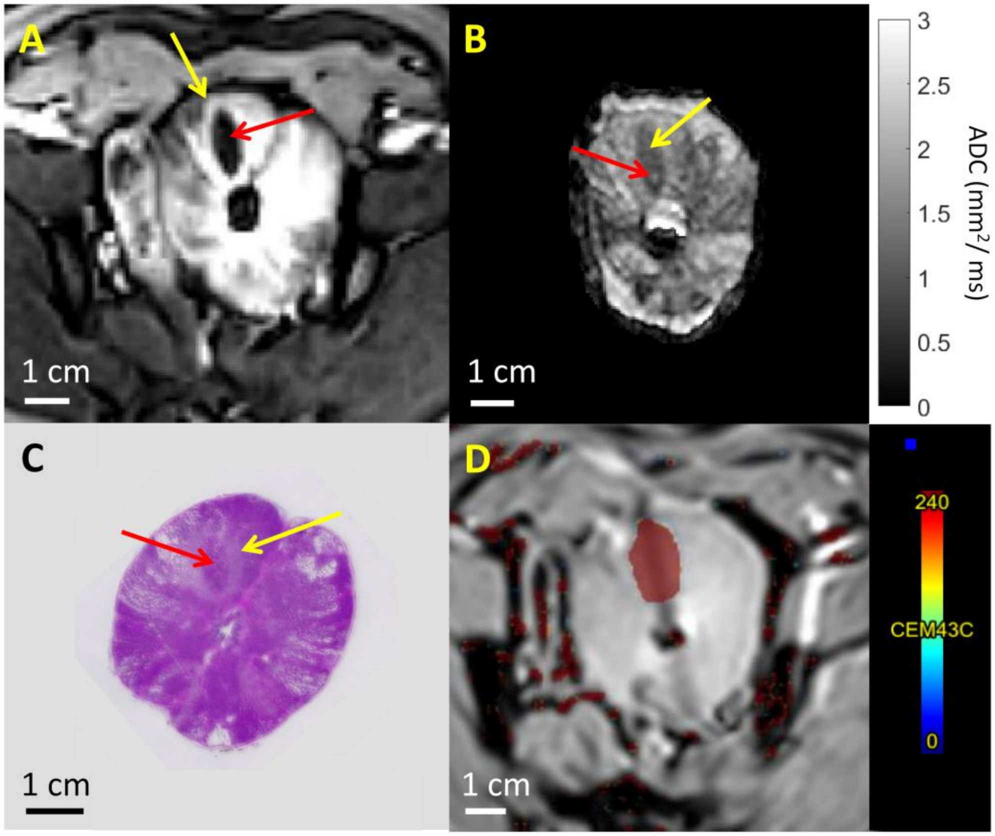

Figure 2.9. 3T *in vivo* post-treatment imaging and histology for evaluation of therapy. MR scan parameters for (A) the DCE 3D FFE sequence, (B) the DWI EPI sequence, and (D) the 2D FFE temperature mapping sequence are given in Table 2.1. (A) DCE image: Region of non-perfusion is noted via a red arrow. Enhancing rim surrounding the lesion is noted via a yellow arrow. (B) ADC map (scale 0 - 3 mm^2/ms): Restricted diffusion is marked by a yellow arrow. Small region of unaffected diffusion (possibly indicating thermal fixation) is marked by a red arrow. (C) H&E stained prostate section: Area of thermal fixation at center of lesion with normal stained appearance is indicated by a red arrow. The area of apparent coagulative necrosis (non-heat-fixed) is characterized by a pale color and exhibits epithelial cell sloughing and death, indicated by a yellow arrow. (D) Thermal dose map (scale 0 - 240 CEM$_{43}$): Dark red corresponds to a dose of 240 CEM$_{43}$ or greater. Treatment arm is sUPEs only. All post-therapy imaging was acquired 5 minutes after MR thermometry indicated the treatment zone had returned to 37-39°C.

2.3.5 Ex vivo 9.4 T MRI

High resolution 9.4T MR images of the *ex vivo* canine prostate tissue indicated increased T_2, decreased T_1, and reduced diffusion in the TULSA lesions compared with untreated tissue (Figure 2.10). Spatially varying changes indicating a subtle ring shape were observed in T_1 and

T_2 maps for 8 and 4 out of 14 cases, respectively. Spatially varying changes were more frequent in the experimental treatment arms and in heat-fixed lesions. For 6 out of 14 cases, the ADC at the lesion center was unchanged or increased compared with untreated tissue, while the ADC at the lesion periphery was reduced. (Figure 2.10c, red and yellow arrows). This feature was only observed for lesions generated with TULSA insonation of sUPEs or sUPEs with Optison, and was significantly more frequent among heat-fixed lesions ($p = 0.005$). In these cases, ADC values outside of treatment zones varied depending on tissue structure and fluid content, but ADCs in heat-fixed areas (0.73 ± 0.13 mm^2/ms) were relatively uniform and consistently larger than those in non-heat-fixed coagulation zones (0.40 ± 0.13 mm^2/ms). In canine 4, lesions exhibited small central regions of very high diffusion, high T_2 and low T_1, which histology confirmed to be hemorrhagic.

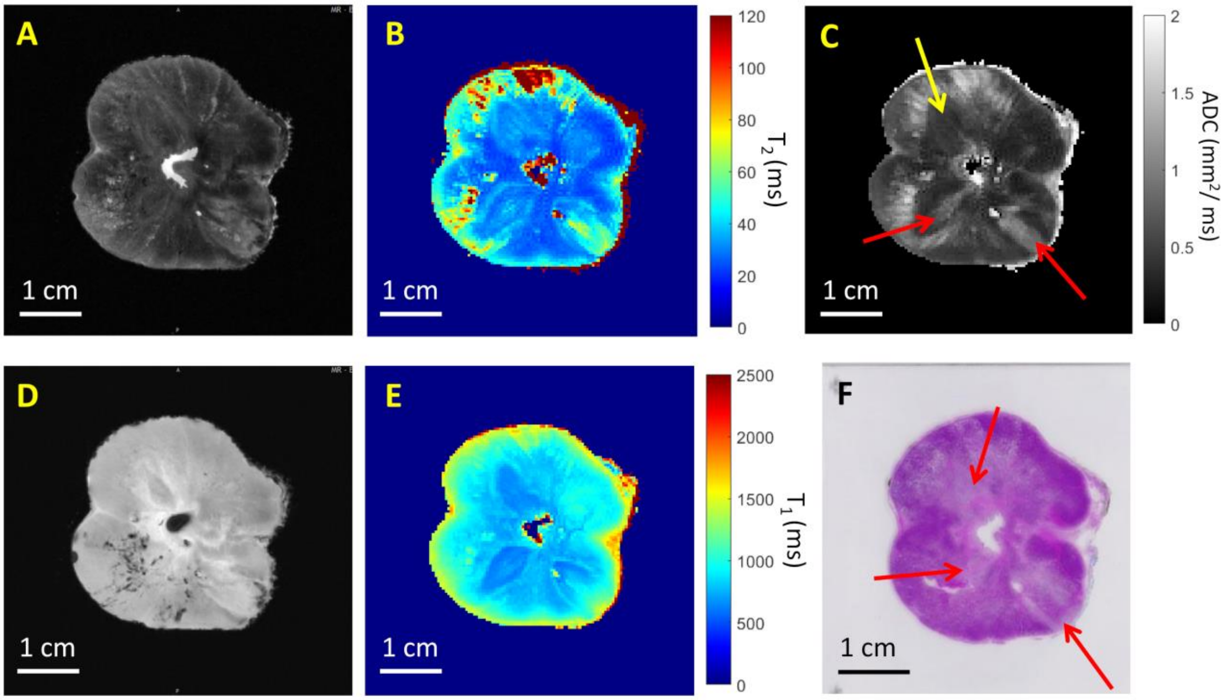

Figure 2.10. 9.4T *ex vivo* MRI images of canine prostate after *in vivo* treatment. MR scan parameters for (A) the T_2W TURBO-RARE sequence, (B) the T_2 mapping MSME sequence, (C) the DWI sequence, (D) the T_1W FLASH sequence, and (E) the T_1 mapping VTR RARE sequence are given in Table 2.2. (A) T_2W TURBO-RARE image, (B) T_2 map (scale 0 – 120 ms), (C) ADC-map (scale 0 - 2 mm^2/ms), (D) T_1W FLASH image, (E) T_1 map (scale 0 - 2,500 ms), and (F) H&E stained histological slide of the same axial prostate section. The three lesions are located roughly at the 5 o' clock (sUPE with Optison injection), 7 o' clock (sUPE injection), and 11 o' clock (saline sham injection) positions in the prostate, indicated by the red arrows in panel F. The red arrows in panel C indicate lesions with rims of reduced ADC surrounding central regions of unchanged ADC; the yellow arrow indicates a lesion with uniformly reduced ADC.

2.3.6 *Comparison of sUPEs, sUPEs with Optison, and saline sham*

Three metrics were compared amongst treatment arms: T_1 contrast-to-noise ratio, area of ablation, and equilibrium temperature (T_{Eq} in equation (2.4)). For each individual metric, no significant differences were observed amongst treatment arms (Figures 2.11 and 2.12). Treatment arms containing sUPEs had a wider range of lesion sizes and temperatures than the saline sham arm.

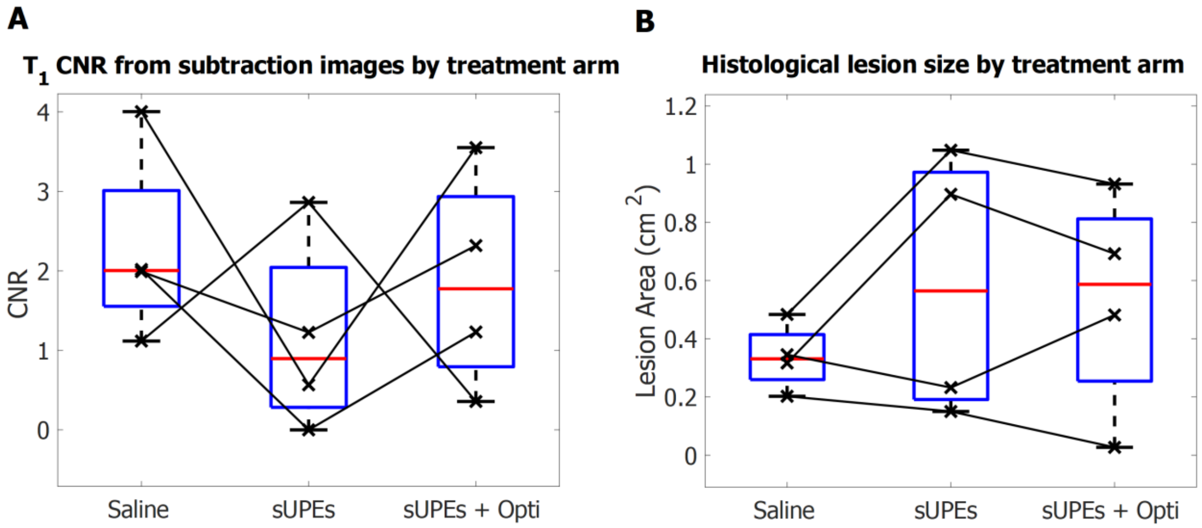

Figure 2.11. Comparison of treatments administered with saline, sUPEs only, and sUPEs with Optison. (A) Largest CNR in lesion ROI over all axial slices, as defined in equation (1). (B) Histological lesion size at most prominent axial slice. Red lines indicate medians, and blue boxes indicate interquartile ranges for each treatment group. Data points from the same canine are connected with black lines. No significant differences were observed between the three groups for CNR or lesion size. Only canines receiving all three treatments are included.

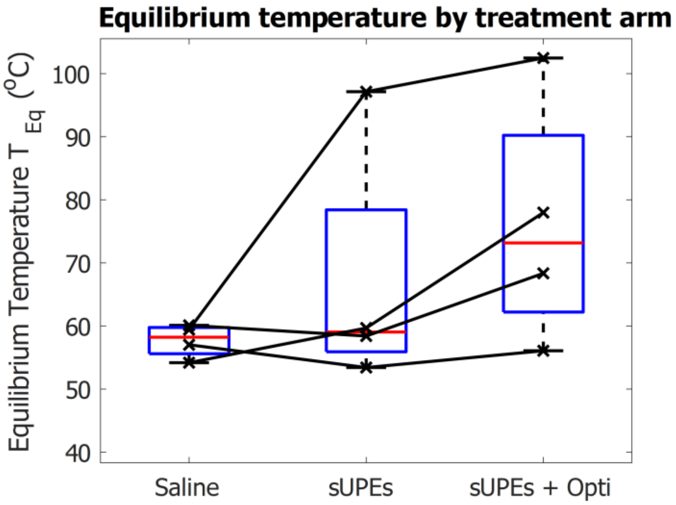

Figure 2.12. Comparison of $\boldsymbol{T_{Eq}}$ as defined in equation (3) for treatments administered with saline, sUPEs only, and sUPEs with Optison. Red lines indicate medians, and blue boxes indicate interquartile ranges for each treatment group. Data points from the same canine are connected with black lines. No significant differences were observed between the three groups. Only canines receiving all three treatments are included.

2.3.7 Comparison of lesion areas using histology, DCE MRI, and MR thermometry

Table 2.7 lists the measured areas of histological lesions, DCE NPAs, 55°C isotherms, and 240 CEM_{43} dose boundaries. Table 2.8 gives Pearson correlation coefficients (r) computed between histology and the three imaging-based methods of ablation zone measurement. The computed correlation coefficients between the histological lesion area and MR imaging metrics (DCE NPAs, 55°C isotherms, and CEM_{43} dose boundaries) ranged from 0.91–0.99 for arms containing sUPEs (N = 4 per arm). For sham arms lacking sUPEs, these correlations ranged from 0.50–0.69 (N = 4). For any given treatment arm (N = 4), the lesion areas ascertained via H&E, NPAs, 55°C isotherms, and thermal dose were not significantly different.

Table 2.7: Lesion areas as determined by histology, DCE NPAs, 55°C isotherms, and thermal dose.

Treatment	**Canine**	**Histological lesion area (cm^2)**	**Non-perfused area (cm^2)**	**55°C isotherm area (cm^2)**	**240 CEM_{43} area (cm^2)**
Saline	**2**	0.48	0.41	0.85	1.27
	4	0.20	0.29	0.34	0.60
	5	0.35	0.27	1.03	1.64
	6	0.32	0.21	0.01	0.15
sUPEs Only	**2**	1.05	1.04	1.48	1.97
	4	0.15	0.13	0.22	0.49
	5	0.23	0.36	0.30	0.37
	6	0.90	0.84	1.00	1.05
sUPEs + Optison	**2**	0.93	1.06	1.66	1.89
	4	0.03	0.03	0.00	0.04
	5	0.48	0.64	0.88	1.05
	6	0.69	1.11	1.28	1.48

Only canines receiving all three treatments are included.

Table 2.8: Pearson correlation coefficients (r) from tests of correlation between lesion sizes from histology, DCE NPAs, 55°C isotherms, and thermal dose measurements.

	Saline (n = 4)	**sUPEs (n = 4)**	**sUPEs + Optison (n = 4)**	**All Arms (n = 12)**
Histology/DCE NPA				
r (Pearson)	0.69	0.99	0.96	0.93*
Histology/55°C Isotherm				
r (Pearson)	0.54	0.98	0.99	0.89*
Histology/Thermal Dose				
r (Pearson)	0.50	0.91	0.99	0.81*

Values are separated by treatment arm (injection). Only canines receiving all three treatments are included.

* Significant correlation between the areas computed using the two listed methods.

When combining all treatment arms (N = 12), significant correlations were observed between areas measured via histology and each of the three imaging metrics examined: DCE MRI, 55°C isotherms, and thermal dose ($p < 0.002$). Areas measured via histology and DCE MRI were not significantly different when combining all treatment arms ($p = 0.47$). Areas of 55°C isotherms were 1.4 ± 0.8 times larger than histological areas ($p = 0.009$). Areas measured via thermal dose were 2.2 ± 1.1 times larger than those measured via histology ($p = 0.003$). Figure 2.13 plots the areas measured with histology, DCE MRI, 55°C isotherms, and thermal dose for each treatment arm and gives linear fits and correlation coefficients between each pair of methods.

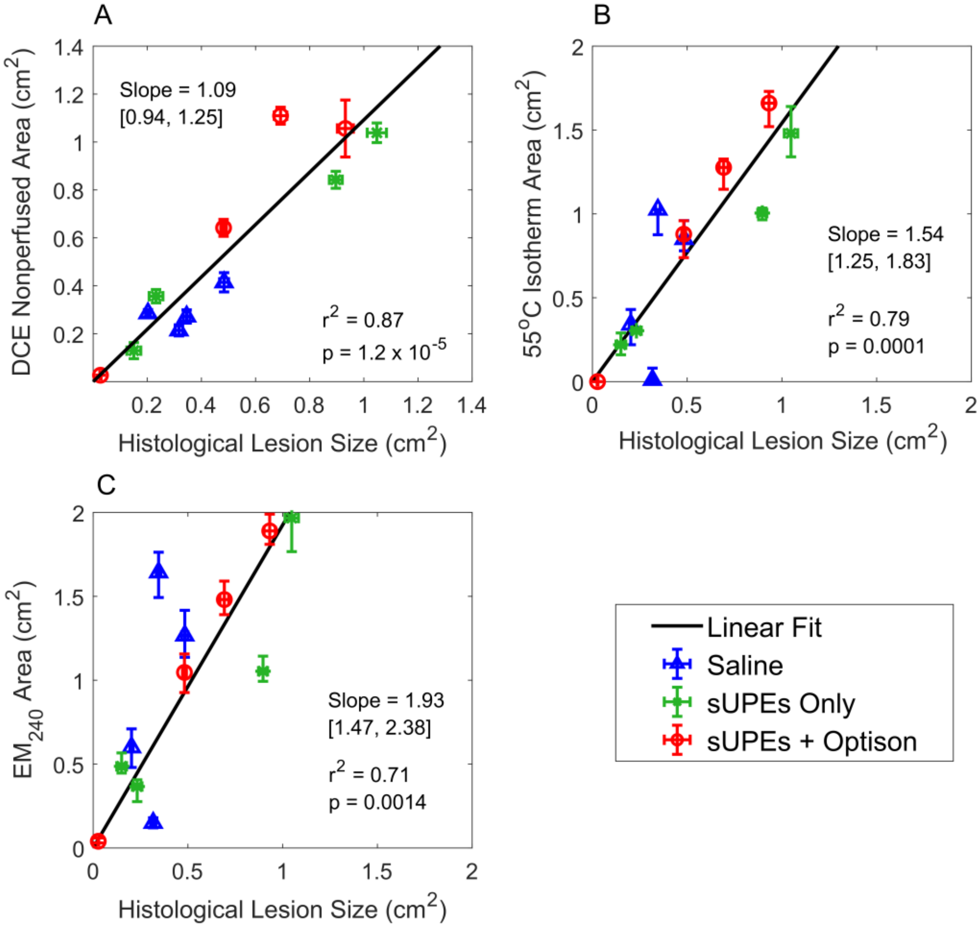

Figure 2.13. Correlation of measured ablative areas from histology and 3T *in vivo* MR imaging estimates. (A) Non-perfused area in DCE images as a function of histological lesion area. (B) Area within 55°C isotherm as a function of histological lesion area. (C) Area of thermal dose ≥ 240 CEM_{43} as a function of histological lesion area. Slopes of linear fits are given as the fitted slope and 95% confidence interval (in brackets). Error bars in histological areas and NPAs are standard deviations of triplicate measurements. Error bars in 55°C isotherms and thermal dose measurements were computed by propagating the temperature uncertainty, as described in the methods. Only canines receiving all three treatments are included.

2.4 Discussion

2.4.1 Transition of sUPEs and MR contrast

The purpose of this study was to quantify TULSA insonation of sUPEs via T_1 contrast, morphology of prostate ablation, and imaging-based treatment assessment in a canine prostate model. To assess transition of the sUPEs, the MR contrast agent Gd_2O_3 was incorporated into the sUPE shell interior. No significant differences in T_1-contrast were observed in the insonation zone between treatment arms, indicating limited transition of the sUPEs, although the sample size limits interpretation of these results. Qualitatively, no clear enhancement in T_1W images was observed that was specific to the experimental arms and could be confidently attributed to MR contrast from transitioned sUPEs. The transition of phase shift emulsions is a stochastic process, with transition being most likely beyond a frequency-dependent pressure threshold.[145] The spatial peak, temporal-peak negative pressure of the ultrasound array used in this study was approximately 2-2.2 MPa. This pressure is near the threshold to transition protein-shell UPEs,[145] but the silica shell may act to increase the threshold for sUPE transition. T_1-contrast is highly dependent on the concentration of Gd, and so a limited number of transitioned sUPEs would not be apparent on T_1W images.

Physical properties of the MR contrast particles can affect the T_1-contrast. Park et al.[146] and Rahman et al.[147] showed that Gd_2O_3 nanoparticles with diameters in the range of 1-2.5 nm exhibit the greatest T_1-relaxivity. Ahrén et al. explored surface functionalization and dialysis of Gd_2O_3 nanoparticles and found that PEGylated Gd_2O_3 nanoparticles, when dialyzed for 6 days, exhibit T_1-relaxivities over twice as high as uncapped nanoparticles and over four times higher than Gd-DTPA chelates.[148] Although the nanoparticles used in this study were approximately 2 nm in diameter, the lack of surface ligands may have allowed for surface charge and consequent particle aggregation, reducing the effective T_1-relaxivity. Furthermore, the nanoparticles may sinter with one another and with the inner wall of the silica shells during the calcination process. The MR contrast formulation encapsulated by the sUPEs should be refined in future work to maximize T_1-contrast efficiency (and thus minimize the dose required per procedure) and establish an acceptable toxicity profile. The presence of residual microbubbles following insonation and sUPE transition may have also introduced confounding susceptibility effects,[149, 150] masking signal enhancement from released Gd_2O_3. An ultrasonic bubble-deleting pulse applied between ablation and MR imaging may help to mitigate this effect.[151]

Only minimal movement of sUPEs was expected in tissue, as similar sUPEs were found to persist spatially in flank tumors *in vivo* for four days, even after multiple Doppler imaging acquisitions with peak negative pressures of approximately 5 MPa.[92] In contrast, the studies here were conducted over the course of several hours. Some degree of diffusion or washout of the particles may have taken place nonetheless during therapy and imaging, reducing the concentration present in the tissue. Radiation force from the TULSA insonation may have exacerbated this effect, pushing and dispersing the injection bolus.[152] This dispersion could explain the apparent non-localized enhanced heating in the experimental treatment arms. Difficulties in visualizing and confirming injection sites also underscore the need for an IV injection and targeted sUPEs that accumulate preferentially at tumor locations. A study involving intravenous injection of similar 500-nm particles has demonstrated uptake and retention in LnCAP prostate tumors implanted in the flanks of mice for an average of 3.3 days.[81] When tumor-specific folate functionalization was added, the particles' *in vivo* lifetime was extended to 12 days.[81]

2.4.2 Enhancement of thermal therapy with sUPEs

To increase the likelihood of sUPE transition with the TULSA device, a treatment arm combining sUPEs with Optison microbubbles was explored. Ultrasound exposure of microbubbles induces strong cavitation activity.[153] Under the proper insonation conditions,[154] inertial cavitation associated with strong acoustic emissions can be induced[155] that may trigger sUPE transition. No change in T_1-signal, heating rate, or ablation zone size was observed in this study in the presence of sUPEs or Optison, although experimental arms exhibited a wider range of lesion sizes and temperatures. Observations of thermal fixation were more frequent in sUPEs and sUPEs with Optison treatment arms, possibly indicating an enhanced heating mechanism resulting from cavitation activity of microbubbles or transitioned sUPEs. Limited microbubble activity likely occurred temporally throughout the insonation, however, as the pressure amplitude was sufficient to result in rupture of the shelled microbubbles.[154] The onset of shell rupture is concurrent with microbubble dissolution and loss of echogenicity,[156] indicating loss of prompt cavitation nuclei to induce inertial cavitation. Further studies are required to quantify the type and dose of cavitation activity from TULSA exposure of microbubbles, and to devise insonation schemes for sustained cavitation activity.[109, 157]

While a limited number of sUPEs were likely transitioned, they had a marked effect on the lesion morphology. All lesions consisted of contiguous areas of non-viable tissue. Six of nine treatments including sUPEs and one of five saline sham treatments exhibited tissue that was thermally fixed.[118, 143, 144] This “heat-fixed” tissue has a paradoxically untreated appearance on H&E staining. In contrast, other biomarkers such as triphenyl tetrazolium chloride (TTC) or cytokeratin 8 (CK8) have been shown to indicate non-viability of heat-fixed tissue.[118, 158] In addition to being more frequent in the experimental treatment arms, the presence of thermal fixation correlated significantly with larger lesions and higher therapeutic temperatures, indicating that the presence of sUPEs could enhance heat deposition with TULSA. Intravenous injection of functionalized or ligand-targeted sUPEs may improve the specificity of sUPEs for prostate cancer tissue,[81, 159] enhancing TULSA ablation of target areas. Increased absorption by sUPEs would also shield distal structures, allowing extension of treatment margins around the target. However, the wide range of lesion sizes and temperatures observed for the experimental arms indicates that therapeutic enhancement imbued by sUPEs may come at a cost of reduced consistency in treatment outcome. This inconsistency may stem from the stochastic nature of droplet transition, or from excess shielding of the acoustic field from transitioned droplets or microbubbles.[127] Such variable therapeutic efficacy could increase the risk of untreated residual disease, although the areas of ablation zones are still reliably assessed via MR imaging metrics (see Fig. 8). Previous studies have found that bubble activity from droplets or microbubbles can provide controlled heating[78–80, 127, 160] and can be monitored with passive ultrasound imaging techniques.[47] In order to reduce the inconsistencies in the experimental treatment arms observed in this study, the acoustic output should be modulated based on feedback of cavitation activity via passive cavitation imaging,[50, 110, 111] plane wave B-mode imaging,[161–163] or color Doppler imaging.[164, 165]

2.4.3 *MR imaging and thermometry for evaluation of treatment*

The observation of thermal fixation with histology was related to some qualitative features of T_2W and diffusion-weighted imaging, suggesting that such enhanced heating could be ascertained *in vivo*, independently from histopathological analysis. In particular, ADC maps both *in vivo* and *ex vivo* indicated that heat-fixed tissue did not always exhibit reduced diffusion as non-heat-fixed ablated tissue did. ADC values for both untreated and thermally necrosed tissue *in vivo* agreed with those reported by Chen et al.[166] and Pauly et al.[139] However, the observed pattern was contrary to these studies, in which contiguous regions of reduced diffusion were observed post-therapy, even when thermal fixation was present.[139, 166] Decreases in T_2W image intensity have been previously reported following thermal ablation of the prostate but with little consistency across treatments, and no clear delineation of treatment boundaries.[84] The results of this work suggest that T_2W image hypointensity corresponds with thermal fixation, and is therefore only likely to be observed for rapid heating of tissue to high temperatures. However, T_2W images were difficult to interpret in highly cystic prostates.

In this study, we observed a significant correlation between standard imaging benchmarks (DCE NPAs, 55°C isotherms, and thermal dose boundaries) and histology when considering all treatment arms together. Correlation coefficients ranged from 0.50-0.69 for the sham arm, and 0.91-0.99 for arms involving sUPEs. The areas of lesions generated in the saline sham arm were within 0.20–0.48 cm^2, providing a smaller range over which to compute the correlation in comparison to arms including sUPEs (0.03–1.05 cm^2). In a similar study, Partanen et al. found a significant correlation between the ablation zone, DCE NPA, and thermal dose induced via TULSA in the absence of any pre-treatment injection.[68] However, Partanen *et al.* stained prostate tissue samples with CK8, which would modify the observed lesion morphology compared to the H&E stain utilized in this study.[167]

MR thermometry measurements in this work exhibited some discrepancies with previous studies. When considering all treatment arms, non-perfused regions were only 10% larger on average than ablated areas on histology, while estimates of lesion sizes based on 55°C isotherms and 240 CEM_{43} dose boundaries were approximately 1.4 and 2 times as large as histological measurements, respectively. Several studies in canines have reported good agreement between 240 CEM_{43} dose boundaries, 52°C isotherms, and thermal coagulation assessed histologically, but many observations are only qualitative.[139, 168] Previous studies have also denoted an outer boundary of delayed cell kill in histopathological sections of prostates treated with TULSA, suggesting a time dependence for complete lesion formation.[35, 117, 118] These works report agreement between histologically necrotic tissue, 240 CEM_{43} dose boundaries, and lower-temperature isotherms (50–52°C) 24–48 hours after treatment in canines. Burtnyk et al.[35] list 240

CEM_{43} as the thermal dose corresponding to delayed cell kill, rather than acute coagulation. Therefore, some discrepancy between acute histology and 240 CEM_{43} of thermal dose is expected. While the 55°C isotherm has been shown to accurately predict the extent of thermal coagulation in the prostate,[35, 66, 117] some degree of patient-specific variation has been observed. Chopra et al. showed agreement between $10^{3.9}$ CEM_{43} dose boundaries, 56.2°C isotherms, and the coagulation boundary in canines.[117] Chopra et al. also reported average peak temperatures ranging from 49–56°C and doses of 110–17,000 CEM_{43} at the acute damage boundary across only 8 human subjects.[66] In the work presented here, non-rotational ablations were applied, which may complicate thermometry estimation compared with ablation of large sectors or whole glands. Indeed, a similar overestimation of statically ablated volume was recorded by Partanen et al.,[68] in which thermal dose estimates were 1.5-2 times greater than histological volumes, DCE NPVs, and volumes of reduced diffusion on DWI. The histological measurements in the current study did not account for shrinkage of the excised tissue, which may have resulted in smaller histological lesion areas. Additionally, during some insonations, slight prostate displacements occurred due to peristalsis, which could induce errors in temperature measurement. No apparent sudden changes in the temperature distribution of the treatment zone were observed during these movements.

The presence of an MR contrast agent can produce local susceptibility effects, confounding the estimated temperature measurement.[169, 170] No discrepancies between MR thermometry and other methods of treatment assessment that were specific to the experimental arms were observed in this study. For the concentrations of Gd_2O_3 employed in this study, the error in the temperature measurements would be less than 1°C based on data reported by Hijnen et al.[169]

However, these results refer to aqueous contrast agent, and do not necessarily reflect the errors associated with the use of Gd_2O_3 nanoparticles.

2.4.4 Limitations of study

The frequency of the 3.75-MHz prototype TULSA system employed in these studies could not be modified due to hardware limitations. Simulation and phantom studies have demonstrated that dual-frequency transducers offer better coverage and more precise, rapid ablation than single-frequency devices.[171] Previous canine studies have primarily utilized frequencies ranging from 6–9 MHz to achieve successful ablations with minimal far field heating.[68, 69, 117, 139] Inhomogeneous ablation can be observed for static 4-MHz excitations (20 W/cm^2 acoustic power) when treating prostate radii less than 16 mm.[172, 173] This, combined with the known decrease in droplet transition threshold pressure with increasing frequency,[145] indicate that the use of a low frequency device may have contributed to the variability observed in this study. The use of higher frequency or multi-frequency devices would likely improve treatment consistency and more effectively transition sUPEs for therapeutic enhancement.[145, 173] Future studies should explore the most clinically appropriate acoustic field based on the disease morphology.

Treatment planning and monitoring was conducted via the iSuite interventional system, which has not previously been utilized with a TULSA device. The iSuite prototype was designed for device guidance during interventions. Simultaneous temperature mapping can be achieved in up to three parallel slices. To better monitor and estimate the entire volume of ablative thermal dose, processing of flexible arrangements of multi-slice thermography sequences should be implemented. Currently, most therapy guidance platforms cannot be immediately integrated with TULSA treatment planning software and delivery systems, requiring manual adjustment of therapeutic insonation. Such integration would allow automatic modulation and shutoff of applicator elements based on temperature feedback from the thermometry measurements, ensuring safer, more conformal delivery of thermal dose to the prostate. Nonetheless, the iSuite platform enabled easy localization of the applicator and injection needle and effective treatment planning and monitoring. In the clinic, iSuite could be utilized to guide placement of the TULSA applicator and endorectal cooling device in real-time, or to guide prostate tissue biopsies.

This study contains several other limitations. The small number of subjects used (6 animals, 15 insonations) limits the reliability of statistical analysis. For all applications of the TULSA device (10 insonations in 6 subjects), appreciable change in T_1 contrast was not observed and a lack of consistency in therapeutic outcome was noted. Thus, studies were suspended. This work reports results of TULSA ablation of healthy canine prostate tissue, which may not reflect treatment response in a cancer model. The direct injection of sUPEs also does not replicate an IV infusion, in which case the sUPEs may require surface modification and additional delay time between injection and therapy in order to ensure sufficient accumulation in the target tissue.

While insonation of sUPEs in this work may indicate therapeutic enhancement, further study is required to optimize sUPEs' therapeutic and contrast properties. Some MR imaging features in this study suggest that enhanced heating and thermal fixation could be visualized *in vivo*, even if sUPE transition is not directly apparent. The differences observed between histological measurements of the lesion area and MR thermometry-based metrics in this study indicate a need for more robust tools for TULSA treatment monitoring and assessment. Future studies should investigate sUPE transition with TULSA insonation schemes to determine the optimal parameters for consistent droplet transition and therapeutic outcome. This study nonetheless shows promise for sUPE-enhanced TULSA and demonstrates the utility of the iSuite interventional system in TULSA procedures. This work also suggests that MR imaging metrics for TULSA treatment evaluation are not compromised when performed in tandem with sUPE injection.

2.5 Conclusions and future work

Silica-shell phase shift emulsions were insonified in a canine prostate model to test their effect on therapy and on the ability to assess treatment outcome of TULSA prostate ablation. A novel MR interventional suite was used for image guidance and treatment evaluation. A significant correlation between histologically nonviable areas, MR thermometry-based estimates, and DCE NPAs was observed when examining all treatment arms together. The presence of sUPEs did not diminish the accuracy of these metrics in estimating ablative areas. DCE NPAs provided the most accurate estimate of acute cell death following TULSA therapy, with 55°C isotherms and 240 CEM_{43} dose boundaries overestimating histological lesion sizes by a factor of 1.4 and 2.2, respectively. The lesion morphology was also modified for arms containing sUPEs compared with saline alone, indicating more frequent thermal fixation due to rapid heating that correlated with some imaging metrics. While this may indicate enhanced heat deposition by sUPEs, lesion sizes and temperatures were less consistent in these arms and did not indicate more localized heating than the saline arm. T_1 contrast indicating sUPE transition was also not apparent. Further studies are thus required to ascertain the mechanism of action of these particles and optimize their therapeutic and diagnostic properties. However, these results indicate that an exogenous agent may be a key element in the improvement of TULSA therapy.

CHAPTER 3

ASSESSMENT OF HISTOTRIPSY-INDUCED LIQUEFACTION WITH DIAGNOSTIC ULTRASOUND AND MAGNETIC RESONANCE IMAGING IN VITRO AND EX VIVO

The work presented in this chapter has been published as: G.J. Anthony, V. Bollen, S. Hendley, T. Antic, S. Sammet, and K.B. Bader, Assessment of histotripsy-induced liquefaction with diagnostic ultrasound and magnetic resonance imaging *in vitro* and *ex vivo*, Phys Med Biol **64**(9), 095023 (2019).

3.1 Introduction

As explored in Chapter 2, image-guided high intensity therapeutic ultrasound is a non-invasive modality for tissue ablation.[30, 33, 67, 82, 174] However, this thermal modality proved insufficient to transition a large number of theranostic silica particles, and the enhanced heating effect imparted by particles that did transition was highly inconsistent. Chapter 3 of this dissertation therefore explores a different and relatively novel therapeutic ultrasound modality: histotripsy. Histotripsy ablates tissue via the nucleation and mechanical activity of bubble clouds, imparting lethal strain to target tissues.[40, 41, 44, 175] Pre-clinical studies have applied histotripsy in the treatment of prostate tissue, liver and renal cancer, thrombosis, and stimulation of anti-tumor immune response.[44] Additionally, a clinical trial was completed assessing the safety of histotripsy technology to treat benign prostatic hyperplasia.[176]

Successful clinical implementation of histotripsy requires accurate and reliable image guidance to assess the treatment progress and efficacy. The presence of histotripsy-induced bubble activity and the resulting tissue homogenization has been monitored with diagnostic ultrasound and magnetic resonance (MR) imaging.[47–50, 52–56] Bubble clouds appear hyperechoic on B-mode imaging, and the strength of bubble cloud emissions can be mapped spatially with passive cavitation imaging (PCI).[50, 110, 111, 177–179] Following histotripsy exposure, regions of tissue liquefaction can be assessed with B-mode imaging.[44, 180] A significant variability in the B-mode grayscale of ablation zones is observed between subjects, preventing quantification of the tissue liquefaction zone with B-mode imaging.[164, 181] Diagnostic ultrasound is typically a two-dimensional imaging modality, while MR imaging provides excellent soft tissue contrast over a volume with the potential for isotropic resolution.[52–56] Strong changes in MR contrast have been reported following histotripsy liquefaction.[53–56] Combinations of diagnostic ultrasound and MR imaging have been implemented for thermal-based therapies[179] and phase shift nanoemulsion-nucleated bubble activity during heating,[178] and may be an attractive multimodal option for histotripsy guidance.

The purpose of this study was to determine the relative utility of diagnostic ultrasound or MR imaging to predict histotripsy liquefaction. Histotripsy-induced bubble cloud activity was mapped with passive cavitation imaging (PCI) and plane wave imaging. Regions of liquefaction were visualized with conventional B-mode ultrasound and MR imaging. The relationship between histotripsy liquefaction and changes in MR or diagnostic ultrasound features were assessed quantitatively in agarose phantoms and *ex vivo* porcine liver.

3.2 Materials & Methods

3.2.1 In vitro phantom preparation

Tissue mimicking agarose phantoms containing 15% v/v porcine red blood cell (RBC)/agarose layers were constructed following Maxwell *et al*.[182] Briefly, 50 mL of unspecified citrate-phosphate-dextrose porcine blood was obtained from a commercial vendor (Lampire Biological, Pipersville, PA, USA), and centrifuged at 3,000 RPM for 10 minutes. The plasma and buffy coat supernatant were removed, leaving a pellet of RBCs. A 1% w/v agarose, 0.9% w/v NaCl (Sigma-Aldrich, St. Louis, MO, USA) solution was prepared using 0.2-µm filtered, deionized water and heated in a microwave at 700 W until clear. The agarose mixture was then transferred to a heated ultrasonic cleaning bath and degassed (50 kPa, 50% atmospheric pressure) for 30 minutes. After degassing, approximately 50 mL of the agarose mixture was poured into a custom acrylic mold (6 x 5 x 5 cm^3) with nylon wires embedded to serve as fiducial markers. After solidification of this layer, a layer of 15% v/v RBC/agarose mixture approximately 500 µm thick was pipetted onto the surface. This process was repeated to generate three RBC layers separated by 1.5 cm, after which the phantom was stored at 4°C overnight (Figure 3.1a). Prior to histotripsy exposure, the phantoms were submerged in isotonic saline (0.9% NaCl w/v) and degassed (50 kPa pressure) for two hours.

3.2.2 Phantom preparation with ex vivo liver samples

Porcine liver samples were collected from an abattoir and shipped fresh within 24 hours via a commercial vendor (Lampire Biological, Pipersville, PA, USA), then cut to approximate dimensions of 6 cm x 3 cm x 1.5 cm. Liver samples were embedded in degassed, isotonic (0.9% NaCl w/v) 2% w/v low-gelling temperature agarose (product number A0701, Sigma-Aldrich, St. Louis, MO, USA) and stored at 4°C overnight (Figure 3.1b). Prior to embedding the liver samples, the liquid agarose mixture was cooled to 40°C. No thermal damage was evident upon histologic inspection of tissue samples. Prior to histotripsy exposure, the embedded samples were submerged in degassed isotonic saline (0.9% NaCl w/v) and degassed (50 kPa pressure) for two hours.

3.2.3 Phantom preparation with in vitro blood clot samples

After local institutional review board approval and informed written consent, venous whole blood was drawn from patients undergoing invasive catheterization procedures at the University of Chicago Medicine cardiac catheterization laboratory. Following an established protocol,[183, 184] in vitro clots were then produced in Pasteur pipettes (14.6 cm length, 2 mL capacity, Fisher Scientific, Hanover Park, IL, USA). Clots were approximately 4 mm in diameter. The clots were removed from the pipettes by gently flushing with isotonic saline (0.9% NaCl w/v), and suspended in the acrylic mold with nylon thread. An isotonic (0.9% NaCl w/v) low-gelling temperature liquid agarose mixture (2% w/v) was cooled to 40°C and poured into the mold. The agarose was allowed to solidify, after which the agarose-embedded clot was stored at 4°C overnight (Figure 3.1c).

3.2.4 Insonation and monitoring bubble activity

After degassing, phantoms were submerged in a tank of degassed (20% dissolved oxygen), filtered (10-µm pore size) water and affixed to a motor-controlled three-axis positioning system (TDC001, Thorlabs, Inc., Newton, NJ, USA) (Figure 3.2). Histotripsy pulses were generated using a custom designed and built transducer and amplifier system[185] (1-MHz center frequency, 90-mm focal length, 100-mm diameter, -6 dB focal zone dimensions: 10 mm x 2 mm x 2 mm). A total of 4,000 pulses 5 µs in duration[186] were applied to each RBC layer with a pulse repetition frequency (PRF) of 100 Hz and peak negative pressures of 13, 17, 21, or 25 MPa. The peak negative pressures employed in this study span those previously used to successfully generate bubble activity via a shock-scattering mechanism.[44, 175, 187] Exposure conditions were randomized for each RBC layer. During the insonation, bubble cloud acoustic emissions and hyperechogenicity generated by the bubble cloud were recorded with an L11-4v imaging array

(Verasonics, Inc., Kirkland, WA, USA) using a research ultrasound scanner system (Vantage 128, Verasonics, Inc., Kirkland, WA, USA) triggered by the histotripsy transmit electronics.[47] Briefly, bubble cloud emissions were passively received over a 60-μs duration starting 5 μs prior to the 5-μs duration histotripsy pulse reaching the focus (Figure 3.2b). Emissions were processed offline to generate passive cavitation images with a delay, sum, and integrate method in the frequency domain over the receive bandwidth of the imaging array (2–10 MHz).[50]

Bubble cloud hyperechogenicity is the primary method by which histotripsy therapy is guided.[181] Several milliseconds are required to execute the imaging sequence for conventional B-mode imaging, over which time the bubble cloud can undergo significant changes.[46, 188] Here, bubble cloud grayscale was assessed over a 20 μs window using plane wave imaging. To minimize constructive interference between the imaging and therapy pulses, the plane wave image was acquired 1 ms after the histotripsy focal insonation.[47] During the 4000 applied pulses, plane wave images and cavitation emissions used to form passive cavitation images were acquired every tenth trigger pulse due to data transfer rate limitations (Figure 3.2b), resulting in 400 frames per data set. In total, 33 insonations were performed in 11 different RBC phantoms.

Insonation and data acquisition for *ex vivo* liver and *in vitro* clot samples were performed as described above, in three locations along the length of the sample (Figure 3.1). A fixed peak negative pressure of 25 MPa in liver samples and 18 MPa in clot samples was employed to achieve consistent liquefaction. For the liver samples, the peak negative pressure was derated to account for propagation through 1 cm of liver tissue with an attenuation coefficient of 0.32 dB $\mathrm{cm^{-1}}$ $\mathrm{MHz^{-1}}$.[189] To achieve consistent liquefaction in the liver samples, the total number of pulses was increased to 8,000. In total, four liver samples were insonated, with three insonations per sample (12 total data sets). A total of 4,000 pulses were generated in three locations in each of three clot samples (nine total data sets).

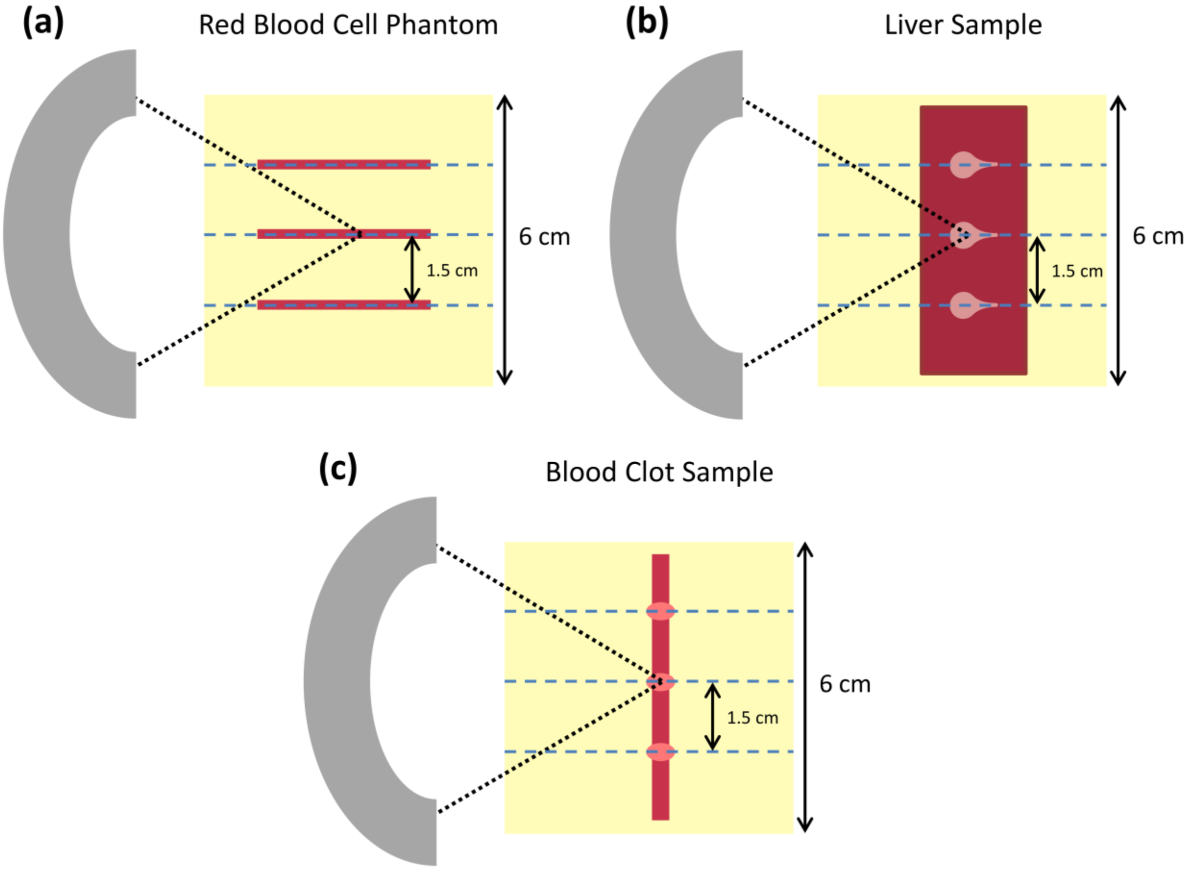

Figure 3.1. Top-down view of experimental setup for phantoms containing (a) red blood cell layers, (b) liver samples, and (c) clot samples. Three locations were targeted with the therapy source (shown in gray on the left) in each phantom, separated by 1.5 cm. In red blood cell phantoms, agarose was poured in layers, with thin blood cell layers (red lines) applied via pipette on top of each solidified agarose layer. Additional fiducial markers (indicated by blue dotted lines) were used to orient the diagnostic ultrasound images, magnetic resonance (MR) images, and collected histologic samples parallel to the direction of ultrasound propagation.

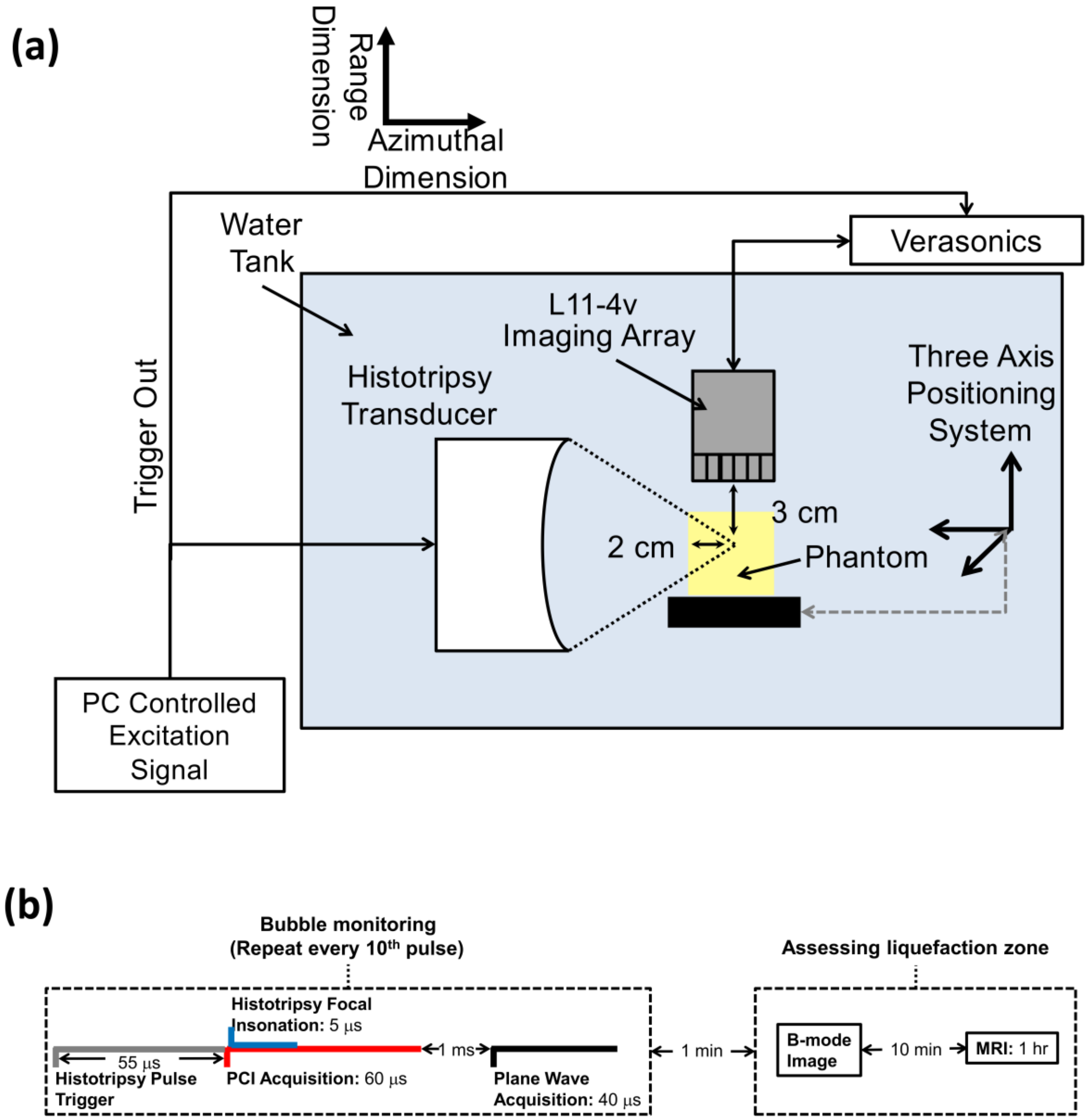

Figure 3.2. (a) Side view of experimental setup for red blood cell (RBC) phantom insonation with a therapeutic ultrasound transducer. RBC layers of the phantoms were oriented parallel to the direction of ultrasound propagation from the histotripsy source. Fiducial markers embedded within the agarose were used to register diagnostic ultrasound and magnetic resonance (MR) images to digital photographs of phantoms post-insonation. The imaging plane of the L11-4v imaging array was registered to the RBC layers and visualized bubble activity along the acoustic axis of the histotripsy source. (b) Timeline of all image data acquisition. Passive and plane wave acquisitions were acquired every tenth histotripsy pulse due to data transfer rate limitations. Post hoc conventional B-mode images were acquired within 1 min of the histotripsy insonation. Samples were transferred to the MR scanner within 10 min, and MR images were acquired over the course of 1 hour.

3.2.5 Post hoc assessment of liquefaction: Conventional B-mode and MR imaging

Image acquisition time relative to application of the histotripsy pulses is outlined in Figure 3.2b. Liquefied tissue appears as hypoechoic regions on conventional B-mode imaging.[44, 180, 181] For all samples, conventional B-mode images of the histotripsy target were acquired following the histotripsy insonation using the L11-4v imaging array to visualize the liquefaction zone. The purpose of these B-mode images was post hoc assessment of the histotripsy therapeutic efficacy. In contrast, plane wave images were employed to visualize the hyperechoic bubble cloud. The confluence of the hyperechoic bubble activity with hypoechoic changes in the material prevented assessment of the sample liquefaction during application of the histotripsy pulse. All samples were then imaged with a clinical 3 Tesla (3T) MR scanner (Ingenia dStream, Philips Healthcare, Best, The Netherlands) using the body transmit coil and a 16-channel head-and-neck receive coil. Samples were submerged in Fomblin® (Solvay Specialty Polymers, Bollate, MI, Italy) during imaging to isolate the target signal from background and prevent parallel acquisition ghosting artifacts. Image slices were oriented parallel to the acoustic axis of the histotripsy source (azimuthal dimension of the diagnostic ultrasound imaging array, Figure 3.2). The scan parameters for MR image acquisition are listed in Table 3.1. Spin-echo (SE) and turbo-spin-echo (TSE) sequences were executed to acquire T_1- and T_2-weighted (T_1W and T_2W) images. Inversion-recovery (IR), multi-echo SE, and diffusion weighted imaging (DWI) sequences were utilized to quantify the relaxation times T_1 and T_2, and the apparent diffusion coefficient (ADC) in the liquefaction zone. For the IR, multi-echo SE, and DWI sequences, the inversion time (TI), echo time (TE), and diffusion-weighting *b*-value were varied, respectively, across multiple acquisitions. From these sequences, T_1, T_2, and ADC were calculated on a voxel-by voxel basis by fitting magnitude image intensities to the following equations as a function of TI, TE, and *b*-value, respectively:[137, 141, 190]

$$S = \left|S_0\left(1 - 2e^{-TI/T_1} + e^{-TR/T_1}\right)\right|, \tag{1}$$

$$S = S_0 e^{-TE/T_2}, \tag{2}$$

$$\ln(S) = \ln(S_0) - b \cdot ADC, \tag{3}$$

where S is the signal amplitude of a magnitude image voxel, and S_0 is the fitted maximum signal amplitude as a function of TI, TE, or *b*-value. The parameters T_1, T_2, and ADC were estimated from least squares fits to equations (1), (2), and (3) implemented with MATLAB software (MathWorks, Natick, MA, USA).

Table 3.1: MR scan parameters used for 3T imaging and parametric mapping of T1, T2, and ADC.

Sequence	TR/TE (ms)	In-plane resolution (acquisition) (mm^2)	Array size (recon matrix)	Slice thickness (mm)	NSA	Echo factor	TI (ms)	b-values (s/mm^2)
T_1W SE	600/10	1.0 x 1.0	192 x 192	2	2	N/A	N/A	N/A
T_2W TSE	4000/100	0.7 x 0.7	224 x 224	2	4	16	N/A	N/A
T_1 mapping (IR)	7000/7	0.7 x 0.7	224 x 224	2.5	1	6	50, 100, 250, 500, 750, 1000, 2500, 5000	N/A
T_2 mapping (multi-echo SE)	4000/20, 40, 60, 80, 100	0.7 x 0.7	224 x 224	2.5	2	5	N/A	N/A
ADC mapping for RBC phantoms (DWI EPI)	5000/160	1.0 x 1.0	384 x 384	3	12	115 (EPI)	N/A	0, 250, 500, 750, 1000
ADC mapping for liver samples (DWI EPI)	5000/69	1.2 x 1.2	176 x 176	4	24	27 (EPI)	N/A	0, 250, 500, 750,
ADC mapping for blood clot samples (DWI TSE)	5000/73	1.5 x 1.5	384 x 384	3	6	65 (TSE)	N/A	0, 500, 1000

TR/TE = repetition time/echo time; NSA = number of signal averages; TI = inversion time; T_1W/T_2W = T_1-/T_2-weighted; SE/TSE = spin echo/turbo spin echo; IR = inversion recovery; ADC = apparent diffusion coefficient; DWI = diffusion-weighted imaging, and EPI = echo planar imaging.

3.2.6 Image registration

Following MR scans, RBC phantoms were sectioned and photographed with a digital single-lens reflex camera (Nikon D3400, 24 MP resolution, Minato, Tokyo, Japan). Fiducial nylon wires embedded within the agarose gel were used to register optical phantom images, diagnostic ultrasound images, and MR images via a custom-scripted landmark-based affine registration implemented in MATLAB (Mathworks, Natick, MA, USA). Gross images were converted to grayscale and segmented using Otsu thresholding[191] to delineate regions of liquefied and intact phantom (Figure 3.3).

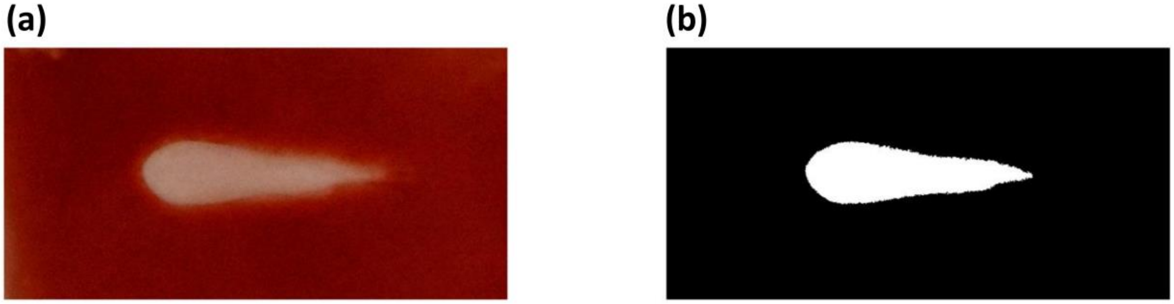

Figure 3.3. Demonstration of Otsu thresholding to generate binary mask of liquefaction zone. Red-green-blue images (a) are converted to grayscale and a global threshold is determined based on the gray level histogram to generate a binary image (b).

Four-millimeter liver sections encompassing the liquefied regions were collected from each insonified region of the liver and clot samples. Sections were fixed for 24–36 hours in 10% buffered formalin (Sigma-Aldrich, St. Louis, MO, USA), transferred to 70% reagent alcohol (Thermo Fisher Scientific, Waltham, MA, USA) for 72 hours, then processed and embedded in paraffin. Embedded tissues were sectioned at 5-μm thickness and stained with hematoxylin and eosin (H&E). Liver tissue slides were reviewed by a board-certified pathologist, who delineated the outer boundary of cellular necrosis as indicated by absence of nuclei and disruption of normal hepatic tissue structure. Minimal changes in tissue sample size occurred due to dehydration from histological processing. Stained liver samples were registered with diagnostic ultrasound and MR images as described above. Registration between imaging and stained clot samples was not possible due to movement of residual clot during fixing and processing. Minimal changes in tissue sample size and shape occurred due to histological processing.

3.2.7 Image analysis

The PCI power, plane wave (uncompressed) grayscale value, and changes in post hoc conventional B-mode (uncompressed) grayscale, T_1, T_2, and ADC from background were independently tested as quantitative predictors of RBC phantom liquefaction or liver tissue necrosis. The plane wave and conventional B-mode image grayscale pixel values are related to the backscattered acoustic power of the ultrasound imaging pulse.[192] Post hoc conventional B-mode grayscale and T_2 exhibited both strong increases and decreases relative to background, and were assessed in terms of absolute change from the baseline signal. ROC curves were generated by varying a threshold across each ultrasound (acoustic power or plane wave/conventional B-mode grayscale) and MR image quantity (T_1, T_2, or ADC) and plotting the true positive rate against false positive rate for prediction of liquefaction/necrosis at each threshold value.[193, 194] The delay, sum, and integrate beamforming algorithm used to form the passive cavitation images in this study is diffraction limited,[50] causing emission artifacts along the range dimension for a linear imaging array (Figures 3.2 and 3.5). Therefore, the ROC analysis was restricted to azimuthal pixels at a fixed range depth of 30 mm. A pixel was considered a true positive (false positive) when it was within the liquefaction zone of an RBC phantom or within the necrosis boundary of a liver sample and the quantitative image metric in question was greater than (less than) the threshold value. A pixel was considered a true negative (false negative) when it was within the intact area of an RBC phantom or outside the necrosis boundary of a liver sample and the quantitative image metric in question was less than (greater than) the threshold value. Areas under the receiver operating characteristic curve (AUCs) were calculated for each quantitative image metric for RBC phantoms and liver samples. The optimal point along the curve, indicative of a threshold value for phantom liquefaction, was identified following Hanley and McNeil.[193]

The sensitivity, specificity, accuracy, and positive and negative predictive values (PPV and NPV) at this threshold point were calculated via:

$$Sensitivity = \frac{TP}{TP+FN}, \tag{4}$$

$$Specificity = \frac{TN}{TN+FP}, \tag{5}$$

$$Accuracy = Sensitivity \cdot P + Specificity \cdot (1 - P), \tag{6}$$

$$PPV = \frac{TP}{TP+FP}, \tag{7}$$

$$NPV = \frac{TN}{TN+FN}, \tag{8}$$

where TP and TN are the true positive and true negative rate, respectively, FP and FN are the false positive and false negative rate, respectively, and P is the overall prevalence of liquefaction/necrosis, or the percentage of azimuthal pixels across all RBC phantoms/liver samples that are within the liquefaction/necrosis zone. Confidence intervals for ROC curves were obtained via bootstrap resampling with 1,000 iterations to test the significance of the AUC relative to random guessing (AUC = 0.5). Significant differences in the above statistics between ROC curves were assessed according to DeLong et al.[195]

The Dice Similarity Coefficient (DSC) was employed to quantify post hoc conventional B-mode and T_2W imaging assessment of the liquefaction zone.[196] Diffusion-weighted and T_1W images were excluded from the DSC analysis, as liquefaction zones were not consistently apparent with these modalities. Passive cavitation and plane wave images acquired during the histotripsy insonation track bubble activity, and are therefore not a direct means to assess the ablation zone. DSC values were computed as:

$$DSC = \frac{2(A \cap B)}{(A+B)}, \tag{9}$$

where $(A \cap B)$ is the area of the intersection of an image-derived liquefaction zone and the true liquefaction zone, and $(A + B)$ is the sum of these two areas. For RBC phantoms and liver samples, DSC values derived from conventional B-mode and T_2W images were compared at each pressure level using paired Student's t-tests. For RBC phantoms, DSC values for 13, 17, 21, and 25 MPa insonations were compared separately using one-way unbalanced analysis of variance (ANOVA) and Tukey's honestly significant difference (HSD) as a post hoc test. Differences in the areas of RBC phantom liquefaction zones as measured from gross observation images were also compared between all pressures using one-way unbalanced ANOVA and Tukey's HSD. All statistical analysis was performed with an α level of 0.05.

Features of diagnostic ultrasound and MR images were also evaluated without comparison to gross observations of histotripsy liquefaction. The azimuthal locations of maximum PCI power, plane wave grayscale, T_1, and ADC, and the maximum and minimum post hoc conventional B-mode grayscale and T_2 relative to the geometric transducer focus were recorded for each RBC phantom data set. Background ROIs were also drawn for each sample in untargeted portions of RBC layers, liver tissue, or blood clot, and the average PCI acoustic power, plane wave and post hoc conventional B-mode grayscale, T_1, T_2, and ADC values within the liquefaction zones and background ROIs were computed. Differences in image parameters between liquefaction zones and background were evaluated using paired Student's t-tests. For RBC phantoms, differences in image parameters between pressures were assessed using one-way unbalanced ANOVA with Tukey's HSD as a post hoc test. All statistical analysis was performed with an α level of 0.05.

3.3 Results

3.3.1 Observation of histotripsy-induced liquefaction

Liquefaction occurred within RBC phantoms at all pressures. For six of eight 13 MPa insonations, "streaks" of inhomogeneous liquefaction were observed at the distal end of the focal zone. As the pressure increased, the liquefaction zone transitioned from a "tadpole" shape to being semi-conical with a wide, flattened head (Figure 3.4, top row). The measured liquefaction area increased significantly with the peak negative pressure of the histotripsy pulse. Targeted areas in liver samples exhibited extensive denucleation and homogenization of cellular membranes and tissue structure that was most pronounced at the head of the liquefaction zone (Figures 3.8a and 3.9a). The outer boundary of observed denucleation (necrosis) was assessed, although some areas of nucleated cells were still present in this region. In blood clot samples, intense hemolysis of the clot structure was observed following histotripsy, with a reduction in residual clot area compared with control clot sections (i.e. unexposed to histotripsy) for all samples. Areas of liquefaction were occasionally evident in the agarose surrounding the clots, suggesting expansion of the histotripsy bubble cloud beyond the clot.

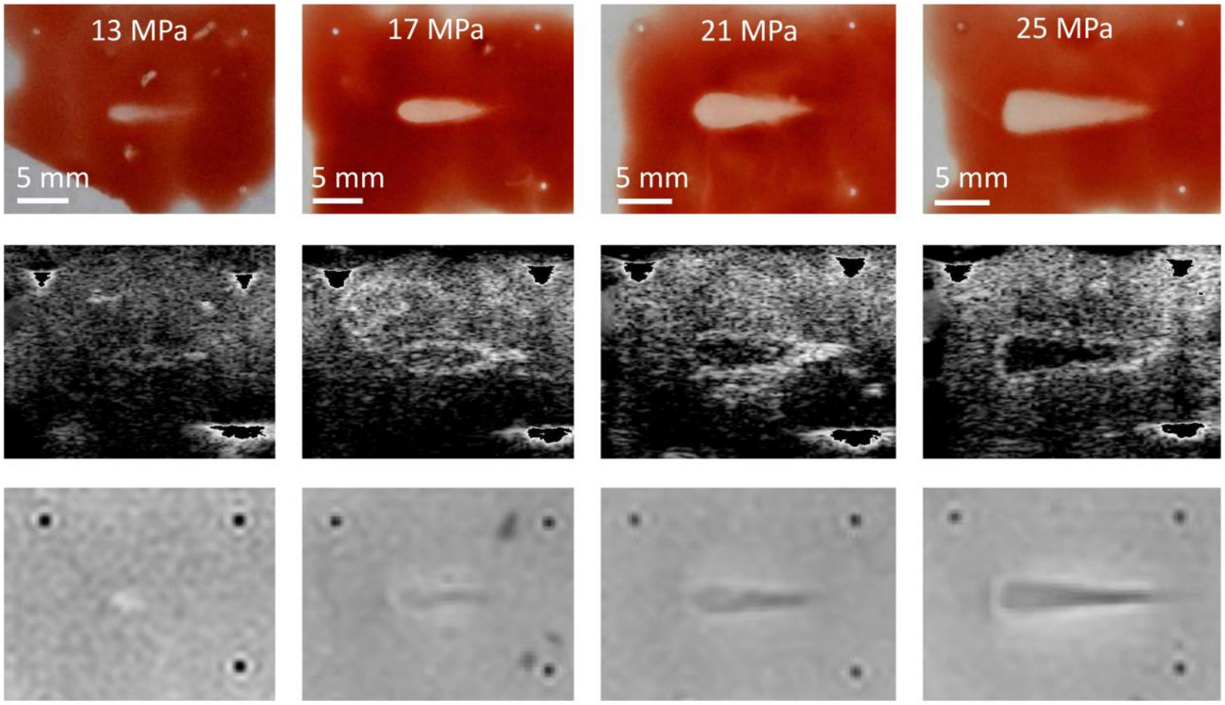

Figure 3.4. Gross observations (top row) and post hoc visualizations of liquefaction zones with conventional B-mode images (middle row) and T_2-weighted images (bottom row). Insonations consisted of 13 (left) 17 (middle-left), 21 (middle-right), or 25 (right) MPa peak negative pressure pulses of 5-μs pulse duration and 1-MHz fundamental frequency in red blood cell phantoms. Therapeutic ultrasound pulses propagated from left to right in all images. In post-insonation conventional B-mode images, fiducial markers have been removed to allow better grayscale windowing for visualization of hypoechoic liquefaction zones.

3.3.2 Monitoring bubble activity with PCI/plane-wave imaging

Table 3.2 displays bubble-monitoring and post-insonation image parameter values measured within liquefaction zones for all phantom and tissue samples. Bubble clouds were generated in all samples for all insonations as indicated by hyperechogenicity on plane wave images and strong acoustic emissions on passive cavitation images (Figures 3.5 through 3.8). Good correspondence was observed between locations of bubble activity, highlighted by hyperechogenicity on plane wave imaging and acoustic emissions on PCI, and histotripsy liquefaction observed in post hoc conventional B-mode and T_2W images (Figures 3.4 and 3.5). RBC phantom liquefaction zones, defined as regions void of red blood cells, were determined using Otsu thresholding[191] (see "Image Registration" in Methods section and Figure 3.3). The PCI power of acoustic emissions within the RBC phantom liquefaction zones increased significantly at each pressure level, while plane wave grayscale values tracking the hyperechoic bubble cloud within liquefaction zones only increased significantly between 13 and 17 MPa insonations. Bubble cloud activity quantified by acoustic power and plane wave grayscale within the liquefaction zones were significantly greater than background values for all phantom and tissue samples. For all RBC phantoms (Figure 3.6), clot samples (Figure 3.7), and most liver samples (Figure 3.8), bubble activity appeared continuously throughout the focal zone. In four of 12 liver samples, bubble activity occurred preferentially along connective, vascular, or ductal structures.

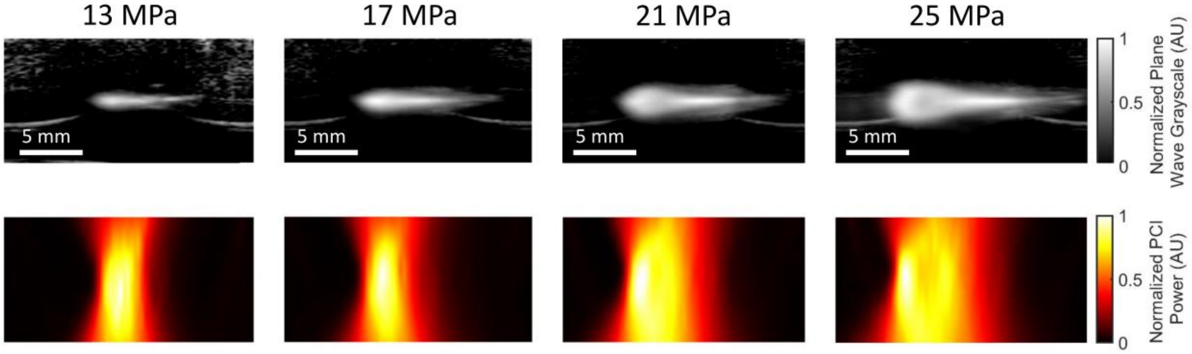

Figure 3.5. Plane wave ultrasound images (top row) and passive cavitation images (bottom row) acquired during histotripsy insonation with 13 (left) 17 (middle-left), 21 (middle-right), and 25 (right) MPa peak negative pressure pulses of 5-μs pulse duration and 1-MHz fundamental frequency in red blood cell phantoms. Therapeutic ultrasound pulses propagated from left to right in all images.

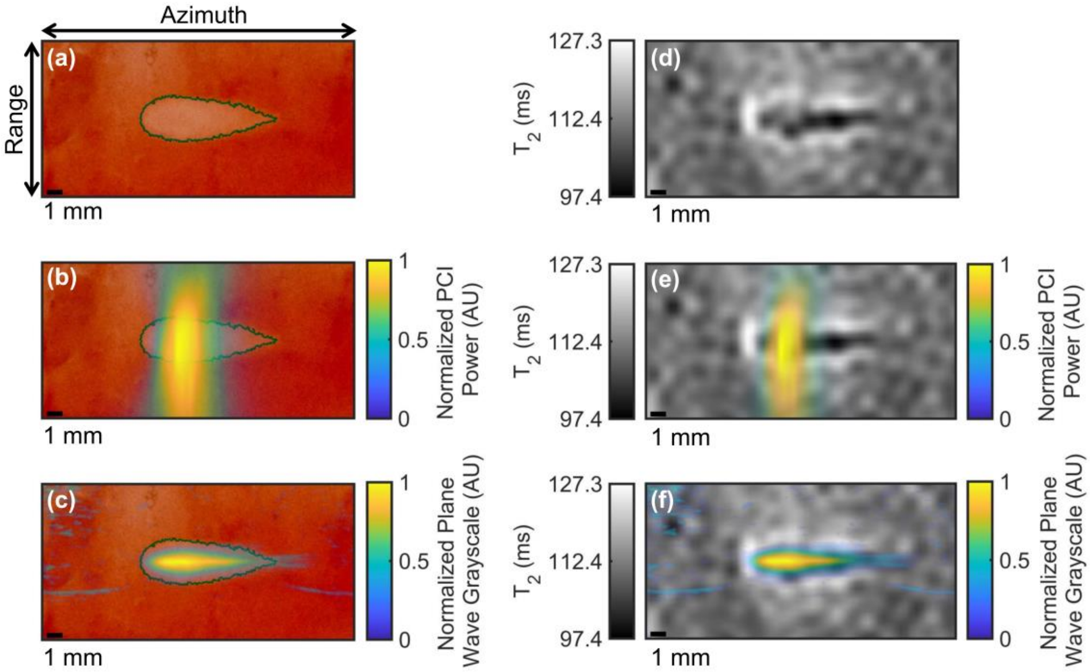

Figure 3.6. Registration of imaging with gross observation of red blood cell phantom liquefaction. (a) Gross observation of liquefaction generated by histotripsy in a red blood cell phantom with the liquefaction zone outlined in green, (b) coregistration of passive cavitation imaging (PCI) acoustic power and red blood cell liquefaction, (c) coregistration of plane wave grayscale and red blood cell liquefaction, (d) parametric T_2 map of red blood cell liquefaction, (e) coregistration of PCI acoustic power and T_2 map, and (f) coregistration of plane wave grayscale and T_2 map. The liquefaction zone outline is shown in panels (a), (b), and (c). The histotripsy pulse (1-MHz fundamental frequency, 5-μs pulse duration, 17-MPa peak negative pressure) propagated from left to right in the image. The azimuth/range dimensions of the diagnostic ultrasound imaging plane are indicated in panel (a).

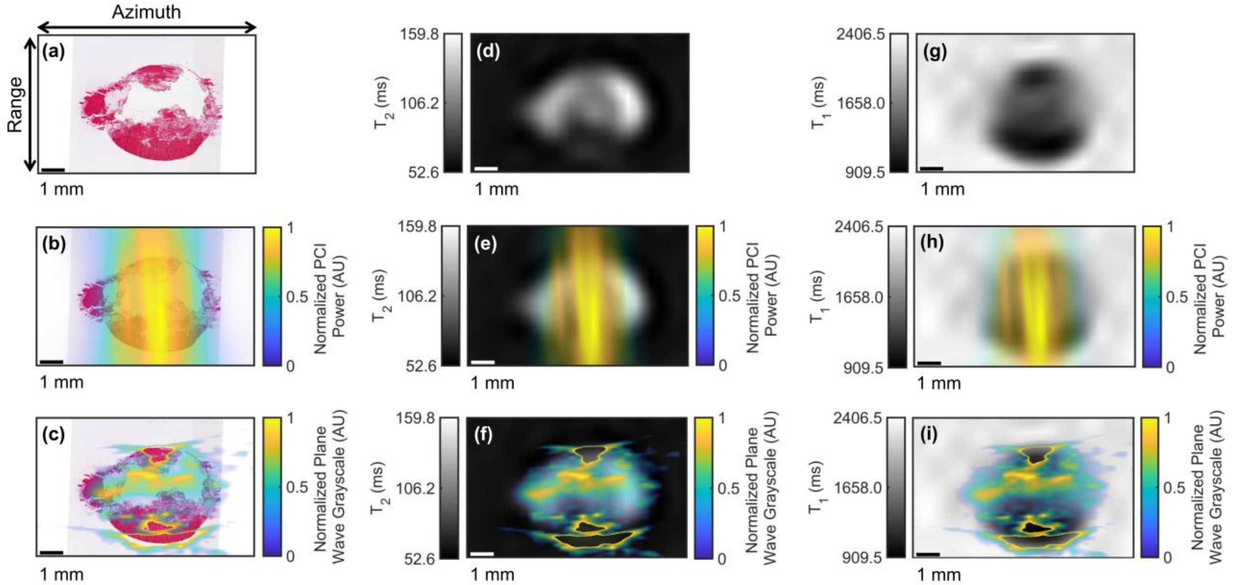

Figure 3.7. Registration of imaging with histologic observation of blood clot sample liquefaction. (a) H&E-stained treated blood clot sample, (b) coregistration of passive cavitation imaging (PCI) acoustic power and H&E-stained clot sample, (c) coregistration of plane wave grayscale and H&E-stained clot sample, (d) parametric T_2 map of treated clot sample, (e) coregistration of PCI acoustic power and T_2 map, (f) coregistration of plane wave grayscale and T_2 map, (g) parametric T_1 map of treated clot sample, (h) coregistration of PCI acoustic power and T_1 map, and (i) coregistration of plane wave grayscale and T_1 map. The histotripsy pulse (1-MHz fundamental frequency, 5-μs pulse duration, 18-MPa peak negative pressure) propagated from left to right in the image. The azimuth/range dimensions of the diagnostic ultrasound imaging plane are indicated in the panel (a). The most hyperechoic pixels in the plane wave images, corresponding to reflections from the top and bottom of the clot, have been removed for better windowing and visualization of the histotripsy bubble cloud.

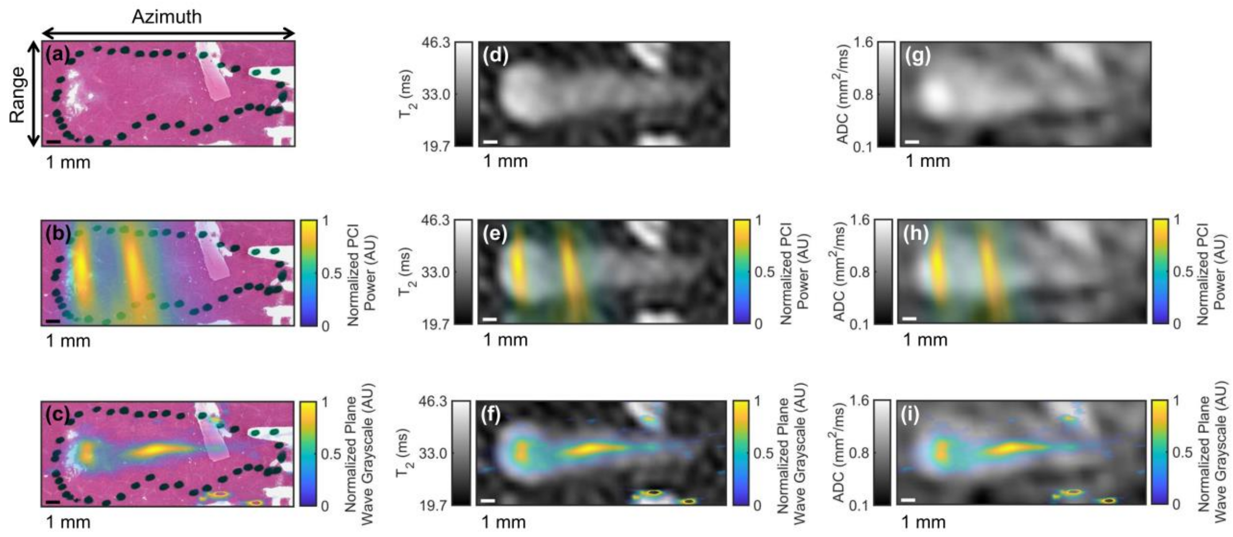

Figure 3.8. Registration of imaging with histologic observation of liver sample liquefaction. (a) Hematoxylin and eosin (H&E) stain of liver sample exposed to histotripsy with the ablation zone indicated by the dotted black outline, (b) coregistration of passive cavitation imaging (PCI) acoustic power and H&E-stained liver sample, (c) coregistration of plane wave grayscale and H&E-stained liver sample, (d) parametric T_2 map of treated liver sample, (e) coregistration of PCI acoustic power and T_2 map, (f) coregistration of plane wave grayscale and T_2 map, (g) parametric apparent diffusion coefficient (ADC) map of treated liver sample, (h) coregistration of PCI acoustic power and ADC map, and (i) coregistration of plane wave grayscale and ADC map. The histotripsy pulse (1-MHz fundamental frequency, 5-µs pulse duration, 25-MPa peak negative pressure) propagated from left to right in the image. The azimuth/range dimensions of the diagnostic ultrasound imaging plane are indicated in the panel (a). Reflections from connective tissue in (c), (f), and (i) have been removed for better windowing and visualization of the histotripsy bubble cloud.

3.3.3 Post hoc conventional B-mode imaging: RBC phantoms

Hypoechoic regions were observed in post-insonation conventional B-mode images of RBC phantoms, corresponding to the liquefaction zone (Figure 3.4, middle row). In 15 of 33 cases, a rim of hyperechoic signal was visible surrounding the hypoechoic region. The intensity of this rim tended to increase with distance from the histotripsy source and increase with peak negative pressure. Due to this rim feature and highly variable echogenicity, no significant differences in conventional B-mode grayscale were observed between liquefaction zones and background areas at any pressure level.

3.3.4 Post hoc conventional B-mode imaging: clot and liver samples

Post-insonation B-mode images of blood clots exhibited significantly reduced echogenicity compared with untreated clot, but no clear liquefaction outline or hyperechoic rim was apparent. Hypoechoic lesions were apparent following insonation of liver samples, although eight of 12 lesions also contained small hyperechoic structures throughout (Figure 3.9b). No significant difference in conventional B-mode grayscale between liquefaction zones and background was observed in liver samples.

3.3.5 Post hoc 3T MRI of RBC phantoms

Figure 3.10 depicts quantitative maps of T_1, T_2, and ADC from a typical RBC phantom. In all RBC phantoms, there was qualitative agreement in the features of T_1W or T_2W images and quantitative T_1 or T_2 maps. Changes in T_1 and absolute changes in T_2 relative to background were significantly greater than zero for all peak negative pressures. A significant increase in ADC from background was observed for 17- and 25-MPa insonations only. Values of T_1, T_2, and ADC measured within liquefaction zones did not change significantly between pressure levels.

Table 3.2 lists MR image parameter values measured within liquefaction zones for RBC phantoms and tissue samples.

3.3.6 Post hoc 3T MRI of clot and liver samples

Areas of liquefaction in liver samples were clearly demarcated in post hoc T_2W MR images (Figure 3.9c). Liquefaction zones of liver samples exhibited significant increases in T_2 and ADC of 7.2 ± 1.8 ms and 0.34 ± 0.10 mm^2/ms, respectively. No significant T_1 changes were observed in liver samples after histotripsy exposure. Histotripsy-induced clot liquefaction significantly increased T_1, T_2, and ADC by 302 ± 122 ms, 35 ± 8 ms, and 0.48 ± 0.11 mm^2/ms, respectively, compared with untreated clot areas.

Table 3.2: Diagnostic ultrasound and MR parameter values measured within liquefaction zones for RBC phantoms insonated at peak negative pressures of 13, 17, 21 and 25 MPa, liver samples insonated at 25 MPa, and clot samples insonated at 18 MPa.

Image Parameters	**RBC Phantoms**				**Liver Samples**	**Clot Samples**
	13 MPa	**17 MPa**	**21 MPa**	**25 MPa**	**25 MPa**	**18 MPa**
Bubble activity monitoring						
PCI Acoustic Power $(\times 10^5\ V^2)$	0.17 ± 0.06*	1.03 ± 0.26*	1.48 ± 0.21*	1.82 ± 0.15*	1.33 ± 0.41*	2.01 ± 0.46*
Plane Wave Grayscale $(\times 10^8)$	1.31 ± 0.54*	6.09 ± 2.26*	7.98 ± 2.27*	7.63 ± 3.08*	6.41 ± 2.26*	5.25 ± 1.06*
Post hoc evaluation						
Post hoc conventional B-mode Grayscale $(\times 10^8)$	0.43 ± 0.18	0.56 ± 0.47	0.42 ± 0.17	1.82 ± 3.77	34.9 ± 57.8	30.6 ± 15.9*
T_1 *(ms)*	2645 ± 83*	2673 ± 55*	2657 ± 56*	2647 ± 44*	296 ± 150	1240 ± 152*
T_2 *(ms)*	123 ± 4*	119 ± 4*	117 ± 6*	117 ± 7*	35.0 ± 2.7*	107 ± 20*
ADC (mm^2/ms)	1.97 ± 0.04	1.97 ± 0.04*	1.98 ± 0.05	1.98 ± 0.04*	0.89 ± 0.10*	1.13 ± 0.08*

* Liquefaction zone significantly different from background (untreated) phantom/tissue.
All errors are given as standard deviations.

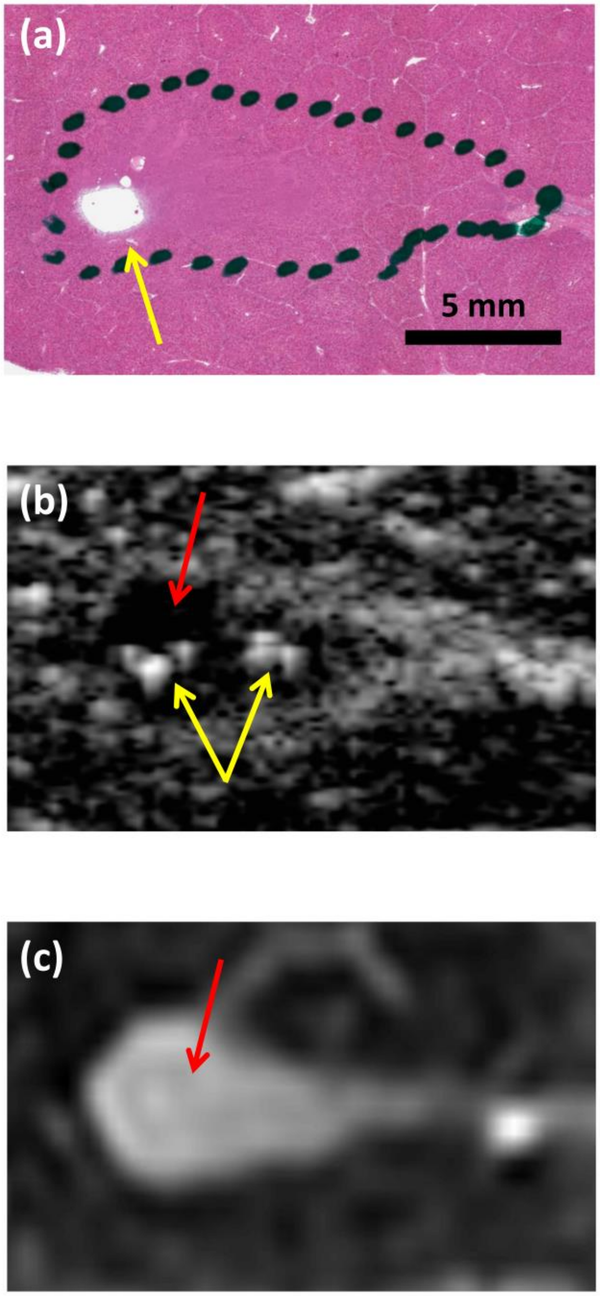

Figure 3.9. (a) Hematoxylin and eosin (H&E) stain, (b) post hoc conventional B-mode image, and (c) T_2-weighted image of liquefaction in the same liver sample. The liquefaction zone (dotted black dotted outline in (a), red arrows) can be distinguished as hypoechoic in (b) and hyperintense in (c). Regions of more thorough liquefaction exhibit minimal H&E staining, (yellow arrow in (a)). Small hyperechoic structures can be seen in the post hoc conventional B-mode image (yellow arrows in (b)), possibly indicating residual bubbles or accumulations of cellular debris. The histotripsy pulse (1-MHz fundamental frequency, 5-μs pulse duration, 25-MPa peak negative pressure) propagated from left to right in each image.

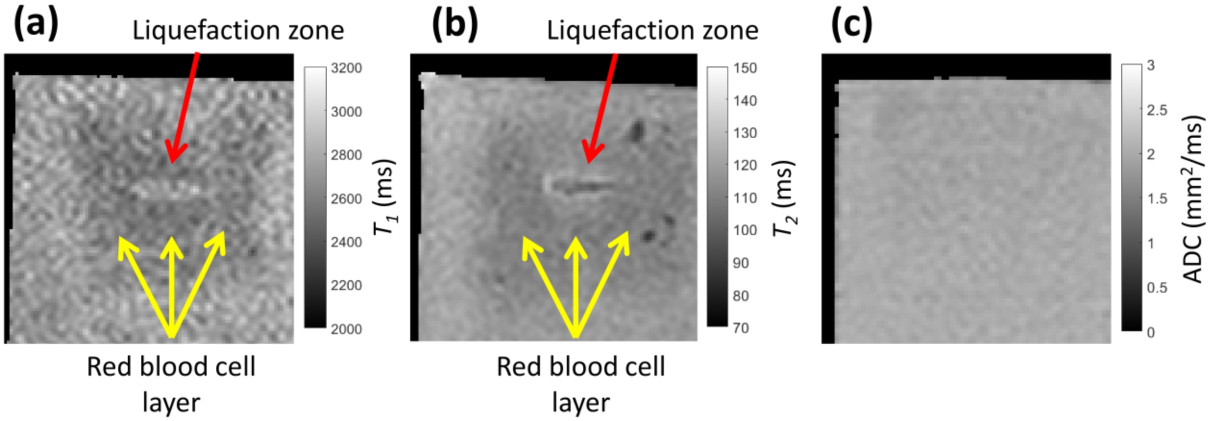

Figure 3.10. Examples of parametric (a) T_1, (b) T_2, and (c) apparent diffusion coefficient (ADC) maps for red blood cell phantoms. The liquefaction zone is indicated by a red arrow in (a) and (b). The red blood cell layer (dark area) is indicated by yellow arrows in (a) and (b). The histotripsy pulse (1-MHz fundamental frequency, 5-µs pulse duration, 17-MPa peak negative pressure) propagated from left to right in each image.

3.3.7 Image analysis/spatial correlation of red blood cell phantoms

Good qualitative agreement was observed between the visualized red blood cell liquefaction zone, observations of bubble activity via acoustic emissions and hyperechogenity, and visualized changes in the phantom structure (Figures 3.4 and 3.6). For peak negative pressures of 17 MPa or less, azimuthal locations of peak PCI power and peak plane wave grayscale were typically coincident with each other and proximal to the geometric focus of the histotripsy source (Figures 3.11a and 3.13). As peak negative pressure of the histotripsy pulse increased, a second peak in the plane wave grayscale was observed near the geometric focus of the therapy source (Figures 3.11b and 3.13). Parametric MR images of the liquefaction zone indicated that the areas of greatest change in the relaxation time T_2 corresponded to areas of relatively low PCI power and plane wave grayscale value (Figure 3.11a). At peak negative pressures greater than 13 MPa, liquefaction zones exhibited a spatially varying T_2 signature: T_2 increased maximally at the head of the liquefaction zone and tended to decrease below background level at the tail (Figures 3.11a and 3.13). T_1 and ADC did not exhibit a preferential location of greatest change within phantom liquefaction zones.

Bubble activity and ablation were elongated along the azimuthal dimension compared with the range dimension. Good correspondence between locations of liquefaction and imaging features were observed along the range dimension (Figure 3.12). However, the limited range resolution of the delay, sum, and integrate beamformer prevented meaningful analysis of the passive cavitation images along this dimension.[50]

3.3.8 Image analysis/spatial correlation of clot and liver samples

Areas of liquefaction within blood clots corresponded with regions of high PCI acoustic power, plane wave image grayscale, and T_2 (Figure 3.7). The strongest emissions of the bubble cloud were contained within the clot, although hyperechogenicity observed in plane wave images indicated extensions of the bubble cloud outside the clot. The maximal increases in T_2 coincided with clot/agarose interfaces, likely due to magnetic susceptibility effects (Figure 3.7d–f). T_1 and ADC were significantly increased within clot lesions relative to areas of untreated clot, but did not exhibit preferential locations of increase. The strongest acoustic emissions in clot samples were in the center of the liquefaction zone, with weaker emissions on either side of this location. Previous studies have demonstrated a threshold acoustic emission power required for liquefaction that may be considerably lower than the peak emissions observed.[47] It is therefore not surprising that liquefaction was observed throughout most of the azimuthal extent of the clot despite a large variation in acoustic emission power along this dimension (Figure 3.7).

Areas of liver qualified pathologically as necrotic (area within dotted outline in Figures 3.8a, 3.9a, 3.11b, and 3.12b) corresponded spatially to locations of elevated PCI power, plane wave grayscale, T_2, and ADC (Figures 3.8, 3.11b and 3.12b). The greatest sources of PCI emissions coincided with locations of greatest denucleation as indicated by histology (Figures 3.8a–c and 3.11b). A second local maximum in both the PCI power and plane wave grayscale distal to the peak emission location was present in 11 of 12 liver samples (Figure 3.11b). Peak plane wave grayscale values were located near the geometric focus, while T_2 and ADC maxima were typically proximal, also coinciding with the most thoroughly liquefied areas and regions of strong bubble cloud acoustic emissions (Figures 3.8d–i and 3.11b). Figure 3.12 depicts profiles of PCI power, plane wave grayscale, and change in T_2 along the range dimension of a liver sample.

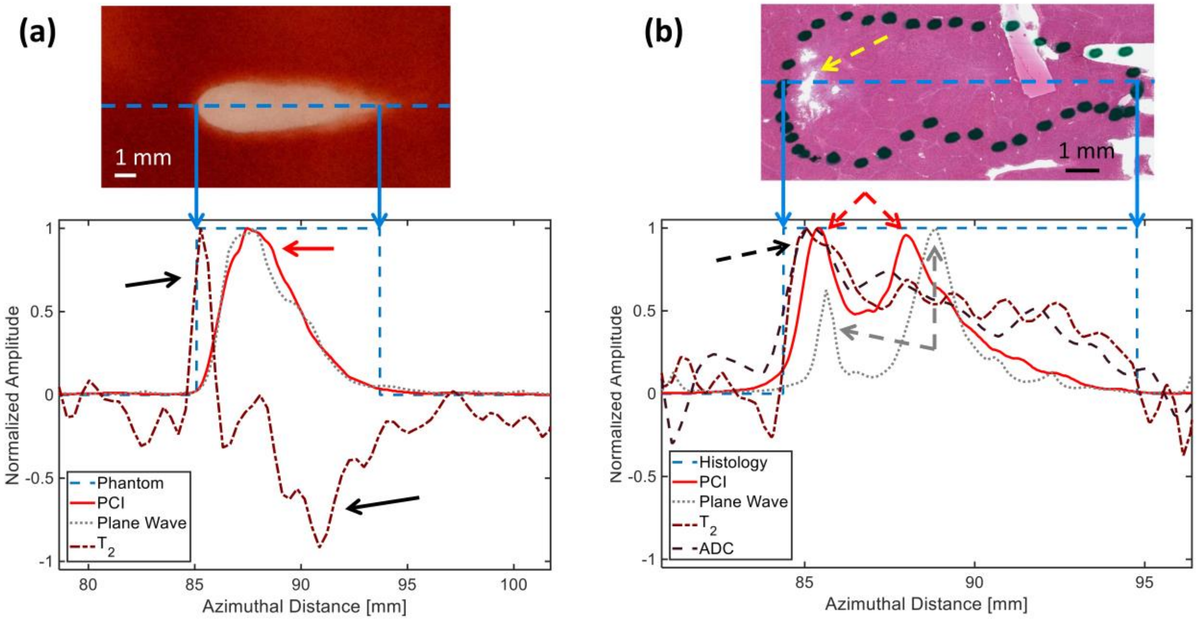

Figure 3.11. Normalized amplitudes of passive cavitation imaging (PCI) acoustic power, plane wave grayscale, and change in T_2 from background along the central axis of the liquefaction zone (dashed blue line in top images) for (a) a red blood cell (RBC) phantom, and (b) a liver sample. The locations of liquefaction are binarized for the bottom plots, with values of 1 indicating liquefaction and 0 indicating intact media. The areas of greatest change in T_2 in the RBC phantom (black arrows) correspond to areas of relatively low PCI power and plane wave grayscale intensity (red arrow) within the liquefaction zone. In the liver sample, locations of T_2 and apparent diffusion coefficient maxima (black dashed arrows) correspond with more thorough liquefaction as indicated by Hematoxylin and eosin staining (yellow dashed arrow). Two maxima are present for PCI power (red dashed arrows) and plane wave grayscale (gray dashed arrows). The proximal (leftmost) plane wave grayscale peak is small compared with the distal (rightmost) peak, while the larger proximal PCI peak more accurately reflects the increased liquefaction and magnetic resonance parameter changes in this location. The histotripsy pulse (1-MHz fundamental frequency, 5-μs pulse duration, 17-MPa peak negative pressure for RBC phantom, 25-MPa peak negative pressure for liver sample) propagated from left to right in each image.

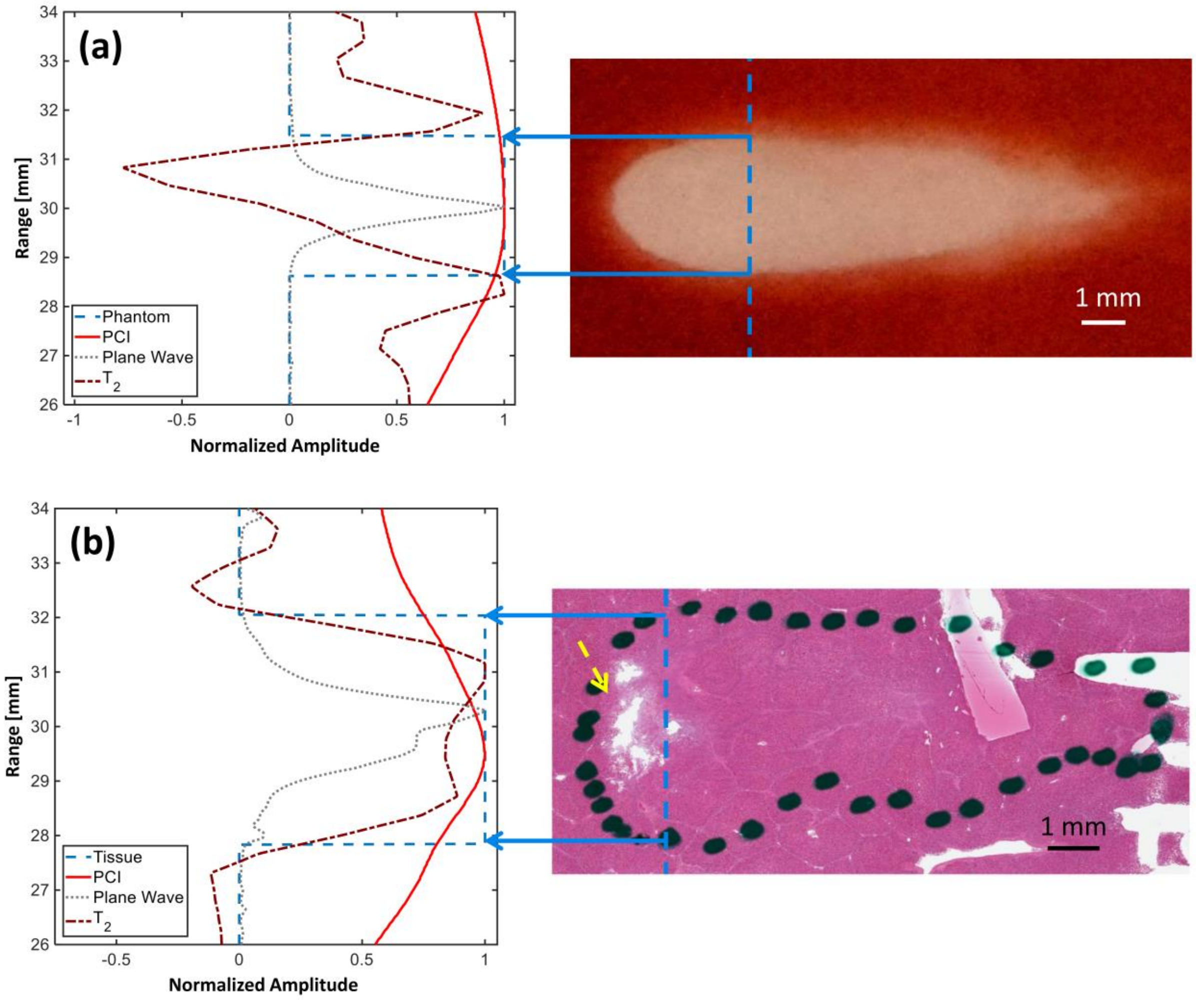

Figure 3.12. Normalized amplitudes of passive cavitation imaging (PCI) acoustic power, plane wave grayscale, and change in T_2 from background at the azimuth position of maximum PCI power (vertical dashed blue lines in right-side images) for (a) a red blood cell phantom, and (b) a liver sample. Apparent diffusion coefficient signals in red blood cell phantoms and T_1 and plane wave grayscale signals in all samples were dominated by noise and thus excluded from this figure. The locations of liquefaction are binarized for the plots, with values of 1 indicating liquefaction and 0 indicating intact media. The azimuthal location of maximum PCI power in the liver sample corresponds with more thorough liquefaction as indicated by hematoxylin and eosin staining (yellow dashed arrow). The histotripsy pulse (1-MHz fundamental frequency, 5-μs pulse duration, 17-MPa peak negative pressure for RBC phantom, 25-MPa peak negative pressure for liver sample) propagated from left to right in each image.

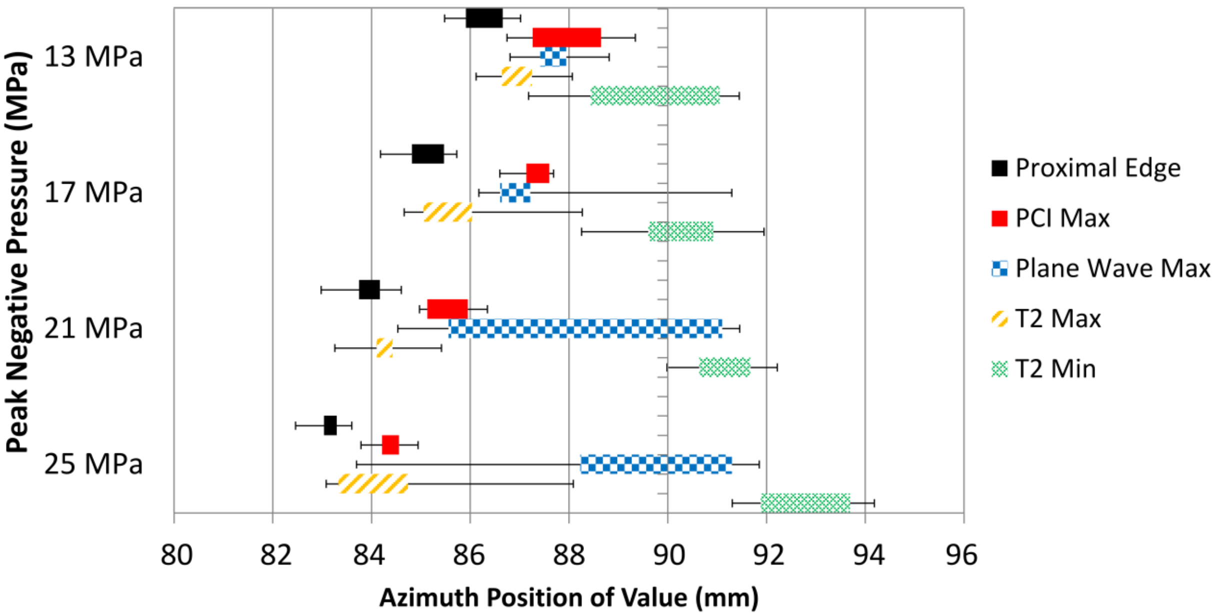

Figure 3.13. Azimuthal position of proximal edge of liquefaction zone (solid black bars), maximum passive cavitation imaging (PCI) acoustic power (solid red bars), plane wave grayscale (checkered blue bars), and maximum (striped orange bars) and minimum (cross-hatched green bars) T_2 for all pressures applied to red blood cell phantoms. Colored bars cover 25% to 75% quantiles, and error bars extend to maximum and minimum azimuthal positions recorded for each parameter. 90 mm corresponds to the geometric focus of the histotripsy source. Locations of maximum PCI acoustic power and T_2 shift proximally with increasing pressure, while plane wave maxima and T_2 minima shift distally.

3.3.9 Receiver Operating Characteristic (ROC) Analyses

The ROC curves obtained from comparing quantitative imaging features to histotripsy-induced liquefaction are shown in Figure 3.14. The AUC values, thresholds for phantom liquefaction/liver necrosis, and the sensitivity, specificity, and accuracy at these threshold values are reported in Tables 3.3 and 3.4. For liver samples and RBC phantoms, confidence intervals of ROC curves indicated that all diagnostic ultrasound and MR image parameters resulted in AUCs significantly greater than 0.5, indicating improved performance over guessing.

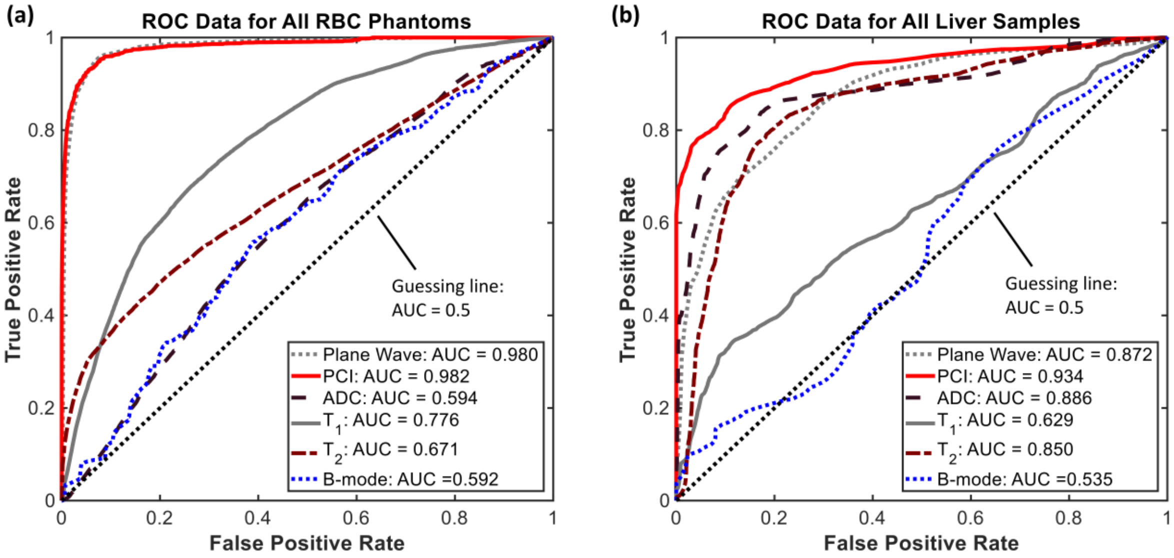

Figure 3.14. Receiver Operating Characteristic (ROC) curves obtained from (a) red blood cell phantoms and (b) liver samples. Quantitative plane wave grayscale (gray dotted line), passive cavitation imaging acoustic power (red solid line), apparent diffusion coefficient (black dashed line), T_1, (gray solid line), T_2, (brown dash-dot line), and post hoc conventional B-mode grayscale (blue dotted line) were used to predict presence of liquefaction/necrosis along azimuth dimension of histotripsy lesions across all peak negative pressures of the histotripsy pulse (only 1 pressure level was employed in the liver studies). The black dotted line indicates the resulting ROC curve from random guessing (area under the curve = 0.5).

3.3.10 ROC Analysis: RBC phantoms

For all image parameters, no trend in RBC phantom AUC was apparent with increasing pressure level. Assessment of bubble activity via plane wave imaging or PCI performed significantly better than post hoc assessment of the liquefaction zone with MR or conventional B-mode imaging. T_1 performed significantly better than T_2, which performed significantly better than ADC and post hoc conventional B-mode grayscale. At the optimal discrimination thresholds, specificity was greater than 0.84 for all image parameters. T_1 was more sensitive to liquefaction than T_2, whereas T_2 was more specific to liquefaction. Due to the low discriminatory power of ADC, its threshold resulted in 100% negative classifications and an undefined positive predictive value. Similarly, post hoc conventional B-mode exhibited low discriminatory power and a threshold strongly favoring negative classification. Excluding ADC, sensitivity was lowest for post hoc conventional B-mode compared with all other diagnostic ultrasound and MR imaging parameters.

Table 3.3: Area under the Curve (AUC) values calculated for all RBC phantom data, and sensitivities, specificities, accuracies, positive predictive values (PPV), and negative predictive values (NPV) at optimal threshold points for all ROC curves.

Image Parameter	**Optimal Threshold Value [95% confidence interval]**	**AUC**	**Sensitivity**	**Specificity**	**Accuracy**	**PPV**	**NPV**
PCI Acoustic Power $(\times 10^4\ V^2)$	1.17 [1.17, 1.19]	0.982	**0.896**	0.969	0.947	0.926	0.955
Plane Wave Grayscale $(\times 10^8)$	1.03 [0.80, 1.09]	**0.980**	**0.884**	**0.967**	**0.942**	**0.921**	**0.950**
T_1 *(change in ms)*	65 [56, 66]	**0.776**	**0.495**	0.865	0.753	0.616	**0.797**
T_2 *(absolute change in ms)*	7.24 [7.16, 7.62] (absolute change in ms)	**0.671**	**0.299**	0.949^	**0.751**	0.718^	**0.756**
ADC† *(change in* mm^2/ms*)*	0.195 [0.192, 0.195]	0.594	0.000	**1.000**^	0.696	N/A	0.696
Post hoc conventional B-mode $(\times 10^9$ *absolute change in grayscale)*	5.09 [5.09, 5.09]	0.592	0.034^	0.992	0.701	0.659	0.702

Image parameters are listed in order of greatest to lowest AUC values.

Bold text indicates statistic is significantly greater than that of subsequent (next lowest) parameter in left column.

^ indicates statistic significantly greater than that of preceding (next highest) parameter in left column.

† Chosen threshold point resulted in 100% negative classifications.

3.3.11 ROC Analysis: Liver samples

All image parameters from liver samples resulted in significantly different AUC values. PCI power performed best, followed by ADC, plane wave grayscale, T_2, T_1, and post hoc conventional B-mode grayscale. At the optimal discrimination thresholds, PCI power and plane wave grayscale were more sensitive to liquefaction than any MR image parameter, although all three MR parameters were significantly more specific to liquefaction than plane wave grayscale. Compared with plane wave grayscale, ADC and T_2 also had significantly improved PPV, and ADC had significantly improved accuracy. Post hoc conventional B-mode grayscale had the lowest AUC value, but was more sensitive to liquefaction than T_1.

Table 3.4: Area under the Curve (AUC) values calculated for all liver sample data, and sensitivities, specificities, accuracies, positive predictive values (PPV), and negative predictive values (NPV) at optimal threshold points for all ROC curves.

Image Parameter	**Optimal Threshold Value [95% confidence interval]**	**AUC**	**Sensitivity**	**Specificity**	**Accuracy**	**PPV**	**NPV**
PCI Power (×10^3 V^2)	7.055 [7.046, 7.435]	**0.934**	**0.862**	**0.882**	**0.871**	**0.885**	0.858
ADC (change in mm^2/ms)	0.13 [0.11, 0.22]	**0.886**	0.839	**0.828**	**0.833**	**0.837**	0.830
Plane Wave Grayscale (×10^8)	0.65 [0.60, 1.27]	**0.872**	**0.853**	0.708	0.783	0.755	0.821
T_2 (change in ms)	3.5 [3.1, 4.1]	**0.850**	**0.810**	0.799^	**0.804**	**0.809**^	**0.800**
T_1 (change in ms)	41 [40, 45]	**0.629**	0.342	**0.886**^	**0.621**	**0.741**	0.586
Post hoc conventional B-mode (×10^8 absolute change in grayscale)	7.08 [6.61, 7.57]	0.535	0.759^	0.345	0.558	0.550	0.577

Image parameters are listed in order of greatest to lowest AUC values.

Bold text indicates statistic is significantly greater than that of subsequent (next lowest) parameter in left column.

^ indicates statistic significantly greater than that of preceding (next highest) parameter in left column.

3.3.12 Dice Similarity Coefficient Analysis

Dice Similarity Coefficient (DSC) values derived from post hoc conventional B-mode images and T_2W images are given in Table 3.5. In RBC phantoms, with the exception of 17 MPa peak negative pressure pulses, DSC values were significantly greater for T_2W images than post hoc conventional B-mode images. For peak negative pressures of 17-, 21-, and 25-MPa, DSC values were significantly higher than 13-MPa insonations for both post hoc conventional B-mode and T_2W images. In liver samples, DSC values derived from T_2W image outlines were significantly greater than those derived from conventional B-mode image outlines.

Table 3.5: DSC values ± standard deviations as a function of peak negative pressure and tissue/phantom type.

	Red Blood Cell Phantoms					**Liver Samples**
	13 MPa	*17 MPa*	*21 MPa*	*25 MPa*	*All Pressures*	*25 MPa*
Conventional B-mode images	0.68 ± 0.11	0.81 ± 0.11	0.83 ± 0.05	0.85 ± 0.08	0.79 ± 0.11	0.49 ± 0.15
T_2W images	0.77 ± 0.10*	0.87 ± 0.06	0.91 ± 0.02*	0.91 ± 0.02*	0.87 ± 0.08*	0.77 ± 0.06*

* indicates significantly greater DSC value from T_2W images over post hoc conventional B-mode images.
Errors represent standard deviations over samples.

3.4 Discussion

3.4.1 Observations of phantom/tissue liquefaction

Liquefaction was achieved in all phantom and tissue samples for all pressures utilized in this study. In RBC phantoms, the lesion morphology and area were dependent on the peak negative pressure of the histotripsy pulse. Liquefaction within the head of the treatment zone appeared continuous. Discontinuous regions of liquefaction at the tail of the focal zone were occasionally present near the periphery (Figure 3.15). Insonation of blood clots induced liquefaction of most of the clot area and some of the surrounding agarose. The focal size of the histotripsy source used in this study (10 mm -6 dB length) was larger than the clot diameter (4 mm), which has been shown to cause collateral vascular damage in thrombotripsy procedures.[197] Histologic examination of clot samples revealed thin protrusions of preferential cavitation in areas of liquefied agarose, similar to the discontinuous regions observed in RBC phantom insonations. Areas of residual nucleated cells were also found in liver necrosis zones, alongside sites of apparent preferential cavitation. These observations are consistent with descriptions of cavitation memory effects, in which the application of histotripsy pulses at pulse repetition frequencies greater than 1–10 Hz increases the spatial persistence of bubble clouds.[198–200] Bubble cloud persistence generates mechanical activity at finite spatial locations within the focal zone and may result in inhomogeneous liquefaction. Applying histotripsy pulses at a lower repetition frequency or applying bubble-deleting pulses[151] between therapeutic pulses would improve liquefaction zone uniformity. Residual regions within liquefaction zones may also be reflective of stiff tissue structures resistant to the lethal strain induced by the bubble cloud activity.[55]

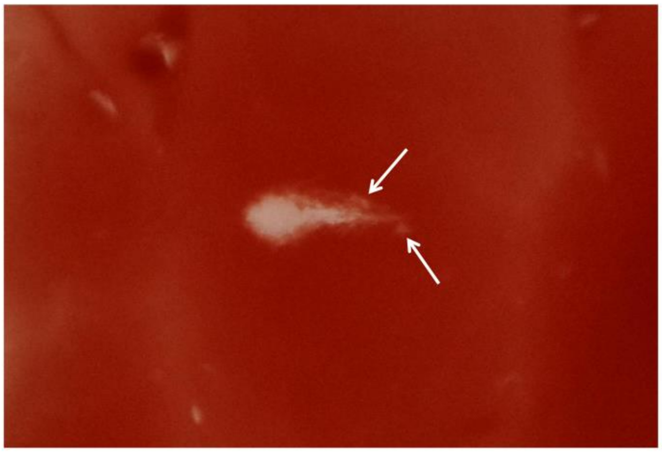

Figure 3.15. Gross digital photograph of liquefaction zone in a red blood cell phantom. The histotripsy pulse (1-MHz fundamental frequency, 5-μs pulse duration, 13-MPa peak negative pressure) propagated from left to right in the image. Discontinuous liquefaction regions along the periphery of the focal zone (white arrows) may indicate sites of persistent bubble clouds.

3.4.2 Prediction of liquefaction via bubble activity

One primary consideration for all image-guided therapies is to establish a quantitative, image-based dose metric with which to control the application of therapy. PCI provides a quantitative measure of the strength of histotripsy bubble cloud activity,[50] as evidenced by the increase in PCI power with each pressure step. Plane wave grayscale values within lesions, which indicate presence of bubble clouds but not the strength of their mechanical action,[47] did not increase for insonations above 17 MPa. This result agrees with previously recorded pressure thresholds for shock-scattering histotripsy in agarose phantoms.[46, 201] The PCI acoustic power within regions of clot liquefaction were two-fold greater than those measured in the closest corresponding pressure for RBC phantom insonation (17 MPa vs. 18 MPa). This may reflect the higher dissolved oxygen content in the clots compared with the degassed agarose mixture prolonging dissolution of microbubbles formed by the histotripsy pulses and promoting repeat cavitation events.[202] In contrast, PCI powers measured from liver insonations were approximately 27% lower than those measured from corresponding (25-MPa) RBC phantom insonations, likely due to greater attenuation of cavitation emissions in the liver tissue.[189] Plane wave grayscale values were comparable between clots, livers and RBC phantoms at corresponding pressure levels, consistent with the saturation of plane wave grayscale observed in RBC phantoms for pressures above 17 MPa.

A key result of this study is that observations of bubble activity were better indicators of liquefaction than post hoc assessment via conventional B-mode or MR imaging (Figure 3.14). Prediction of RBC phantom liquefaction was similar for PCI and plane wave grayscale, whereas PCI provided an improved prediction of liver sample liquefaction compared with plane wave imaging. The liver samples have an increased acoustic attenuation compared with the agarose phantoms, which may account for the discrepancy in liquefaction prediction between PCI and plane wave imaging. In a similar study, PCI provided an improved prediction of histotripsy liquefaction compared with plane wave imaging in an attenuating prostate tissue phantom[47]. The significantly reduced specificity of plane wave imaging in the liver samples of this study also suggests a greater incidence of false positives from highly reflective structures in the tissue. There may be other reasons for the similar predictive power of PCI and plane wave imaging observed in RBC phantoms. The study presented here utilized a pulse repetition frequency five times larger than the prostate phantom study (100 vs. 20 Hz), which may have increased bubble cloud persistence spatially and improved the correlation between plane wave grayscale and phantom liquefaction. The total number of pulses applied in this study was also increased by a factor of 2 (4000 vs. 2000), which would reduce noise in the averaged data.

3.4.3 Post hoc evaluation of liquefaction with MR and conventional B-mode imaging

Accurate assessment of the liquefaction zone extent is necessary to confirm histotripsy treatment efficacy. Insonation of clot and liver tissue samples in this study resulted in more pronounced changes in T_1, T_2, and diffusion compared with RBC phantoms. Uniform increases in T_2 and ADC and both uniform increases and decreases in T_1 have been observed previously following boiling histotripsy ablation in *ex vivo* tissue.[56, 203] Allen *et al* (2017) reported uniform increases in T_1, T_2 and ADC in similar 16% RBC phantoms and *ex vivo* tissue samples following histotripsy liquefaction, but utilized 2-cycle pulses from a 400-kHz transducer with a 10 Hz PRF. In contrast, this study utilized shock-scattering histotripsy pulses of 5-cycle duration from a 1-MHz source at a PRF of 100 Hz. Allen *et al* (2017) acquired MR images of histotripsy ablation, where the focus of the source was rastered throughout a volume. Here, in contrast, histotripsy pulses were applied to a single fixed location. The MR image slices in this study were oriented parallel to the direction of ultrasound propagation to observe variations in the liquefaction zone along this axial dimension. Allen *et al* (2017) oriented MR image slices perpendicular to the direction of ultrasound propagation, which would likely homogenize the appearance of the ablation zone.

In this study, MR image slices of RBC phantoms encompassed both pure agarose and thin RBC layers. Therefore, only a portion of MR signal originated from the RBC layers, degrading the contrast between liquefied and intact structures. Following histotripsy, homogenization of paramagnetic blood agents is the primary source of change in T_2, while disruption of diffusion-limiting membranes tends to increase apparent diffusion.[52] The greater density of red blood cells and cell/nuclear membranes in tissue samples likely made liquefaction more evident. Indeed, much stronger changes in T_1, T_2, and ADC following histotripsy liquefaction were observed in human whole blood clots in comparison to the red blood cell phantoms (Figure 3.7, Table 3.2). Histological lesion boundaries in liver samples were based on denucleation and homogenization of cellular structures, rather than red blood cell lysis, which may explain the improved discriminatory power of ADC over T_2 observed in liver samples.

Reduction in B-mode image backscatter is the primary method for evaluating the efficacy of histotripsy therapy in pre-clinical studies[181] and was employed in a clinical trial assessing histotripsy ablation of the prostate.[176] Hypoechoic regions in B-mode images have been shown to correlate with histologic areas of liquefaction.[44, 180] In this study, the information provided by conventional B-mode imaging was limited due to low contrast-to-noise ratios between intact and liquefied tissue, image artifacts, and hyperechoic structures within and surrounding liquefaction zones (Figures 3.4 and 3.9b). Post hoc conventional B-mode imaging produced the lowest AUC of any image parameter studied and exhibited worse correlation with liquefaction and lesion morphology than T_2W images for both RBC phantoms and liver samples. While T_2 maps of liquefied RBC layers exhibited spatially varying features (Figure 3.6d–f), liquefaction zones were easily identified in clot and liver samples by a marked increase in intensity (Figures 3.7d–f and 3.8d–f). Previous studies have demonstrated strong agreement of morphology between T_2W imaging and gross histologic observation of histotripsy lesions, suggesting this image modality is well-suited to evaluation of histotripsy ablation.[53, 55] The liquefaction zone for RBC phantoms tended to be underestimated by conventional B-mode imaging (26 of 33 insonations) but overestimated by T_2W MR imaging (18 of 33 insonations). Both imaging modalities underestimated histologic lesion areas for liver samples, but T_2W image outlines more closely approximated necrosis boundaries. Post hoc evaluative imaging, particularly MRI, may be a necessary supplement to bubble-monitoring techniques for histotripsy guidance.

3.4.4 Relationship between diagnostic ultrasound, MRI, and liquefaction

Diagnostic ultrasound and MR imaging can provide complimentary data to inform histotripsy guidance. The short timescale of bubble cloud activity is best captured with the real-time capability of diagnostic ultrasound imaging, while MR image contrast can supply clearer delineations of the liquefaction zone post-insonation. In this study, the information provided by each image modality varied between tissue and RBC phantom samples, most notably as the predictive power of MR imaging improved considerably in liver samples. The intersection of ROC curves for plane wave grayscale, T_2, and ADC measured from liver samples in this study (Figure 3.14b) suggest that constructing a liquefaction classifier based on input from more than one of these image modalities (e.g. logistic regression)[204] would improve classification of liquefied and intact tissue. Such a multi-modal approach to histotripsy image guidance could improve accuracy of treatment zone measurements and improve treatment outcomes. Although PCI produced greater AUC values than any other image metric, its limited range resolution necessitates the use of supplementary image data (e.g. plane wave, conventional B-mode, or MRI) to predict two- and three-dimensional liquefaction zones. In the RBC phantoms, fewer of the analyzed pixels were associated with liquefaction compared with intact structure (30% liquefied and 70% intact). As a result, the liquefaction threshold pixel value for weaker discriminators of liquefaction (e.g. conventional B-mode grayscale, T_2, and ADC) favored specificity over sensitivity (Table 3.3). These modalities would therefore not provide good sensitivity to the onset of tissue liquefaction. The use of absolute changes in T_2 and post hoc conventional B-mode grayscale from background also likely reduced the power of these features in distinguishing liquefaction in this study, as both positive and negative fluctuations in noise masked the liquefaction-induced changes.

In all materials studied, the azimuthal locations of maximum changes in diagnostic ultrasound and MR image parameters appeared to reflect the evolution of the bubble cloud and resulting liquefaction. In RBC phantoms, the location of strongest bubble cloud activity as indicated by PCI was consistently at the proximal, wider end of the lesion. The observation of two plane wave grayscale peaks in this study was also reported by Bader *et al* (2018a) during histotripsy insonation of prostate-mimicking phantoms. This phenomenon likely reflects nuclei expansion at the focal zone as well as strong bubble activity induced by shock scattering of incident waves proximal to the source.[46] For peak negative pressures of 25 MPa, the intensity of the distal plane wave peak surpassed that of the proximal peak and was accompanied by the appearance of a second PCI peak (Figure 3.11b). The distal peak at the geometric focus of the therapy source likely indicates onset of intrinsic threshold cavitation[175, 187, 205] in addition to proximal shock-scattering cavitation. In RBC phantoms, the observed maxima and minima in T_2 became increasingly separated with increasing pressure (Figure 3.13). Decreases in T_2 at the tail ends of RBC phantom liquefaction zones may indicate distal accumulation of agarose debris and paramagnetic blood agents due to streaming, which was also suggested by hyperechoic tails in the post hoc conventional B-mode images. These features were more pronounced at greater peak negative pressures and may be due to intense streaming from the bubble cloud that causes accumulation of debris at certain locations within the liquefaction zone over time. The onset of such streaming may indicate the area was liquefied over the course of many applied pulses, suggesting overtreatment. The maximum observed increases in T_2 at the proximal edge and around the liquefaction boundary are likely due to the magnetic susceptibility difference between the intact and liquefied agar matrix. In liver samples, a spatial variation in T_2 and ADC was also present in 3 of 12 lesions (Figure 3.8d–i). Maxima for both of these parameters were frequently located at the proximal end of liver necrosis zones. Furthermore, histological liver slides indicated liquefaction was most thorough at the proximal ends of the lesions, which also exhibited peaks in PCI and plane wave grayscale intensity. These findings collectively indicate that both diagnostic ultrasound and MR image features could potentially quantify the efficacy of histotripsy liquefaction, which may vary along the axial dimension for certain insonation parameters. Furthermore, combining PCI and plane wave image data can indicate which histotripsy modes (e.g. shock-scattering vs. intrinsic threshold) are occurring.

3.4.5 Limitations of study

There are some aspects of this study that limit the generalizability of the findings. The ROC and DSC analyses of liver samples in this study were limited due to some distortion of the tissue and lesion morphology during histological processing. The ROC analysis was based on a binary model of treatment outcome (i.e. intact or liquefied), which may oversimplify the liquefaction process. Future studies should explore the type of cell death or *in vivo* immunological response relative to imaging features. The histotripsy insonation parameters could also be varied to determine sensitivity of the image parameters explored here to varying degrees of histotripsy liquefaction. The objective of this study was to determine the accuracy of diagnostic ultrasound and MR image quantities in predicting spatial locations of histotripsy liquefaction. Therefore, the histotripsy insonation parameters were chosen such that liquefaction occurred somewhere within the imaging plane, but not everywhere throughout the entire imaging plane. Including samples without any observable liquefaction may produce a more robust analysis.

The findings of this study constitute a post hoc analysis of histotripsy liquefaction, and were not tested as a real-time prediction of liquefaction. The optimal operating points extracted from the ROC curves provide quantitative pixel values associated with liquefaction, but may vary based on the tissue type, array sensitivity, or the therapy insonation conditions. Conclusions of the ROC analysis were restricted to the azimuthal dimension due to the limited range resolution of PCI. Histotripsy bubble activity is strongest along the central axis of the therapy source (azimuthal dimension for this study, Figure 3.2).[46] Alternative beamforming algorithms can be implemented to reduce the range artifact, but have an increased computational load for image generation.[206, 207] Alternatively, sparse, multi-element detectors can be constructed with favorable point spread functions to minimize the artifact.[208]

In this study, passive cavitation and plane wave images were analyzed based on a pixel-by-pixel summation of all frames acquired for a given data set (400 frames per data set for RBC phantoms, 800 frames per data set for liver samples). The temporal averaging of the images used here neglects changes in the bubble activity as the medium liquefies.[164, 209, 210] The use of MR parameter changes to evaluate liquefaction as presented here also constitutes only a post hoc assessment, rather than real-time monitoring of treatment. Other studies have assessed MR cavitation contrast for monitoring the mechanical action of histotripsy[211, 212] and MR thermometry for monitoring tissue boiling at pre-clinical field strengths (4.7–9T).[213] In this study, MR images were acquired with a 3T clinical scanner.

The phantoms and tissue samples evaluated in this study may not be representative of histotripsy liquefaction *in vivo*. The liquefaction zone was visualized in this study at a fixed time point shortly following the histotripsy exposure, which does not capture changes in the lesion morphology over the course of the applied pulses. Physiologic responses due to the therapeutic insonation may obfuscate the ablation extent in post hoc evaluative imaging immediately following treatment.[68, 124] In particular, the use of T_2W imaging to designate histotripsy ablation may be complicated *in vivo* by the presence of hemorrhage and lesion evolution.[125] The appearance of post hoc images following histotripsy may therefore be highly dependent on the timing of their acquisition, underscoring the importance of real-time monitoring of bubble cloud activity via PCI for successful histotripsy guidance. However, the utility of MR imaging in detecting liquefaction-induced tissue changes and delineating histotripsy lesions has been demonstrated both in prior studies[52–56] and the ROC and DSC analysis of this study. This suggests a multi-modal image guidance scheme including PCI and plane wave imaging for monitoring cavitation and MR imaging for lesion assessment may be well-suited to histotripsy ablation and facilitate its clinical translation. Advancing analysis techniques such as machine learning that delineate the extent of damage in post hoc imaging may also aid in the assessment of histotripsy treatment progress.[214]

3.5 Conclusions and future work

This *in vitro* and *ex* vivo study examined the relative utility of diagnostic ultrasound and MR imaging for predicting histotripsy-induced liquefaction. In red blood cell phantoms, quantitative measurements of ultrasound passive cavitation imaging (PCI) power, ultrasound plane wave grayscale, and magnetic resonance (MR) imaging T_1 and T_2 relaxation times were indicative of histotripsy induced cavitation activity and resultant liquefaction. Changes in MR imaging parameters post-histotripsy were most apparent in clot and liver tissue samples. Post hoc conventional B-mode imaging proved to be an unreliable indicator of liquefaction compared with other diagnostic ultrasound and MR imaging parameters. PCI power produced the largest area under the curve for all materials studied, but the performances of PCI, plane wave, and MR modalities were more comparable in liver samples. Delineation of lesions from T_2-weighted images more accurately reflected phantom and tissue liquefaction than post hoc conventional B-mode images. Further study in a greater variety of *in vivo* tissues is needed to determine the relative utility of diagnostic ultrasound and MR image guidance for histotripsy in physiologic conditions. A more thorough evaluation of histopathologic observations following liquefaction is also important to relate the information provided by imaging to relevant biological outcomes. Nonetheless, the use of multiple imaging modalities provides complimentary information and improves the assessment of histotripsy liquefaction compared with current clinically used approaches.

CHAPTER 4

ASSESSMENT OF HISTOTRIPSY-MEDIATED PRODUCTION OF REACTIVE OXYGEN SPECIES IN VITRO

4.1 Introduction

Standard treatments for aggressive cancerous diseases are often associated with harmful side effects, high failure rates, and are not well-tolerated by critically ill patients.[215] Recurrent disease is often prone to radio-, chemo-, and hormone therapy resistance,[12, 216–219] as well as metastatic spread. Further, the target lesions are often inaccessible by surgical resection.[16, 220] These limitations motivate the development of therapies that induce cancer cell death with alternative mechanisms in order to bypass the unique biological resilience of recurrent cancerous disease.

One possible alternative treatment is the creation of ultrasound-induced reactive oxygen species (ROS) in tissue.[221] Pyrolysis of water vapor within the adiabatically collapsing bubbles can form hydroxyl (•OH) radicals,[222] as well as catalyzing the formation of other ROS.[223] Sonodynamic therapy (SDT) agents can amplify the cytotoxic ROS generated by inertial cavitation activity.[57] The primary mechanism for activation of SDT agents is sonoluminescence, or bubble-induced light emission.[224, 225] In multibubble sonoluminescence (MBSL), light emission occurs via thermal Bremsstrahlung radiation, ion recombination, and spectral emissions from electronic transitions within the warm, dense plasma (> 5000 K).[226] The emission spectra of sonoluminescent bubbles consist primarily of wavelengths between 200 and 800 nm due to decreasing radiance above 800 nm and strong absorption by water below 200 nm.[227] Semiconductor materials such as titanium dioxide (TiO_2) are commonly employed as sonosensitizers.[225] Upon exposure to ultraviolet light, electron/hole pairs occur within the crystalline structure due to excited valence-band electrons that become trapped along the crystal surface. Reduction and oxidation activities of the electrons/holes result in ROS in the surrounding solution.[228]

Most implementations of SDT utilize microbubbles as nucleation agents for inertial cavitation, with parallel or conjugated administration of sonosensitizing agents. Functionalized targeting of the microbubble enables greater accumulation and ROS generation in the target tissues and reduces the tensile pressure required to initiate cavitation. Oxygen-loaded microbubbles have also been used to improve efficacy of SDT in hypoxic tumor environments.[229] Microbubbles are vascular agents, which prevents significant bubble activity beyond the vessel and limits their uptake in poorly vascularized tumor regions. The intravascular nature of contrast agents motivates the development of methods to improve initiation of cavitation throughout the tumor. Sonodynamic therapy has been applied to a variety of cancerous pathologies, including prostate cancer,[230] but remains limited by low sensitizer accumulation in the target and a lack of consistent ultrasound conditions or quantitative guidance of the therapy.[57]

Histotripsy is a non-thermal ultrasound therapy that generates copious amounts of inertial cavitation without the need of exogenous agents.[40, 41] Preclinical studies have demonstrated the capability of histotripsy for the disintegration of liver, kidney, breast, and prostate tissue, as well as vascular thrombi with high efficacy and specificity.[44] Further, the safety of histotripsy technology in prostate tissue ablation has already been established in a pilot human trial.[176] Mechanical activity via bubble expansion and inertial cavitation are the primary mechanisms for tissue ablation, which can be initiated irrespective of the biological or biochemical resistances of the target tissue. Histotripsy bubble activity has been employed to enhance the delivery of lytic and chemotherapeutic drugs.[186, 231] Ultrasound-induced bubble activity is also capable of generating reactive oxygen species without sonosensitizing agents.[112] We hypothesize that histotripsy has the capacity to activate sonosensitizers while simultaneously liquefying tissue structure. Because the location of bubble activation is not restricted to the vasculature, robust ROS can be generated throughout the target tissue. Hydrophobic regions on the surfaces of sonosensitizing particles like TiO_2 may serve as bubble nucleation sites, reducing the peak negative pressure required for ROS generation and minimize off-target effects.

In this study, ROS generation via histotripsy exposure of titanium dioxide (TiO_2) was explored. A terephthalic acid assay was used to quantify •OH formation. The power of bubble activity generated by the histotripsy pulse was mapped spatially with passive cavitation imaging[50, 232] and correlated with the degree of ROS generation.

4.2 Materials & Methods

4.2.1 Chemical solutions

An established protocol was used to quantify histotripsy-induced ROS generation.[112] Stock solutions of terephthalic acid (TA) and 2-hydroxyterephthalic acid (HTA) were prepared following Mason et al.[233] Briefly, a 20 mM TA solution was generated by mixing 3.32 g of TA (ACROS Organics, Thermo Fisher Scientific, Waltham, MA, USA) and 1.00 g of NaOH (Fisher Scientific, Hampton, NH, USA) in 1 L of 1X phosphate buffered saline (PBS) (Mediatech, Inc., Manassas, VA) until completely dissolved. The TA stock solution was diluted to 2 mMol for exposure to histotripsy pulses. A 2 mM stock solution of HTA was then prepared by mixing 0.182 g of HTA and 0.1 g of NaOH (TCI America, Portland, OR) in 1X PBS until completely dissolved. A reference standard solution of 1-μM HTA sample was used to standardize and quantify ROS generation in the fluorescence assay (see Section 4.2.4). The pH of both stock solutions was 7.3 and was checked prior to each use.

4.2.2 Experimental setup and ultrasound exposure

Titanium dioxide (TiO_2) nanoparticles (anatase, Alfa Aesar, Haverhill, MA, USA; 32 nm mean diameter, 45 m^2/g surface area) were tested as a sonosensitizing agent to amplify histotripsy-induced ROS production. Stock solutions containing 1.75 mg/mL TiO_2[225] in gas-saturated 1X PBS were prepared. 20 mM TA solution and gas-saturated PBS were added to the stock TiO_2 solution in the ratio 1:7:2 (20 mM TA : gas-saturated PBS : TiO_2 solution) to generate a 2 mM TA solution with 0.35 mg/mL TiO_2 for sonication. Samples of this solution or a 2 mM TA solution were transferred to a disposable polyethylene pipette (total TA volume 1 mL, Thermo Scientific; bulb dimensions: diameter = 12 mm, length = 15.4 cm, thickness = 0.35 ± 0.05 mm). The bulb end of the pipette was submerged in a tank of degassed (20% dissolved oxygen), filtered (10-µm pore size) water and affixed to a motor-controlled three-axis positioning system (TDC001, Thorlabs, Inc., Newton, NJ, USA) (Figure 4.1). Histotripsy pulses were generated by an eight-segment, spherically focused 1-MHz transducer with a 10-cm aperture and 7.5 cm focal length. All elements of the transducer were excited in parallel by a custom-designed and built class D amplifier and matching network.[185, 234] The nonlinear field and acoustic output at the focus of the transducer were measured with a fiber optic hydrophone (HFO-690, Onda Corp., Sunnyvale, CA, USA) for peak negative pressures up to 20 MPa peak negative pressure. The -3 dB widths of the focal zone are 7.5 mm x 0.5 mm x 0.5 mm. Prior to sonication, scan line B-mode images were acquired to visualize the pipette. Test pulses of 29 MPa PNP using the pulse duration and pulse repetition frequency (PRF) of interest were performed to verify localization of the bubble cloud within the pipette and to determine the starting and ending positions for sonication. The pipette was translated in 0.5 mm increments to raster the focal region vertically through the 1-mL sample volume. At each position, a total of

500 pulses were applied with durations of 5 or 20 cycles and pulse repetition frequencies of 20 or 100 Hz (Table 4.1). The peak negative pressures of the pulses were 24, 26.5, 29, 34, or 39 MPa. Following sonication, all nanoparticle samples and controls were centrifuged for 20 minutes at 13,200 RPM, and the clear supernatant was recovered for fluorescence measurement.

Table 4.1: Number of samples for each insonation condition. 2 mM TA solutions were prepared with and without 0.354 mg/mL of TiO_2 nanoparticles.

	TA solution alone				**TiO_2 particle solution**			
Peak negative pressure (MPa)	**5 cycles, 20 Hz PRF**	**5 cycles, 100 Hz PRF**	**20 cycles, 20 Hz PRF**	**20 cycles, 100 Hz PRF**	**5 cycles, 20 Hz PRF**	**5 cycles, 100 Hz PRF**	**20 cycles, 20 Hz PRF**	**20 cycles, 100 Hz PRF**
24	5	N/A	N/A	N/A	3	N/A	N/A	N/A
26.5	5	N/A	N/A	N/A	3	N/A	N/A	N/A
29	5	4	4	3	4	4	4	3
34	5	N/A	N/A	N/A	3	N/A	N/A	N/A
39	5	N/A	N/A	N/A	3	N/A	N/A	N/A

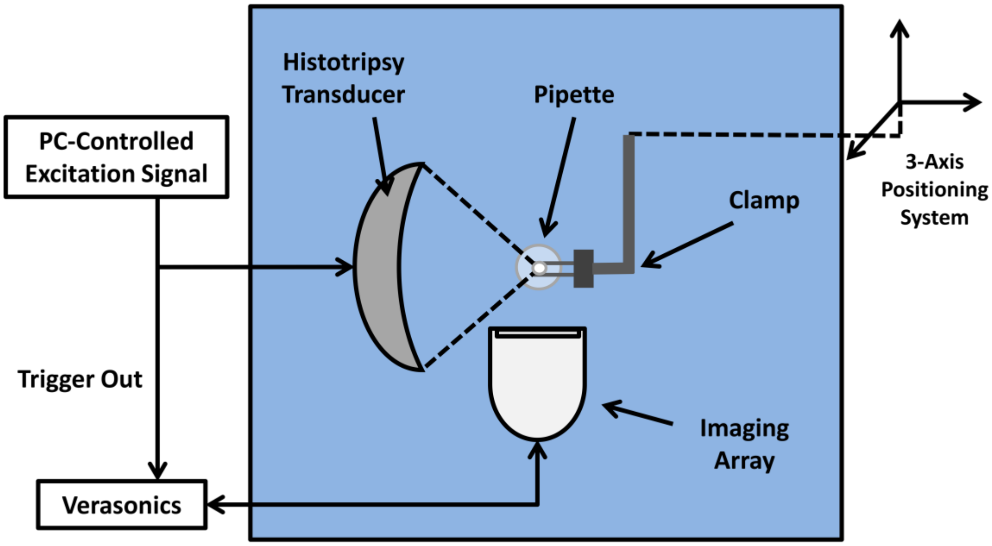

Figure 4.1. Top-down diagram of experimental setup for sonication and imaging of pipette sample. The histotripsy source is focused on the center of the disposable polyethylene pipette, which translates vertically (in and out of the page) between each set of pulses. The imaging array is positioned orthogonally to the therapeutic source to capture a cross-sectional image of the pipette. A conventional scan line B-mode image was acquired prior to each set of pulses. During sonication, passive cavitation images were acquired every 10th trigger pulse.

4.2.3 Monitoring and quantification of cavitation

At each insonation location, bubble cloud acoustic emissions generated by the bubble cloud were recorded with an L11-4v imaging array (Verasonics, Inc., Kirkland, WA, USA) using a research ultrasound scanner system (Vantage 128, Verasonics, Inc., Kirkland, WA, USA) triggered by the histotripsy transmit electronics.[47] Briefly, bubble cloud emissions were passively received over a 60-µs duration starting 5 µs prior to the histotripsy pulse focal insonation. Emissions were processed offline to generate passive cavitation images with a delay, sum, and integrate method in the frequency domain over the receive bandwidth of the imaging array (2–10 MHz).[50] During the 500 applied pulses per position, cavitation emissions used to form passive cavitation images were acquired every tenth trigger pulse due to data transfer-rate limitations, resulting in 50 frames per location, which were summed to generate a cumulative passive cavitation image for each insonation location within the sample. Additionally, all locations were summed over each pipette sample (21 locations for each sample × 50 frames = 1050 frames/data set) to form a cumulative image of bubble emissions for each data set.

4.2.4 Fluorescence measurement

Fluorescence measurement of HTA generated by ultrasound exposure was carried out using a spectrofluorometer (Fluorolog-3, Horiba Jobin Yvon, Kyoto, Japan) with an excitation wavelength of 318 nm.[112] Emission spectra following sonication for the range of insonation pressures studied are shown in figure 4.2. Excitation and emission window widths were 2 and 10 nm, respectively. Samples were transferred to a 500-µL quartz cuvette and scanned in triplicate to produce an average emission spectrum. The quantity of HTA for each sonicated sample was reported as:

$$HTA(\mu M) = \frac{F_{samp} - F_{ctrl}}{F_{ref} - F_{blank}} \bullet C_{ref},$$

where F_{samp}, F_{ctrl}, F_{ref}, and F_{blank} are the fluorescence intensities measured at 424 nm[235] for a sonicated TA (or TiO_2 in TA solution) sample, an unsonicated control TA (or TiO_2 in TA solution) sample, a reference HTA standard, and a blank PBS sample, respectively. The concentration of the reference HTA standard, C_{ref}, was 0.1 μM. The terephthalate assay is reported to be linear over the range of 0.2–20 μM.[233, 236] An additional calibration curve confirmed linearity of fluorescence at 424 nm over HTA concentrations from 0.025 to 0.2 μM (Figure 4.2).

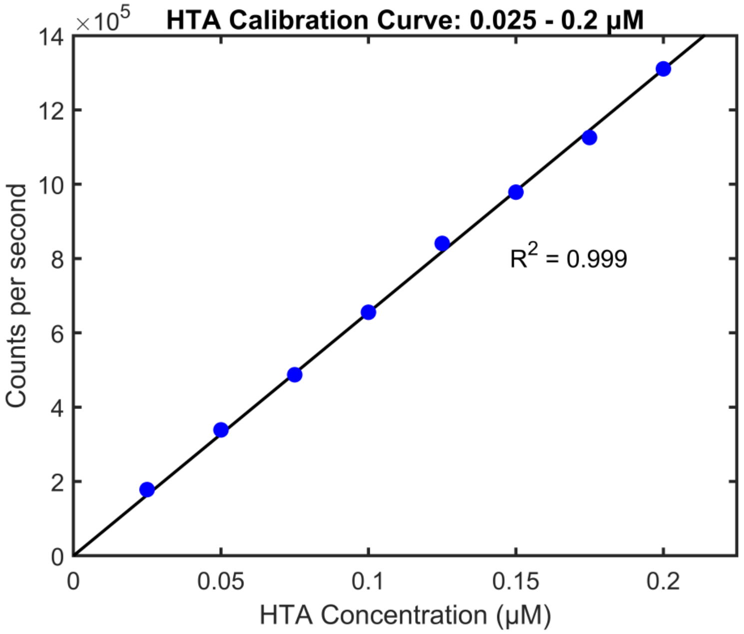

Figure 4.2. Calibration curve (black fitted line) for fluorescence measurement of 2-hydroxyterephthalic acid (HTA) over the range of concentrations observed in this study.

4.2.5 Cavitation measurement, correlation with ROS production, and statistical analysis

For each sonication position in a given pipette sample, the total generated acoustic emission power was obtained by spatially integrating the passive cavitation images. These integrated values were summed over all sonication positions to obtain a single acoustic power measurement for each sample. Representative co-registered B-mode and passive cavitation images are depicted in figure 4.3.

The degree of HTA generation and bubble activity were compared across experimental groups using the statistics package in MATLAB (MathWorks, Natick, MA, USA). The concentrations of HTA produced in sonicated TA samples with and without TiO_2 particles were compared across peak negative pressure levels and sonication parameters using a one-way unbalanced analysis of variance (ANOVA) with Tukey's honestly significant difference (HSD) as a post hoc test. The summed bubble activity measured via PCI generated in TA samples with and without TiO_2 particles were also compared across peak negative pressure levels using a one-way unbalanced ANOVA with Tukey's HSD as a post hoc test. The computed total PCI powers of all sonicated samples were tested for significant correlations with HTA concentrations using Pearson's correlation coefficient. All statistical analysis was performed with an α level of 0.05.

4.3 Results

4.3.1 Observation of bubble activity

Pipettes were readily visualized with scan line B-mode imaging (Figure 4.3a). Acoustic power mapped via PCI indicated a strong source of emissions within the pipette (Figure 4.3b). Due to the delay, sum, and integrate beamformer used, acoustic power maps were blurred in the range dimension, resulting in some artefactual mapping of emissions outside the pipette. B-mode imaging confirmed that bubble activity was contained within the pipette for all 5-cycle pulses and for 20-cycle pulses at 20 Hz PRF. For 20-cycle, 100 Hz PRF excitations, some cavitation activity extended beyond the pipette into the surrounding water, although the majority of bubble activity was constrained to the pipette for all sonication positions.

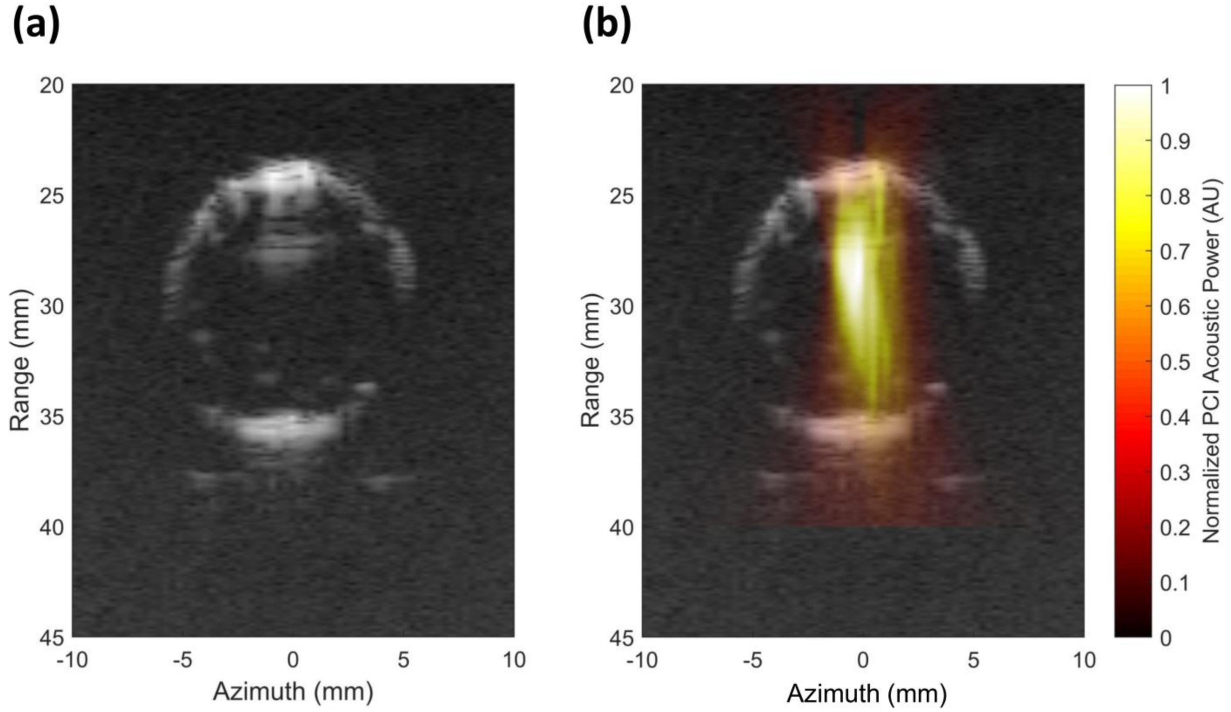

Figure 4.3. (a) Scan line B-mode image acquired prior to sample sonication showing the polyethylene pipette outline (total TA volume 1 mL, Thermo Scientific; bulb dimensions: diameter = 12 mm, length = 15.4 cm, thickness = 0.35 ± 0.05 mm); (b) Coregistration of B-mode image of the pipette with passive cavitation image.

At a peak negative pressure of 24 MPa, only sparse cavitation was observed at 3–5 of the insonation positions. Cavitation became more consistent with increasing peak negative pressure. For peak negative pressures less than 29 MPa, cavitation appeared suppressed for locations within 1 mm of the top of the sample possibly due to strong reflection at the fluid/air interface. Cavitation occurred at all sonication positions with few to no interruptions for all 34 and 39 MPa sonciations, and all 20-cycle and/or 100 Hz PRF sonications.

The strength of bubble activity for the 5-cycle excitations as a function of peak negative pressure, indicated by the summed passive cavitation images, is noted in Figure 4.4. For arms with and without TiO2, the strength of bubble cloud emissions increased with the peak negative pressure. For a given peak negative pressure, the total acoustic power did not differ significantly for insonation of TA solutions with or without TiO_2.

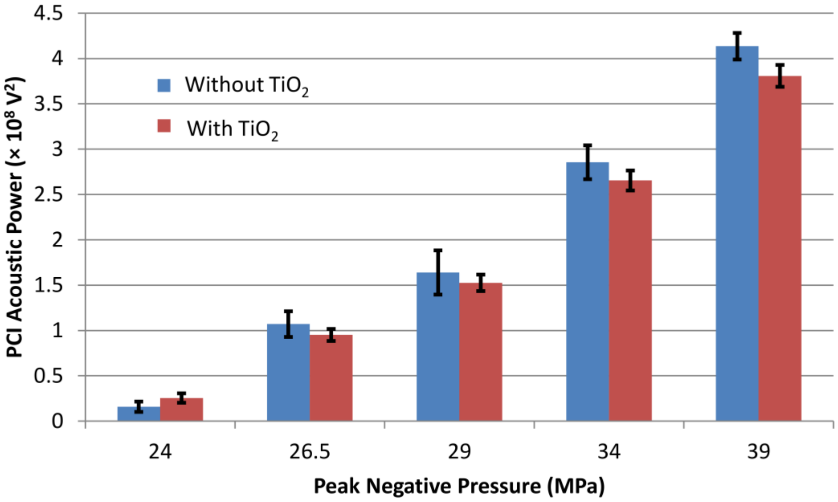

Figure 4.4. Total PCI acoustic power measured from passive cavitation images as a function of peak negative pressure for sonicated TA solutions with (red bars) and without (blue bars) TiO_2 particles.

4.3.2 ROS production with varying PNP

Fluorescence emissions of HTA generated in sonicated samples of TA with and without TiO_2 particles resulted in similar peaks centered at 424 nm (Figure 4.5). In the absence of TiO_2 particles, HTA concentrations produced by cavitation increased linearly ($R^2 = 0.968$) with the peak negative pressure from 0.003 ± 0.002 μM at 24 MPa to 0.117 ± 0.012 μM at 39 MPa (Figure 4.6). Sonicated solutions of TiO_2 contained HTA concentrations that also increased linearly with peak negative pressure ($R^2 = 0.991$), ranging from 0.009 ± 0.004 μM to 0.111 ± 0.001 μM. The HTA generation rate (calculated as the concentration of HTA produced per unit on-time of the therapy source) ranged from 0.02–2.45 μM/s and from 0.12–2.14 μM/s for TA and TiO_2 samples, respectively, over the range of pressures studied. For any given peak negative pressure, no significant difference was observed in HTA production for arms with and without TiO_2.

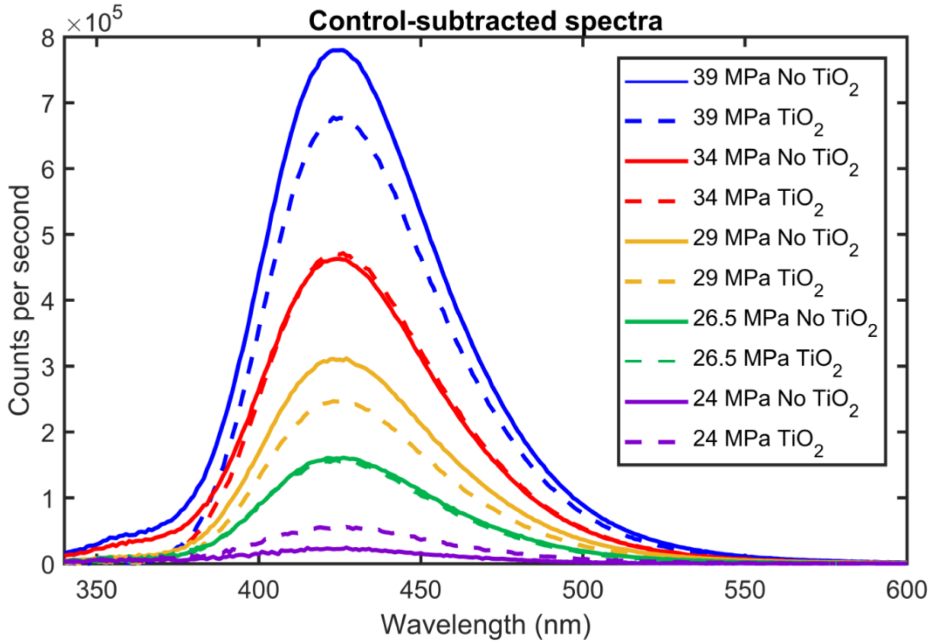

Figure 4.5. Emission spectra of 2 mM terephthalic acid samples with (dashed lines) and without (solid lines) TiO_2 particles, sonicated with pulses of 24–39 MPa peak negative pressure (5-cycle pulse duration, 1-MHz fundamental frequency, 20 Hz pulse repetition frequency). Spectra were averaged over n = 3–5 samples per pressure level (see table 4.1). The spectra of corresponding control samples (unsonicated 2 mM TA or unsonicated, centrifuged 2 mM TA with 0.35 mg/mL TiO_2) were subtracted to better visualize the emission peak.

A strong correlation was observed between ROS production and bubble activity tracked with passive cavitation imaging (Figure. 4.7). A linear relationship was observed between HTA concentration and the intensity of bubble activity (R^2 = 0. 989 and 0.952 for samples with and without TiO_2, respectively). No significant difference was observed in the slopes of the linear fits to this data (red and blue lines in Figure 4.7).

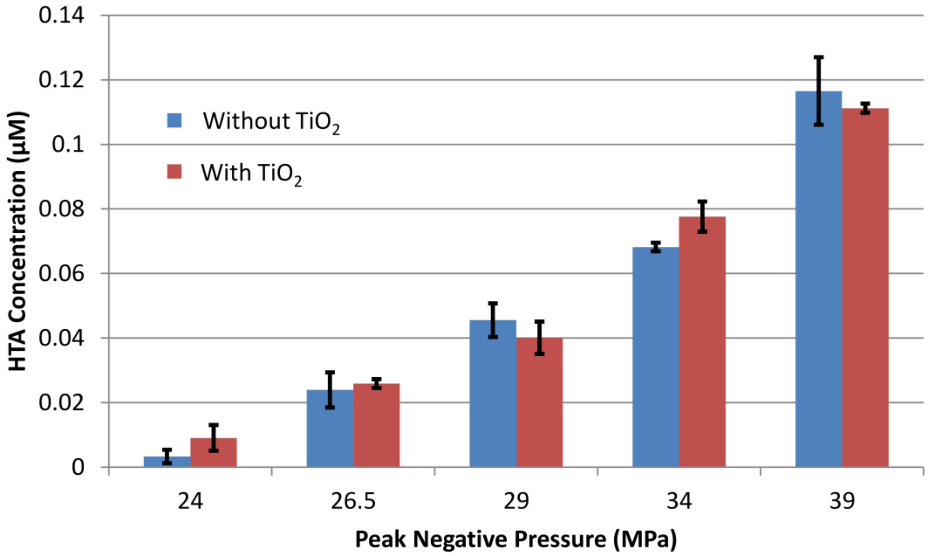

Figure 4.6. 2-hydroxyterephthalic acid (HTA) generation as a function of peak negative pressure for sonicated TA solutions with (red bars) and without (blue bars) TiO_2 particles. No significant differences in HTA concentration between particle and non-particle samples were observed at any pressure level. HTA concentration increased significantly with each change in peak negative pressure.

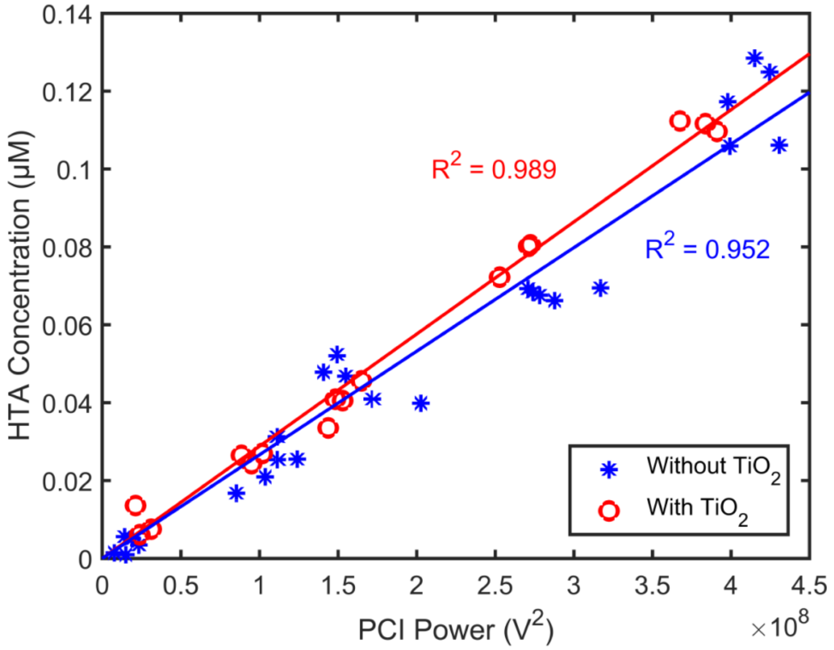

Figure 4.7. Concentration of 2-hydroxyterephthalic acid (HTA) as a function of the total acoustic power measured from passive cavitation images. Samples with (blue stars) and without (red circles) TiO_2 sonicated with 5-cycle, 20 Hz PRF pulses of 24–39 MPa peak negative pressure.

4.3.3 ROS production with varying sonication parameters

The pulse duration and repetition frequency had a significant impact on •OH generation, as shown in Table 4.2. Sample-averaged spectra for each set of insonation parameters are shown in Figure 4.8. Increasing the pulse repetition frequency from 20 to 100 Hz for 5-cycle pulses significantly increased the measured HTA concentration by a factor of 1.6 and 2.0 for non-particle and particle sonications, respectively. Increasing the pulse duration from 5 to 20 cycles at 20 Hz PRF significantly increased HTA generation by a factor of 3.6 and 4.7 for non-particle and particle sonications, respectively. The HTA production rate, or increase in HTA per total ultrasound exposure time, did not change significantly between 5- and 20-cycle pulses at 20 Hz PRF, but decreased significantly between 5- and 20-cycle pulses at 100 Hz PRF. HTA production rate was not significantly different between particle and non-particle solutions for any set of sonication parameters. Insonations of 20-cycle duration at 100 Hz PRF generated significantly more •OH than 5-cycle, 100 Hz PRF pulses, but significantly less than 20-cycle, 20 Hz PRF pulses. TiO_2 particle samples generated significantly more •OH than non-particle samples under exposure to 20-cycle, 20 Hz PRF pulses (Figure 4.9).

Table 4.2: Total 2-hydroxyterephthalic acid (HTA) concentrations and HTA generation rates for the two pulse durations and two pulse repetition frequencies tested. All sonications were performed at 29 MPa peak negative pressure. Errors are given as standard deviations.

	TA solution alone				**TiO_2 particle solution**			
	5 cycles, 20 Hz PRF	**5 cycles, 100 Hz PRF**	**20 cycles, 20 Hz PRF**	**20 cycles, 100 Hz PRF**	**5 cycles, 20 Hz PRF**	**5 cycles, 100 Hz PRF**	**20 cycles, 20 Hz PRF**	**20 cycles, 100 Hz PRF**
Total HTA (µM)	0.046 ± 0.005	0.074 ± 0.010	0.163 ± 0.011	0.105 ± 0.004	0.040 ± 0.005	0.081 ± 0.006	0.187 ± 0.014	0.123 ± 0.004
HTA production rate (µM/s)	0.87 ± 0.10	1.41 ± 0.20	0.78 ± 0.05	0.50 ± 0.02	0.76 ± 0.10	1.54 ± 0.11	0.89 ± 0.07	0.59 ± 0.02

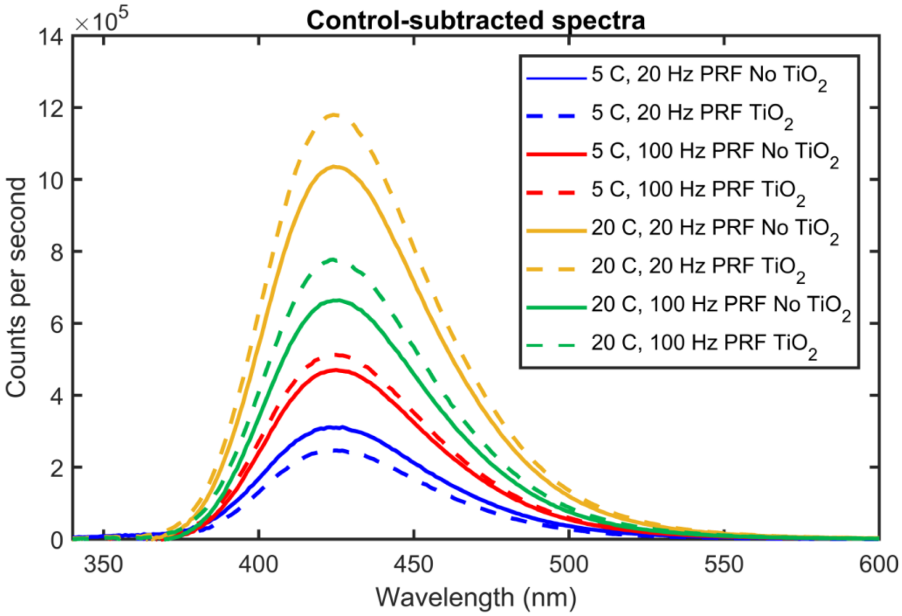

Figure 4.8. Emission spectra of 2 mM terephthalic acid samples with (dashed lines) and without (solid lines) TiO_2 particles, sonicated with 5- or 20-cycle (5 C, 20 C) pulses of 20 or 100 Hz PRF and 29 MPa peak negative pressure. Spectra were averaged over n = 3–5 samples per pressure level (see table 4.1). The spectra of corresponding control samples (unsonicated 2 mM TA or unsonicated, centrifuged 2 mM TA with 0.35 mg/mL TiO_2) were subtracted to better visualize the emission peak.

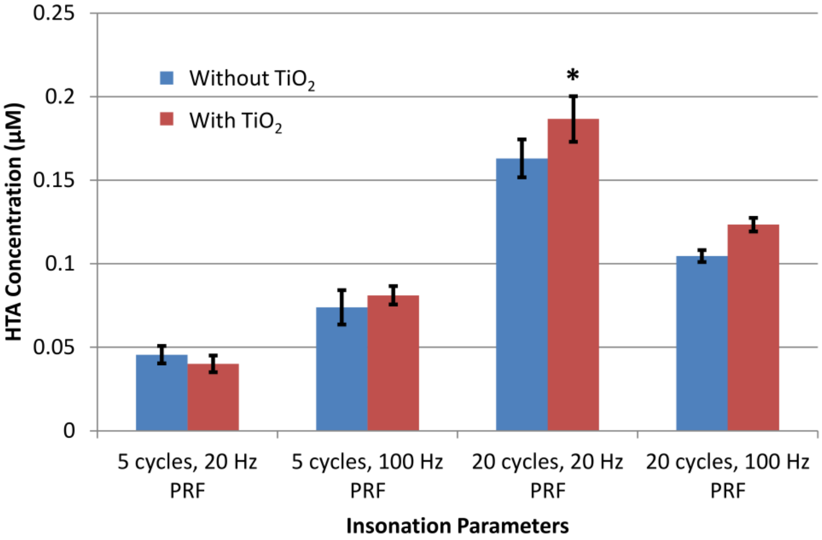

Figure 4.9. 2-hydroxyterephthalic acid (HTA) generation as a function of sonication parameters for sonicated TA solutions with (red bars) and without (blue bars) TiO_2 particles. When considering particle and non-particle samples individually, each set of sonication parameters resulted in a significantly different concentration of HTA. The asterisk (*) indicates a significant difference between particle and non-particle samples.

4.4 Discussion

4.4.1 Generation of ROS by ultrasound exposure

The total HTA generated by histotripsy-induced bubble activity in this study is considerably smaller than that reported previously for other types of ultrasound exposure.[112, 235] The HTA production rate (total HTA production relative to total insonation duration) ranged from approximately 0.5 to 2.5 μM/s in this study, which is greater than HTA production rates estimated from data provided by Somaglino et al.[112] (0.1–0.7 μM/s) and Villeneuve et al.[235] (~0.03 μM/s). Both studies utilized 1-MHz focused sources, but employed longer duration pulses (250–1,250 cycles in duration[112] or continuous wave excitation[235] vs. 5–20 cycle duration employed here) and lower peak negative pressures (1–19 MPa vs. 24–39 MPa for the present study). Since •OH production is dependent on collapsing bubbles achieving the high temperatures and pressures necessary for pyrolysis,[223] these results suggest that histotripsy excitation produces intense bubble collapse and large quantities of sonochemical reactions during a brief period following the pulse, but the low duty cycle limits the overall production of •OH. Bubble clouds induced by histotripsy pulses have been shown to be largely invariant in size and position over a 50-ms period following the pulse.[237] Application of a secondary pulse following the initial excitation to drive inertial collapse of these bubbles may increase the production of •OH. This may also prevent repeat-excitation of bubble clouds, improving the homogeneity of ROS production.

Altering the insonation parameters also affected the degree of HTA production. Increasing the pulse duration by a factor of four resulted in an approximately equal increase in HTA (0.046 μM vs. 0.163 μM for five and 20 cycle pulses, respectively) when pulses were applied at a 20 Hz rate. The extension of the total transducer on time for the longer pulses should extend the duration of the inertial bubble activity and resultant sonochemical production of •OH accordingly. The consistency in HTA generation rate between 5- and 20-cycle pulses for the 20 Hz PRF setting suggests consistent inertial bubble activity over the duration of the pulse. Increasing the PRF from 20 to 100 Hz for the 5-cycle pulses increased the HTA generation rate by approximately a factor of two, but decreased it by approximately 65% for the 20-cycle pulses. At higher PRFs, cavitation bubbles become repeatedly excited and do not have sufficient time for dissolution between pulses.[198] As a result, the bubble cloud from 5-cycle pulses, which was well-contained within the pipette, experienced more repeat excitation of bubbles, which may have improved the consistency of cavitation and thus the HTA generation rate. However, for the shock-scattering mechanism utilized here, the volume of the bubble cloud expands considerably toward the histotripsy source over the course of a 20-cycle pulse compared with a 5-cycle pulse.[46] The most intense bubble activity is located at the proximal end of this cloud, as evidenced by PCI data acquired in this and previous studies.[47, 232] In the case of 20-cycle, 100 Hz PRF pulses, repeated excitation of the proximal edge of the bubble cloud, which was near the proximal edge of the pipette, shielded the pipette interior and reduced cavitation activity during the sonication.

The bubble cloud acoustic power tracked with passive cavitation imaging increased linearly with HTA production. These data indicate a strong correlation between the strength of bubble activity and sonochemical reactions. The spectrally integrated PCI data in this study are a quantitative measure of the broadband emissions associated with inertial bubble collapse,[50] and the locations of strongest emissions are therefore expected to correspond to locations of greatest ROS production. Previous studies have utilized single-element passive cavitation detectors to quantify bubble activity and have shown it to correlate with sonochemical generation of •OH.[112]

These detectors do not provide information regarding the spatial distribution of bubble activity, whereas the results of the current work indicate passive cavitation imaging can track the specific locations of bubble activity sufficient for generating ROS. Under histotripsy insonation in an *in vivo* setting, cavitation activity may not spatially coincide with locations of sonosensitizer accumulation. Conjugation of sonosensitizers to phase-shift emulsions,[238] mesoporous particles,[239] or nanocups,[240] could help ensure close proximity of the cavitation activity to the sonosenstizers and promote targeted therapy via functionalization. Particles with hydrophobic surfaces can also harbor cavitation nuclei, improving cavitation efficiency.[241] Such approaches have been shown to improve the efficacy of sonodynamic therapy.[242]

Histotripsy induces homogenization of cells and tissue structure through the mechanical action of cavitation.[41] The marginal tissue adjacent to the liquefaction zone, while physically intact, may undergo delayed cell death via other mechanisms of collateral damage from histotripsy.[243, 244] Given the low overall production of •OH during the histotripsy insonations performed in this study, ROS-induced damage seems an unlikely mechanism of cell death under histotripsy exposure. Furthermore, the margins of mechanical tissue disruption from histotripsy are very sharp, and the ROS generated in the liquefaction zone (primarily hydroxyl radicals) are likely too short-lived to diffuse to the peripheral margin.[57] Hiraoka et al. have also demonstrated that •OH radicals and singlet oxygen do not take part in the enhancement of ultrasound-enhanced cell death with sonosensitizing particles, and that mechanical stresses such as disruption of cellular membranes are sufficient to explain the reduction in cell survival.[245]

4.4.2 Histotripsy exposure of TiO_2

The histotripsy-induced bubble activity initiated in this study did not appear to stimulate ROS production from TiO_2 particles, despite the known relationship between inertial cavitation and effective SDT.[223, 224, 246] There may be several reasons for this lack of sonocatalytic ROS generation. TiO_2 produces ROS upon exposure to ultraviolet light,[228, 247] which is aligned with the sonoluminescence spectrum from cavitation in oxygen-saturated water (200–500 nm).[248] This indicates that a sonoluminescent histotripsy exposure would be required for activation of TiO_2. Although light emissions were not measured in this study, the lack of increased •OH in the presence of TiO_2 particles suggests minimal generation of sonoluminescent light. Previous work has demonstrated an approximately two-fold increase in total ROS production with ultrasound irradiation of anatase TiO_2 compared with ultrasound irradiation alone, but used long (~60 min) sonications at 40 kHz.[249] This may indicate that bubble dynamics under histotripsy excitation are distinct from those under other forms of acoustic cavitation. In particular, the bubble collapse may not be sufficiently strong to generate sonoluminescent light. There is a significant diffusion of gas from the surrounding solution into the bubble throughout a multiple-cycle histotripsy excitation.[250] The gaseous core will be a limiting factor in the intensity of the bubble collapse, which may decrease the probability of sonoluminescence occurring. This is supported by observations of increased sonoluminescence when decreasing the dissolved oxygen content of the solution.[251] In this study, the gas-saturated PBS (~20.9% O_2) used as the sonication medium is not generally representative of dissolved oxygen content in human tissues (1–11% O_2).[252] In addition to being more physiologically relevant, performing sonications in degassed media may mitigate gas diffusion and facilitate more intense bubble collapse. On the other hand, inhibition of bubble collapse by gas diffusion would likely increase at higher pressures, which is not indicated by the continual increase in acoustic power and •OH generation with pressure observed in this study. It may be that ROS production by the collapsing bubble is not impacted by gas diffusion, whereas sonoluminescence is inhibited.

The apparent absence of strong light emissions despite the high driving pressures of the histotripsy pulses may have implications for the mechanism of histotripsy ablation. If the bubble collapse is not violent enough to induce sonoluminescence, then it may not play a major role in mechanical liquefaction by histotripsy. Analytic models and numerical computations of bubble expansion in elastic media have demonstrated that, under histotripsy excitation, a bubble's expansion induces considerably more mechanical strain on surrounding cells and tissue structure than its inertial collapse.[253] The increased efficacy of histotripsy ablation at greater peak negative pressures, despite increased gas diffusion and buffering of bubble collapse,[250] further supports rarefaction-induced strain of the bubble as the predominant factor in tissue liquefaction.

In addition to the effects of bubble dynamics, the properties of TiO_2 particles can significantly influence the efficacy of SDT. This study utilized 30 nm anatase TiO_2 particles. Both anatase and rutile crystalline structures of TiO_2 have been used successfully as sonocatalytic agents,[254, 255] but rutile TiO_2 particles have been shown to produce •OH more efficiently than anatase under ultrasonic irradiation.[255, 256] The anatase structure may also be susceptible to damage from cavitational ultrasound, as evidenced by its decreased sonocatalytic activity with increasing ultrasound pressure.[255] This may explain the minimal activation of anatase TiO_2 in the current study, which used very high ultrasonic pressures. In addition, rutile TiO_2 exhibits greater oxygen adsorption, reducing the dissolved oxygen at the particle surface.[257] This can promote generation of oxygen radicals as well as mitigate oxygen influx into histotripsy bubbles to promote a stronger bubble collapse, two beneficial factors in SDT. Composites of anatase and rutile TiO_2 of varying size and surface structure have been shown to further increase photo- and sonocatalytic activity by balancing the oxidation properties of anatase with the stability and gas adsorbability of rutile.[256, 257]

TiO_2 nanoparticles can vary in their hydrophilicity, with anatase being generally more hydrophilic than rutile forms.[258] Hydrophobic particles would be expected to harbor cavitation nuclei and reduce the threshold ultrasonic pressure necessary for cavitation. In this study, no differences in measured acoustic power were observed between particle and TA solutions, suggesting a more hydrophilic TiO_2 particle. The use of rutile TiO_2 with histotripsy excitation could improve nucleation of cavitation, but may also facilitate particle aggregation, which has been shown to reduce light absorption and photocatalytic activity.[259] PEGylation of rutile TiO_2 nanoparticles would prevent aggregation, improving both sonocatalytic efficiency and biocompatibility.[260, 261] Sonocatalytic activation by histotripsy may be more effective for different semiconductor oxides, such as zinc-oxide, magnetite or maghemite.[242] Furthermore, doping of TiO_2 and other inorganic sonosensitizers can increase efficacy by preventing electron/hole recombination.[262]

4.4.3 Limitations

The methods and results presented in this work contain several limitations. A relatively small sample size for each sonication condition (N = 3–5) limits the strength and generalizability of the conclusions. The TA assay utilized in this study is only sensitive to •OH generation. Hydroxyl radicals are the primary species produced in the experimental conditions explored here, though other species are also produced by sonochemical reactions and sonostimulation of TiO_2, such as superoxide and singlet oxygen.[249] A more comprehensive evaluation of the total ROS production could be achieved through the oxidation reaction from 1,5-diphenyl carbazide (DPCI) to 1,5-diphenyl carbazone (DPCO). The addition of radical scavengers such as L-histidine (His), dimethylsulfoxide (DMSO) and thiourea (TU) can help distinguish production of hydroxyl radicals from singlet oxygen.[256] Electron paramagnetic resonance (EPR) imaging can also quantify and distinguish a wide variety of reactive oxygen and nitrogen species.[263] Bubble cloud behavior and sonoluminescent emissions depend on the gas content,[251] temperature,[264] and medium elasticity,[253] and so the soncications performed in gas-saturated PBS in this study may not be physiologically relevant. In this study, passive cavitation images were only acquired over a 60-μs duration, but some of the cavitation cloud inertial collapse may occur more than 60 μs after the focal insonation. A longer PCI acquisition window could provide more reliable information regarding the bubble activity, but at the cost of a reduced maximum image sampling rate. Finally, while the absence of notable sonostimulation of TiO_2 would seem to indicate a lack of sonoluminescence, definitive conclusions cannot be drawn without actual measurement of light emissions.

4.5 Conclusions and Future Work

This study explored histotripsy insonation as a sonocatalytic and sonodynamic adjuvant. Overall, relatively small concentrations of •OH radical were produced, but the rate of •OH generation was at least an order of magnitude greater than previous studies that utilized longer cavitational pulses or continuous wave sonications. •OH generation was dependent on the ultrasound pressure, pulse duration, and pulse repetition frequency, but a combination of long pulses and high PRF hindered its production. The histotripsy pulses did not appear to successfully stimulate appreciable •OH generation from TiO_2 particles. This may reflect insufficient sonoluminescence as a result of gas diffusion-buffered collapse of the histotripsy-generated bubbles, or that the TiO_2 formulation used here is ill-suited to activation by histotripsy. Finally, passive cavitation imaging provided a reliable metric for measuring •OH production by histotripsy exposure, and may therefore be well-suited for image guidance of SDT.

Future studies should investigate light production as a function of histotripsy pulse parameters. This could be performed with a photomultiplier tube (PMT) in a light-isolated tank positioned below the pipette and affixed to the three-axis positioning system to allow co-translation of the pipette and PMT. A fiber optic cable could also be inserted through the top of the pipette to achieve closer proximity to the bubble activity in the solutions. The use of rutile TiO_2 particles or rutile/anatase composites, alternative sonosensitizing particles, or doping agents could also be explored to increase the sonodynamic efficacy. Variation of the temperature and dissolved gas content in the sonicated solution should also be tested, with attention to physiologically relevant gas concentrations. Nonetheless, this study demonstrated that histotripsy sonication is capable of producing sonochemical reactions and hydroxyl radical, and this activity is quantifiable through passive cavitation imaging.

CHAPTER 5

CONCLUSIONS

5.1 Overview of Work

This dissertation has explored several novel applications of therapeutic ultrasound for disease pathologies resistant to conventional interventions. Thermal ultrasound ablation has made only marginal inroads into clinical practice as a therapeutic modality, and histotripsy and sonodynamic therapy are not yet used clinically outside of case reports and early-phase clinical trials. The primary remaining obstacles to clinical translation of these modalities are limited therapeutic efficacy over alternative available treatments and limited reliability of image guidance. In this dissertation, several promising improvements to both efficacy and image guidance of these therapeutic ultrasound modalities were explored. As indicated by the first aim of this work, combinatorial treatments involving phase shift emulsions can enhance thermal ablation with no degradation of MR image-based evaluation of TULSA ablation zones.[82] However, therapeutic outcomes were not consistent, and no MR contrast release was observed from the encapsulated Gd_2O_3, suggesting limited utility of sUPEs as TULSA-activated delivery or contrast agents. The remaining work of this dissertation focused on histotripsy ablation. The second aim explored the utility of diagnostic ultrasound and MR image parameters for guidance, monitoring, and evaluating treatment efficacy of histotripsy. From these studies, it was shown that diagnostic ultrasound and MRI can provide supplementary information toward the goal of pre-treatment planning, real-time monitoring, and post-treatment evaluation of histotripsy ablation.[232] Passive cavitation imaging provides the best real-time indication of the bubble activity, whereas MRI provides high-resolution, high-contrast visualization of the ablation zone. The final aim of this work involved preliminary study of the feasibility of a combinatorial therapy involving histotripsy and sonodynamic therapy. Histotripsy was shown to be capable of generating ROS through sonochemical reactions, although efficiency was limited by the short duration of histotripsy pulses. ROS were produced at appreciably greater rates than previously observed, but at low overall yields. Further, histotripsy seemed ill-suited to sonoactivation of TiO_2 sensitizing particles for sonodynamic therapy, suggesting minimal generation of sonoluminescence. Alterations to the composition of the sensitizing particle and the ultrasound parameters used are both promising methods for improving sonocatalytic activity via histotripsy and sonoluminescent stimulation of TiO_2.

5.2 Enhancement of TULSA Therapy with sUPEs

Numerous formulations of theranostic particles have been explored previously for purposes of HIFU therapy enhancement. In particular, microbbubles and phase-shift emulsions have been used for bubble-enhanced heating in therapeutic ultrasound.[127, 160, 178] Silica-based nanoparticles are popular for their easy functionalization, allowing targeted delivery of imaging contrast agents and therapeutics.[77] This dissertation investigated the use of a novel silica-shell phase-shift emulsion intended for enhanced heating and delivery of therapeutics during ablative ultrasound therapy, with MR contrast for improved delineation of ablation zones. This approach has not been explored with an unfocused TULSA device. The results of this work suggest that such arrays are inefficient for transitioning large quantities of pressure-sensitive sUPEs, although newer, dual-frequency models may be more effective. Previous studies of ultrasound-activated MR contrast agents have optimized particle size and composition for maximum contrast enhancement,[146–148] which was not performed in this work, although contrast was observed from ruptured sUPEs *in vitro*. This work exhibited altered lesion morphology and thermal fixation in sUPE treatment arms, suggesting bubble-enhanced heating even with an unfocused transurethral array. Previous work has also demonstrated thermally fixed tissue following rapid ablation of the prostate.[118, 158] Both MR thermometry and passive ultrasound imaging have been demonstrated as indicators of bubble-enhanced heating from phase-shift emulsions.[178] This dissertation also verified the integrity of evaluative MR imaging *in vivo* in the presence of exogenous contrast and bubble-enhanced heating agents, which has not been established. However, thermal-dose metrics tended to overestimate the ablation boundaries, in agreement with previous studies.[68] The 55°C isotherm and nonperfused volumes were more reliable indicators of ablation. In contrast to previous studies,[84, 139, 166] differential MR contrast on DWI and T_2W imaging was observed in the presence of thermally fixed lesions. The first aim of this dissertation was limited by a small sample size, therapy transducer parameters, and a less than comprehensive characterization of sUPEs.

5.3 Multi-modal imaging assessment of histotripsy ablation

The safety and efficacy of histotripsy ablation of human prostate tissue has been demonstrated,[176] but would greatly benefit from improved image guidance and evaluation. The second aim of this thesis combined registered image data sets for comparison of gross and histologic ablation and liquefaction with diagnostic ultrasound and MR imaging. Previous work has assessed quantitative MR parameters such as T_1, T_2, and apparent diffusion[52] or diagnostic ultrasound methods such as passive cavitation imaging[47] individually as indicators of histotripsy liquefaction. The current work demonstrated the superior sensitivity and specificity of bubble-monitoring techniques over post-hoc evaluative imaging in predicting spatial locations of histotripsy liquefaction, in agreement with previous studies.[47] This result is a promising step toward clinical application of histotripsy guided with B-mode and passive cavitation imaging. This aim also explored the complimentary information provided by MR and ultrasound image modalities. In particular, T_2W MR imaging allowed more reliable delineations of liquefaction zones than B-mode imaging, which exhibited highly inconsistent appearances of liquefaction zones. Given B-mode imaging is the primary method of monitoring histotripsy ablation, this result is somewhat troubling, and suggests combinatorial image guidance with diagnostic ultrasound and MRI could improve outcomes in histotripsy ablation. This study was also one of few to examine quantitative changes in MR image properties of phantoms and *ex vivo* tissues following histotripsy ablation. In contrast with previous work, which exhibited largely uniform histotripsy lesions with MRI,[52] the current studies demonstrated spatial variation in T_2W and diffusion-weighted MRI over the length of histotripsy lesions. These variations corresponded to the apparent severity of liquefaction in tissues, which further supports the utility of multi-modal image guidance in histotripsy ablation. Although it provided interesting results in a variety of *ex vivo* tissues and tissue-mimicking phantoms, this study does not represent an *in vivo* assessment of histotripsy ablation, and its binary classification of liquefaction may oversimplify the mechanical ablation process. The analysis is also based on a post-hoc evaluation of histotripsy, and did not monitor the treatment progress in real time.

5.4 Histotripsy-mediated production of ROS

The final aim of this thesis tested histotripsy as a method for generating sonochemical reactions in sonodynamic therapy. Shock-scattering histotripsy generates intense cavitational bubble activity with negligible thermal effects,[46] making it a promising candidate for a sonodynamic adjuvant.[215] Recent advances in sonodynamic therapy have also enabled its effective application in the treatment of prostate cancer.[230, 265] In the current work, histotripsy exposure of saline solution in the absence of sonosensitizing particles resulted in lower overall concentrations of hydroxyl radical than previously reported,[112, 235] but an •OH production rate approximately one to two orders of magnitude greater. Therefore, the relatively high pressures of histotripsy insonations appear to accelerate ROS generation, but the low duty cycles limit the total amount of ROS produced. Hydroxyl radical production was dependent on the pressure, pulse duration, and PRF of the histotripsy insonation. Acoustic power measured during the excitations with passive cavitation imaging also exhibited a linear relationship with the •OH concentration. Ultrasonic activation of anatase TiO_2 has been demonstrated previously with longer ultrasonic pulses of lower amplitudes,[249] but the current study demonstrated minimal amplification of •OH from histotripsy exposure of anatase TiO_2. This may suggest insufficient luminescence from the bubble collapse, or non-suitability of this TiO_2 formulation to sonocatalysis via histotripsy. This study was limited by a small sample size and an experimental environment that was not representative of physiologic conditions. Information regarding cavitation activity and ROS formation were also limited by the use of an •OH-specific sonochemical assay, limited passive image acquisition, and no direct measurement of light emissions during histotripsy excitation.

5.5 Future work

There are several avenues of research beyond the scope of the current work that could serve to overcome the limitations of therapeutic ultrasound and SDT and facilitate their clinical translation. Chapter 2 of this dissertation explores only one formulation of a gadolinium-doped phase-shift emulsion. Future work should explore other temperature-sensitive MR contrast agents to indicate the ablation zone and obviate the need for contrast injection. Using temperature sensitive particles such as liposomes[73, 266] would likely be a better approach to release contrast or therapeutic payloads during ultrasound ablation. Additionally, using sUPEs with higher-frequency pulsing schemes from focused sources,[145] varying the insonation parameters,[200] or utilizing passive acoustic mapping with ultrasound[50, 178] may ensure more controllable cavitation activity and more consistent bubble-enhanced heating. The formulation of sUPEs could also be optimized to more readily transition under insonation schemes achievable with TULSA applicators, and to improve contrast enhancement upon transition. Iron-based nanoparticles[267] or dual-mode contrast agents[268] may provide more reliable imaging of sUPEs, which can also be employed as ultrasound contrast agents.[126]

Chapter 3 of this dissertation indicates an improvement of histotripsy image guidance when diagnostic ultrasound and MR imaging are combined. The delineation of histotripsy liquefaction zones from imaging to predict cell death or certain biological endpoints is a complex task, well-suited to machine learning.[214] Future studies could utilize deep learning to correlate diagnostic ultrasound and MR images of tissues exposed to histotripsy with spatially registered ground truth histologic tissue samples. These studies should be performed in a variety of clinically relevant tissues to help determine the pathologies best suited to image-guided histotripsy ablation. Quantitative MR measurements using accelerated pulse sequences,[269, 270] while less accurate, would greatly improve the clinical viability of MR-guided histotripsy ablation. However, the disparity in cost between ultrasound and MR imaging motivates further production of diagnostic ultrasound methods for more widespread clinical implementation. Passive cavitation imaging in particular would benefit from new beamforming algorithms to improve two-dimensional spatial resolution.[206] Further study is also needed to reduce the computational burden of PCI beamforming while maintaining adequate spatial resolution.[207] Combining passive cavitation imaging with post-hoc evaluative B-mode imaging would provide a straightforward, low-cost, workflow for histotripsy guidance. These efforts would help adapt the techniques used in this dissertation to real-time clinical treatment guidance, monitoring, and evaluation of histotripsy.

The work presented in Chapter 4 of this dissertation could be extended with a number of avenues of further study. Variation of the rutile/anatase content and the size and shape of the TiO_2 particles used will help determine the optimal formulation for sonocatalysis by histotripsy. The experiments presented here should be repeated with concurrent measurement of light emission, which will allow insight into the mechanism of activating (or failing to activate) TiO_2 under histotripsy exposure. The results of this study also suggest that a deeper exploration of the ultrasonic parameter space (pulse duration, PRF, etc.) should elucidate the optimal insonation parameters for ROS generation and sonodynamic therapy applications. In order to test the utility of histotripsy in sonodynamic therapy more broadly, sonosensitizers of different materials, doping, and dielectric and piezoelectric properties should also be explored.[256, 257, 262] Conjugates of sonosensitizers and cavitation nucleation agents are another promising avenue of improving sonodynamic therapy.[242] Acoustic power measured via PCI has been demonstrated in multiple sections of this dissertation as a useful metric for several cavitation-induced bioeffects. A natural extension of this work could be the evaluation of PCI as an indicator for histotripsy induced lysis, apoptosis, or drug delivery in cancer cells. Interestingly, the goals of this dissertation are being actively explored in combination through recent, promising research on image-guided, nanoparticle-assisted ultrasound therapy and drug delivery for prostate cancer treatment.[230, 265]

This dissertation explored several therapeutic ultrasound applications for treatment of resilient cancerous disease. The results of these studies offer insight into the relevant considerations for improving the efficacy and safety of potential non-invasive therapies. Further investigation of the therapeutic and image guidance modalities presented in this work could lead to the development and clinical translation of novel treatment options for resistant pathologies such as recurrent prostate cancer.

REFERENCES

1 F. Bray, J. Ferlay, I. Soerjomataram, R.L. Siegel, L.A. Torre, and A. Jemal, Global cancer statistics 2018: GLOBOCAN estimates of incidence and mortality worldwide for 36 cancers in 185 countries, CA: A Cancer Journal for Clinicians **68**(6), 394–424 (2018).

2 S.E. Eggener, P.T. Scardino, P.C. Walsh, *et al.*, Predicting 15-Year Prostate Cancer Specific Mortality After Radical Prostatectomy, The Journal of Urology **185**(3), 869–875 (2011).

3 J.E. Sylvester, P.D. Grimm, J.C. Blasko, *et al.*, 15-Year biochemical relapse free survival in clinical Stage T1-T3 prostate cancer following combined external beam radiotherapy and brachytherapy; Seattle experience, International Journal of Radiation Oncology*Biology*Physics **67**(1), 57–64 (2007).

4 L. Klotz, L. Zhang, A. Lam, R. Nam, A. Mamedov, and A. Loblaw, Clinical Results of Long-Term Follow-Up of a Large, Active Surveillance Cohort With Localized Prostate Cancer, JCO **28**(1), 126–131 (2010).

5 R. Zdrojowy, J. Dembowski, B. Małkiewicz, K. Tupikowski, and W. Krajewski, Salvage local therapy for radiation-recurrent prostate cancer – where are we?, Cent European J Urol **69**(3), 264–270 (2016).

6 P.A. Kupelian, A. Mahadevan, C.A. Reddy, A.M. Reuther, and E.A. Klein, Use of different definitions of biochemical failure after external beam radiotherapy changes conclusions about relative treatment efficacy for localized prostate cancer, Urology **68**(3), 593–598 (2006).

7 C.J. Paller and E.S. Antonarakis, Management of Biochemically Recurrent Prostate Cancer After Local Therapy: Evolving Standards of Care and New Directions, Clin Adv Hematol Oncol **11**(1), 14–23 (2013).

8 D.B. Rukstalis, Treatment Options after Failure of Radiation Therapy—A Review, Rev Urol **4**(Suppl 2), S12–S17 (2002).

9 A.M. Autran-Gomez, R.M. Scarpa, and J. Chin, High-Intensity Focused Ultrasound and Cryotherapy as Salvage Treatment in Local Radio-Recurrent Prostate Cancer, UIN **89**(4), 373–379 (2012).

10 F.-J. Murat, L. Poissonnier, M. Rabilloud, *et al.*, Mid-term Results Demonstrate Salvage High-Intensity Focused Ultrasound (HIFU) as an Effective and Acceptably Morbid Salvage Treatment Option for Locally Radiorecurrent Prostate Cancer, European Urology **55**(3), 640–649 (2009).

11 M.G. Sanda, R.L. Dunn, J. Michalski, *et al.*, Quality of Life and Satisfaction with Outcome among Prostate-Cancer Survivors, New England Journal of Medicine **358**(12), 1250–1261 (2008).

12 P.K. Agarwal, N. Sadetsky, B.R. Konety, M.I. Resnick, and P.R. Carroll, Treatment failure after primary and salvage therapy for prostate cancer, Cancer **112**(2), 307–314 (2008).

[13] A. Gelet, J.Y. Chapelon, L. Poissonnier, *et al.*, Local recurrence of prostate cancer after external beam radiotherapy: early experience of salvage therapy using high-intensity focused ultrasonography1, Urology **63**(4), 625–629 (2004).

[14] V.A. Solovov, S.Y. Dvoynikov, and M.O. Vozdvizhenskiy, High-intensity focused ultrasound for the treatment of localized and locally advanced hormone-resistant prostate cancer: 2,5 year outcome, AIP Conference Proceedings **1359**(1), 473–479 (2011).

[15] M.K. Brawer, Radiation Therapy Failure in Prostate Cancer Patients: Risk Factors and Methods of Detection, Rev Urol **4**(Suppl 2), S2–S11 (2002).

[16] A. D'Amico, M. Altschuler, R. Whittington, G. Kao, S.B. Malkowicz, and A. Wein, The use of clinical parameters in an interactive statistical package to predict pathological features associated with local failure after radical prostatectomy for prostate cancer, Clin Perform Qual Health Care **1**(4), 219–222 (1993).

[17] J.F. Langenhuijsen, E.M.P. Broers, and H. Vergunst, Cryosurgery for Prostate Cancer: an Update on Clinical Results of Modern Cryotechnology, European Urology **55**(1), 76–86 (2009).

[18] I.F. Tannock, D. Osoba, M.R. Stockler, *et al.*, Chemotherapy with mitoxantrone plus prednisone or prednisone alone for symptomatic hormone-resistant prostate cancer: a Canadian randomized trial with palliative end points., JCO **14**(6), 1756–1764 (1996).

[19] I.F. Tannock, R. de Wit, W.R. Berry, *et al.*, Docetaxel plus Prednisone or Mitoxantrone plus Prednisone for Advanced Prostate Cancer, New England Journal of Medicine **351**(15), 1502–1512 (2004).

[20] D.P. Petrylak, C.M. Tangen, M.H.A. Hussain, *et al.*, Docetaxel and Estramustine Compared with Mitoxantrone and Prednisone for Advanced Refractory Prostate Cancer, New England Journal of Medicine **351**(15), 1513–1520 (2004).

[21] M.C. Markowski and M.A. Carducci, Early use of chemotherapy in metastatic prostate cancer, Cancer Treatment Reviews **55**, 218–224 (2017).

[22] J. Kroon, J.M. Metselaar, G. Storm, and G. van der Pluijm, Liposomal nanomedicines in the treatment of prostate cancer, Cancer Treatment Reviews **40**(4), 578–584 (2014).

[23] Y. (Chezy) Barenholz, Doxil® — The first FDA-approved nano-drug: Lessons learned, Journal of Controlled Release **160**(2), 117–134 (2012).

[24] U. Bulbake, S. Doppalapudi, N. Kommineni, and W. Khan, Liposomal Formulations in Clinical Use: An Updated Review, Pharmaceutics **9**(2), (2017).

[25] S. Shen, H. Tang, X. Zhang, *et al.*, Targeting mesoporous silica-encapsulated gold nanorods for chemo-photothermal therapy with near-infrared radiation, Biomaterials **34**(12), 3150–3158 (2013).

[26] M. Zheng, C. Yue, Y. Ma, *et al.*, Single-Step Assembly of DOX/ICG Loaded Lipid–Polymer Nanoparticles for Highly Effective Chemo-photothermal Combination Therapy, ACS Nano **7**(3), 2056–2067 (2013).

[27] T.-Y. Kim, D.-W. Kim, J.-Y. Chung, *et al.*, Phase I and Pharmacokinetic Study of Genexol-PM, a Cremophor-Free, Polymeric Micelle-Formulated Paclitaxel, in Patients with Advanced Malignancies, Clin Cancer Res **10**(11), 3708–3716 (2004).

[28] Y.H. Bae, Drug targeting and tumor heterogeneity, J Control Release **133**(1), 2–3 (2009).

[29] C. de L. Davies, L.M. Lundstrøm, J. Frengen, *et al.*, Radiation improves the distribution and uptake of liposomal doxorubicin (caelyx) in human osteosarcoma xenografts, Cancer Res. **64**(2), 547–553 (2004).

[30] D. >Gail ter Haar and C. Coussios, High intensity focused ultrasound: Physical principles and devices, International Journal of Hyperthermia **23**(2), 89–104 (2007).

[31] C.G. Chaussy and S. Thüroff, High-Intensity Focused Ultrasound for the Treatment of Prostate Cancer: A Review, Journal of Endourology **31**(S1), S-30 (2017).

[32] J.E. Kennedy, F. Wu, G.R. ter Haar, *et al.*, High-intensity focused ultrasound for the treatment of liver tumours, Ultrasonics **42**(1), 931–935 (2004).

[33] J.E. Kennedy, High-intensity focused ultrasound in the treatment of solid tumours, Nat. Rev. Cancer **5**(4), 321–327 (2005).

[34] V. Rieke and K.B. Pauly, MR Thermometry, J Magn Reson Imaging **27**(2), 376–390 (2008).

[35] M. Burtnyk, T. Hill, H. Cadieux-Pitre, and I. Welch, Magnetic Resonance Image Guided Transurethral Ultrasound Prostate Ablation: A Preclinical Safety and Feasibility Study with 28-Day Followup, The Journal of Urology **193**(5), 1669–1675 (2015).

[36] J.L. Chin, M. Billia, J. Relle, *et al.*, Magnetic Resonance Imaging–Guided Transurethral Ultrasound Ablation of Prostate Tissue in Patients with Localized Prostate Cancer: A Prospective Phase 1 Clinical Trial, European Urology **70**(3), 447–455 (2016).

[37] J.-J. Li, M.-F. Gu, G.-Y. Luo, L.-Z. Liu, R. Zhang, and G.-L. Xu, Complications of high intensity focused ultrasound for patients with hepatocellular carcinoma, Technol. Cancer Res. Treat. **8**(3), 217–224 (2009).

[38] S.A. Curley, Radiofrequency Ablation of Malignant Liver Tumors, The Oncologist **6**(1), 14–23 (2001).

[39] D.S.K. Lu, S.S. Raman, P. Limanond, *et al.*, Influence of Large Peritumoral Vessels on Outcome of Radiofrequency Ablation of Liver Tumors, Journal of Vascular and Interventional Radiology **14**(10), 1267–1274 (2003).

[40] J.E. Parsons, C.A. Cain, G.D. Abrams, and J.B. Fowlkes, Pulsed cavitational ultrasound therapy for controlled tissue homogenization, Ultrasound Med Biol **32**(1), 115–129 (2006).

[41] W.W. Roberts, T.L. Hall, K. Ives, J.S. Wolf, J.B. Fowlkes, and C.A. Cain, Pulsed cavitational ultrasound: a noninvasive technology for controlled tissue ablation (histotripsy) in the rabbit kidney, J. Urol. **175**(2), 734–738 (2006).

[42] E. Vlaisavljevich, A. Maxwell, L. Mancia, E. Johnsen, C. Cain, and Z. Xu, Visualizing the Histotripsy Process: Bubble Cloud–Cancer Cell Interactions in a Tissue-Mimicking Environment, Ultrasound in Medicine & Biology **42**(10), 2466–2477 (2016).

[43] A. Maxwell, O. Sapozhnikov, M. Bailey, *et al.*, Disintegration of Tissue Using High Intensity Focused Ultrasound: Two Approaches That Utilize Shock Waves, Acoustics Today **8**(4), 24–37 (2012).

[44] V. Khokhlova, J. Fowlkes, W. Roberts, *et al.*, Histotripsy Methods in Mechanical Disintegration of Tissue: Toward Clinical Applications, Int J Hyperthermia **31**(2), 145–162 (2015).

[45] K.B. Bader and C.K. Holland, Predicting the growth of nanoscale nuclei by histotripsy pulses, Phys Med Biol **61**(7), 2947–2966 (2016).

[46] A.D. Maxwell, T.-Y. Wang, C.A. Cain, *et al.*, Cavitation clouds created by shock scattering from bubbles during histotripsy, J Acoust Soc Am **130**(4), 1888–1898 (2011).

[47] K.B. Bader, K.J. Haworth, A.D. Maxwell, and C.K. Holland, Post Hoc Analysis of Passive Cavitation Imaging for Classification of Histotripsy-Induced Liquefaction in Vitro, IEEE Trans Med Imaging **37**(1), 106–115 (2018).

[48] T.Y. Wang, Z. Xu, F. Winterroth, *et al.*, Quantitative ultrasound backscatter for pulsed cavitational ultrasound therapy-histotripsy, IEEE Transactions on Ultrasonics, Ferroelectrics, and Frequency Control **56**(5), 995–1005 (2009).

[49] T.L. Hall, J.B. Fowlkes, and C.A. Cain, Imaging feedback of tissue liquefaction (histotripsy) in ultrasound surgery, in *IEEE Ultrasonics Symposium, 2005.*(2005), pp. 1732–1734.

[50] K.J. Haworth, K.B. Bader, K.T. Rich, C.K. Holland, and T.D. Mast, Quantitative Frequency-Domain Passive Cavitation Imaging, IEEE Transactions on Ultrasonics, Ferroelectrics, and Frequency Control **64**(1), 177–191 (2017).

[51] K.B. Bader, Comparison of passive cavitation imaging and plane wave B-mode imaging for monitoring histotripsy ablation, The Journal of the Acoustical Society of America **140**(4), 3084–3084 (2016).

[52] S.P. Allen, E. Vlaisavljevich, J. Shi, *et al.*, The response of MRI contrast parameters in in vitro tissues and tissue mimicking phantoms to fractionation by histotripsy, Phys. Med. Biol. **62**(17), 7167 (2017).

[53] Y. Kim, C.G. Fifer, S.K. Gelehrter, *et al.*, Developmental Impact and Lesion Maturation of Histotripsy-Mediated Non-Invasive Tissue Ablation in a Fetal Sheep Model, Ultrasound in Medicine and Biology **39**(6), 1047–1055 (2013).

[54] Y. Kim, E. Vlaisavljevich, G.E. Owens, S.P. Allen, C.A. Cain, and Z. Xu, In vivo transcostal histotripsy therapy without aberration correction, Phys. Med. Biol. **59**(11), 2553 (2014).

[55] E. Vlaisavljevich, Y. Kim, G. Owens, W. Roberts, C. Cain, and Z. Xu, Effects of Tissue Mechanical Properties on Susceptibility to Histotripsy-induced Tissue Damage, Phys Med Biol **59**(2), 253–270 (2014).

[56] A. Eranki, N. Farr, A. Partanen, *et al.*, Boiling histotripsy lesion characterization on a clinical magnetic resonance imaging-guided high intensity focused ultrasound system, PLOS ONE **12**(3), e0173867 (2017).

[57] M. Lafond, S. Yoshizawa, and S. Umemura, Sonodynamic Therapy: Advances and Challenges in Clinical Translation, Journal of Ultrasound in Medicine **38**(3), 567–580 (2019).

[58] R.E. Apfel, 7. Acoustic Cavitation, in *Methods in Experimental Physics*, edited by P.D. Edmonds (Academic Press, 1981), pp. 355–411.

[59] R.E. Apfel and C.K. Holland, Gauging the likelihood of cavitation from short-pulse, low-duty cycle diagnostic ultrasound, Ultrasound in Medicine & Biology **17**(2), 179–185 (1991).

[60] N. Yumita, K. Sasaki, S. Umemura, and R. Nishigaki, Sonodynamically induced antitumor effect of a gallium-porphyrin complex, ATX-70, Jpn. J. Cancer Res. **87**(3), 310–316 (1996).

[61] N. Yumita, N. Okuyama, K. Sasaki, and S.-I. Umemura, Sonodynamic therapy on chemically induced mammary tumor: pharmacokinetics, tissue distribution and sonodynamically induced antitumor effect of gallium-porphyrin complex ATX-70, Cancer Chemother. Pharmacol. **60**(6), 891–897 (2007).

[62] Y. Shimamura, D. Tamatani, S. Kuniyasu, *et al.*, 5-Aminolevulinic Acid Enhances Ultrasound-mediated Antitumor Activity via Mitochondrial Oxidative Damage in Breast Cancer, Anticancer Res. **36**(7), 3607–3612 (2016).

[63] N. Nomikou, C. Fowley, N.M. Byrne, B. McCaughan, A.P. McHale, and J.F. Callan, Microbubble-sonosensitiser conjugates as therapeutics in sonodynamic therapy, Chem. Commun. (Camb.) **48**(67), 8332–8334 (2012).

[64] C. Zini, E. Hipp, S. Thomas, A. Napoli, C. Catalano, and A. Oto, Ultrasound- and MR-guided focused ultrasound surgery for prostate cancer, World J Radiol **4**(6), 247–252 (2012).

[65] H. Lukka, T. Waldron, J. Chin, *et al.*, High-intensity Focused Ultrasound for Prostate Cancer: a Systematic Review, Clinical Oncology **23**(2), 117–127 (2011).

[66] R. Chopra, A. Colquhoun, M. Burtnyk, *et al.*, MR Imaging–controlled Transurethral Ultrasound Therapy for Conformal Treatment of Prostate Tissue: Initial Feasibility in Humans, Radiology **265**(1), 303–313 (2012).

[67] A.A. Schulman, K.J. Tay, C.N. Robertson, and T.J. Polascik, High-intensity focused ultrasound for focal therapy: reality or pitfall?, Current Opinion in Urology **27**(2), 138–148 (2017).

[68] A. Partanen, N.K. Yerram, H. Trivedi, *et al.*, Magnetic resonance imaging (MRI)-guided transurethral ultrasound therapy of the prostate: a preclinical study with radiological and pathological correlation using customised MRI-based moulds, BJU Int. **112**(4), 508–516 (2013).

[69] S. Sammet, A. Partanen, A. Yousuf, *et al.*, Cavernosal nerve functionality evaluation after magnetic resonance imaging-guided transurethral ultrasound treatment of the prostate, World J Radiol **7**(12), 521–530 (2015).

[70] Eggener* Scott, Penson David, Pavlovich Christian, *et al.*, Lba-26 pivotal trial of mri-guided transurethral ultrasound ablation in men with localized prostate cancer, Journal of Urology **201**(Supplement 4), e1004–e1004 (2019).

[71] C.-H. Wang, S.-T. Kang, Y.-H. Lee, Y.-L. Luo, Y.-F. Huang, and C.-K. Yeh, Aptamer-conjugated and drug-loaded acoustic droplets for ultrasound theranosis, Biomaterials **33**(6), 1939–1947 (2012).

[72] J.S. Arora, H.Y. Murad, S. Ashe, *et al.*, Ablative Focused Ultrasound Synergistically Enhances Thermally Triggered Chemotherapy for Prostate Cancer in Vitro, Mol. Pharmaceutics **13**(9), 3080–3090 (2016).

[73] A.M. Ponce, B.L. Viglianti, D. Yu, *et al.*, Magnetic resonance imaging of temperature-sensitive liposome release: drug dose painting and antitumor effects, J. Natl. Cancer Inst. **99**(1), 53–63 (2007).

[74] Z.S. Al-Ahmady, C.L. Scudamore, and K. Kostarelos, Triggered doxorubicin release in solid tumors from thermosensitive liposome-peptide hybrids: Critical parameters and therapeutic efficacy, Int. J. Cancer **137**(3), 731–743 (2015).

[75] T. Ta, E. Bartolak-Suki, E.-J. Park, K. Karrobi, N.J. McDannold, and T.M. Porter, Localized delivery of doxorubicin in vivo from polymer-modified thermosensitive liposomes with MR-guided focused ultrasound-mediated heating, Journal of Controlled Release **194**, 71–81 (2014).

[76] L.C. Chiu, S.K. Wu, W.L. Lin, and G.S. Chen, Synergistic Effects of Nanodrug, Ultrasound Hyperthermia, and Thermal Ablation on Solid Tumors #8212;An Animal Study, IEEE Transactions on Biomedical Engineering **64**(12), 2880–2889 (2017).

[77] A. Liberman, N. Mendez, W.C. Trogler, and A.C. Kummel, Synthesis and surface functionalization of silica nanoparticles for nanomedicine, Surf Sci Rep **69**(2–3), 132–158 (2014).

[78] A. Liberman, Z. Wu, C.V. Barback, *et al.*, Hollow iron-silica nanoshells for enhanced high intensity focused ultrasound, J. Surg. Res. **190**(2), 391–398 (2014).

[79] Y. Chen, H. Chen, Y. Sun, *et al.*, Multifunctional Mesoporous Composite Nanocapsules for Highly Efficient MRI-Guided High-Intensity Focused Ultrasound Cancer Surgery, Angew. Chem. Int. Ed. **50**(52), 12505–12509 (2011).

[80] X. Wang, H. Chen, Y. Chen, *et al.*, Perfluorohexane-Encapsulated Mesoporous Silica Nanocapsules as Enhancement Agents for Highly Efficient High Intensity Focused Ultrasound (HIFU), Adv. Mater. **24**(6), 785–791 (2012).

[81] J. Wang, C.V. Barback, C.N. Ta, *et al.*, Extended Lifetime In Vivo Pulse Stimulated Ultrasound Imaging, IEEE Transactions on Medical Imaging **37**(1), 222–229 (2018).

[82] G.J. Anthony, K.B. Bader, J. Wang, *et al.*, MRI-guided transurethral insonation of silica-shell phase-shift emulsions in the prostate with an advanced navigation platform, Med Phys **46**(2), 774–788 (2019).

[83] L. Winter, E. Oberacker, K. Paul, *et al.*, Magnetic resonance thermometry: Methodology, pitfalls and practical solutions, International Journal of Hyperthermia **32**(1), 63–75 (2016).

[84] J.D. Hazle, C.J. Diederich, M. Kangasniemi, R.E. Price, L.E. Olsson, and R.J. Stafford, MRI-guided thermal therapy of transplanted tumors in the canine prostate using a directional transurethral ultrasound applicator, J. Magn. Reson. Imaging **15**(4), 409–417 (2002).

[85] N. McDannold, K. Hynynen, D. Wolf, G. Wolf, and F. Jolesz, MRI evaluation of thermal ablation of tumors with focused ultrasound, J. Magn. Reson. Imaging **8**(1), 91–100 (1998).

[86] J.W. Wijlemans, R. Deckers, M.A. a j van den Bosch, *et al.*, Evolution of the Ablation Region After Magnetic Resonance–Guided High-Intensity Focused Ultrasound Ablation in a Vx2 Tumor Model, Investigative Radiology **48**(6), 381–386 (2013).

[87] I. Jacobs, S.J.C.G. Hectors, M.C. Schabel, H. Grüll, G.J. Strijkers, and K. Nicolay, Cluster analysis of DCE-MRI data identifies regional tracer-kinetic changes after tumor treatment with high intensity focused ultrasound, NMR Biomed. **28**(11), 1443–1454 (2015).

[88] D. Gianfelice, A. Khiat, M. Amara, A. Belblidia, and Y. Boulanger, MR Imaging-guided Focused Ultrasound Surgery of Breast Cancer: Correlation of Dynamic Contrast-enhanced MRI with Histopathologic Findings, Breast Cancer Res Treat **82**(2), 93–101 (2003).

[89] A. Khiat, D. Gianfelice, M. Amara, and Y. Boulanger, Influence of post-treatment delay on the evaluation of the response to focused ultrasound surgery of breast cancer by dynamic contrast enhanced MRI, BJR **79**(940), 308–314 (2006).

[90] A. Liberman, Z. Wu, C.V. Barback, *et al.*, Color Doppler Ultrasound and Gamma Imaging of Intratumorally Injected 500 nm Iron–Silica Nanoshells, ACS Nano **7**(7), 6367–6377 (2013).

[91] C.N. Ta, A. Liberman, H. Paul Martinez, *et al.*, Integrated processing of contrast pulse sequencing ultrasound imaging for enhanced active contrast of hollow gas filled silica nanoshells and microshells, J Vac Sci Technol B Nanotechnol Microelectron **30**(2), (2012).

[92] A. Liberman, H.P. Martinez, C.N. Ta, *et al.*, Hollow silica and silica-boron nano/microparticles for contrast-enhanced ultrasound to detect small tumors, Biomaterials **33**(20), 5124–5129 (2012).

[93] J.A. Feshitan, F. Vlachos, S.R. Sirsi, E.E. Konofagou, and M.A. Borden, Theranostic Gd(III)-lipid microbubbles for MRI-guided focused ultrasound surgery, Biomaterials **33**(1), 247–255 (2012).

[94] J. Huang, J.S. Xu, and R.X. Xu, Heat-sensitive microbubbles for intraoperative assessment of cancer ablation margins, Biomaterials **31**(6), 1278–1286 (2010).

[95] T.L. Hall, C.R. Hempel, A.M. Lake, *et al.*, Histotripsy for the treatment of BPH: evaluation in a chronic canine model, in *2008 IEEE Ultrasonics Symposium*(2008), pp. 765–767.

[96] N. Styn, T.L. Hall, J.B. Fowlkes, C.A. Cain, and W.W. Roberts, Histotripsy Homogenization of the Prostate: Thresholds for Cavitation Damage of Periprostatic Structures, J Endourol **25**(9), 1531–1535 (2011).

[97] S.E. Darnell, T.L. Hall, S.A. Tomlins, X. Cheng, K.A. Ives, and W.W. Roberts, Histotripsy of the Prostate in a Canine Model: Characterization of Post-Therapy Inflammation and Fibrosis, J Endourol **29**(7), 810–815 (2015).

[98] T.L. Hall, C.R. Hempel, K. Wojno, Z. Xu, C.A. Cain, and W.W. Roberts, Histotripsy of the Prostate: Dose Effects in a Chronic Canine Model, Urology **74**(4), 932–937 (2009).

[99] A.M. Lake, T.L. Hall, K. Kieran, J.B. Fowlkes, C.A. Cain, and W.W. Roberts, Histotripsy: Minimally Invasive Technology for Prostatic Tissue Ablation in an In Vivo Canine Model, Urology **72**(3), 682–686 (2008).

[100] J.C. Wheat, T.L. Hall, C.R. Hempel, C.A. Cain, Z. Xu, and W.W. Roberts, Prostate Histotripsy in an Anticoagulated Model, Urology **75**(1), 207–211 (2010).

[101] G.R. Schade, J. Keller, K. Ives, *et al.*, Histotripsy Focal Ablation of Implanted Prostate Tumor in an ACE-1 Canine Cancer Model, The Journal of Urology **188**(5), 1957–1964 (2012).

[102] R. Boutier, N. Girouin, A.B. Cheikh, *et al.*, Location of residual cancer after transrectal high-intensity focused ultrasound ablation for clinically localized prostate cancer, BJU International **108**(11), 1776–1781 (2011).

[103] L. Poissonnier, J.-Y. Chapelon, O. Rouvière, *et al.*, Control of Prostate Cancer by Transrectal HIFU in 227 Patients, European Urology **51**(2), 381–387 (2007).

[104] E. Hagtvet, K. Røe, and D.R. Olsen, Liposomal doxorubicin improves radiotherapy response in hypoxic prostate cancer xenografts, Radiation Oncology **6**, 135 (2011).

[105] S. Eggen, M. Afadzi, E.A. Nilssen, S.B. Haugstad, B. Angelsen, and C. de L. Davies, Ultrasound Improves the Uptake and Distribution of Liposomal Doxorubicin in Prostate Cancer Xenografts, Ultrasound in Medicine & Biology **39**(7), 1255–1266 (2013).

[106] A.D. Maxwell, S. Park, B.L. Vaughan, C.A. Cain, J.B. Grotberg, and Z. Xu, Trapping of embolic particles in a vessel phantom by cavitation-enhanced acoustic streaming, Phys. Med. Biol. **59**(17), 4927 (2014).

[107] C.C. Coussios and R.A. Roy, Applications of Acoustics and Cavitation to Noninvasive Therapy and Drug Delivery, Annual Review of Fluid Mechanics **40**(1), 395–420 (2008).

[108] S. Datta, C.-C. Coussios, A.Y. Ammi, T.D. Mast, G.M. de Courten-Myers, and C.K. Holland, Ultrasound-Enhanced Thrombolysis Using Definity® as a Cavitation Nucleation Agent, Ultrasound in Medicine & Biology **34**(9), 1421–1433 (2008).

[109] K.B. Bader, M.J. Gruber, and C.K. Holland, Shaken and Stirred: Mechanisms of Ultrasound-Enhanced Thrombolysis, Ultrasound in Medicine & Biology **41**(1), 187–196 (2015).

[110] M. Gyöngy and C.C. Coussios, Passive Spatial Mapping of Inertial Cavitation During HIFU Exposure, IEEE Transactions on Biomedical Engineering **57**(1), 48–56 (2010).

[111] C. Arvanitis, C. Crake, N. McDannold, and G. Clement, Passive Acoustic Mapping with the Angular Spectrum Method, IEEE Transactions on Medical Imaging **PP**(99), 1–1 (2017).

[112] L. Somaglino, G. Bouchoux, J.-L. Mestas, and C. Lafon, Validation of an acoustic cavitation dose with hydroxyl radical production generated by inertial cavitation in pulsed mode: Application to in vitro drug release from liposomes, Ultrasonics Sonochemistry **18**(2), 577–588 (2011).

[113] S.A. Rosenthal, D. Hunt, A.O. Sartor, *et al.*, A Phase 3 Trial of 2 Years of Androgen Suppression and Radiation Therapy With or Without Adjuvant Chemotherapy for High-Risk Prostate Cancer: Final Results of Radiation Therapy Oncology Group Phase 3 Randomized Trial NRG Oncology RTOG 9902, International Journal of Radiation Oncology*Biology*Physics **93**(2), 294–302 (2015).

[114] A. Hubert, O. Lyass, D. Pode, and A. Gabizon, Doxil (caelyx): an exploratory study with pharmacokinetics in patients with hormone-refractory prostate cancer, Anti-cancer Drugs **11**(2), 123–127 (2000).

[115] X. Wang, H. Chen, Y. Zheng, *et al.*, Au-nanoparticle coated mesoporous silica nanocapsule-based multifunctional platform for ultrasound mediated imaging, cytoclasis and tumor ablation, Biomaterials **34**(8), 2057–2068 (2013).

[116] K.J. Haworth, P. Arunkumar, B.H. Goldstein, *et al.*, Dissolved oxygen scavenging by acoustic droplet vaporization using intravascular ultrasound, in *2017 IEEE International Ultrasonics Symposium (IUS)*(2017), pp. 1–4.

[117] R. Chopra, K. Tang, M. Burtnyk, *et al.*, Analysis of the spatial and temporal accuracy of heating in the prostate gland using transurethral ultrasound therapy and active MR temperature feedback, Phys. Med. Biol. **54**(9), 2615 (2009).

[118] A. Boyes, K. Tang, M. Yaffe, L. Sugar, R. Chopra, and M. Bronskill, Prostate Tissue Analysis Immediately Following Magnetic Resonance Imaging Guided Transurethral Ultrasound Thermal Therapy, The Journal of Urology **178**(3), 1080–1085 (2007).

[119] R.L. Siegel, K.D. Miller, and A. Jemal, Cancer statistics, 2019, CA: A Cancer Journal for Clinicians **69**(1), 7–34 (2019).

[120] M.R. Cooperberg, D.P. Lubeck, M.V. Meng, S.S. Mehta, and P.R. Carroll, The Changing Face of Low-risk Prostate Cancer: Trends in Clinical Presentation and Primary Management, J Clin Oncol **22**(11), 2141–2149 (2004).

[121] J.J. Tosoian, H.B. Carter, A. Lepor, and S. Loeb, Active surveillance for prostate cancer: current evidence and contemporary state of practice, Nat Rev Urol **13**(4), 205–215 (2016).

[122] M.J. Resnick, T. Koyama, K.-H. Fan, *et al.*, Long-Term Functional Outcomes after Treatment for Localized Prostate Cancer, New England Journal of Medicine **368**(5), 436–445 (2013).

[123] J.L. Chin, J. Relle, M. Dewar, *et al.*, MP30-03 MRI-GUIDED TRANSURETHRAL ULTRASOUND ABLATION IN PATIENTS WITH LOCALIZED PROSTATE CANCER: 3-YEAR OUTCOMES OF A PROSPECTIVE PHASE I STUDY, The Journal of Urology **199**(4, Supplement), e375 (2018).

[124] Y.-F. Zhou, High intensity focused ultrasound in clinical tumor ablation, World J Clin Oncol **2**(1), 8–27 (2011).

[125] E. Vlaisavljevich, J. Greve, X. Cheng, *et al.*, Non-Invasive Ultrasound Liver Ablation Using Histotripsy: Chronic Study in an In Vivo Rodent Model, Ultrasound in Medicine & Biology **42**(8), 1890–1902 (2016).

[126] A. Liberman, J. Wang, N. Lu, *et al.*, Mechanically Tunable Hollow Silica Ultrathin Nanoshells for Ultrasound Contrast Agents, Adv. Funct. Mater. **25**(26), 4049–4057 (2015).

[127] R.G. Holt and R.A. Roy, Measurements of bubble-enhanced heating from focused, mhz-frequency ultrasound in a tissue-mimicking material, Ultrasound in Medicine & Biology **27**(10), 1399–1412 (2001).

[128] J.A. Kopechek, E. Park, C.-S. Mei, N.J. McDannold, and T.M. Porter, Accumulation of Phase-Shift Nanoemulsions to Enhance MR-Guided Ultrasound-Mediated Tumor Ablation In Vivo, J Healthc Eng **4**(1), 109–126 (2013).

[129] X. Fan, C.R. Haney, G. Agrawal, *et al.*, High-resolution MRI of excised human prostate specimens acquired with 9.4T in detection and identification of cancers: Validation of a technique, J. Magn. Reson. Imaging **34**(4), 956–961 (2011).

[130] R. Bazzi, M.A. Flores-Gonzalez, C. Louis, *et al.*, Synthesis and luminescent properties of sub-5-nm lanthanide oxides nanoparticles, Journal of Luminescence **102**, 445–450 (2003).

[131] A.P. Crawley and R.M. Henkelman, A comparison of one-shot and recovery methods in T1 imaging, Magn Reson Med **7**(1), 23–34 (1988).

[132] E.L. Hahn, Spin Echoes, Phys. Rev. **80**(4), 580–594 (1950).

[133] N. Stikov, C. Tardif, J.K. Barral, I. Levesque, and G.B. Pike, T1 mapping: Methods and challenges, in *19th Scientific Meeting of the International Society for Magnetic Resonance in Medicine*(2011).

[134] A.R. Padhani, C.J. Gapinski, D.A. Macvicar, *et al.*, Dynamic Contrast Enhanced MRI of Prostate Cancer: Correlation with Morphology and Tumour Stage, Histological Grade and PSA, Clinical Radiology **55**(2), 99–109 (2000).

[135] S.A. Sapareto and W.C. Dewey, Thermal dose determination in cancer therapy, Int. J. Radiat. Oncol. Biol. Phys. **10**(6), 787–800 (1984).

[136] F.L. Goerner and G.D. Clarke, Measuring signal-to-noise ratio in partially parallel imaging MRI, Med Phys **38**(9), 5049–5057 (2011).

[137] E.O. Stejskal and J.E. Tanner, Spin Diffusion Measurements: Spin Echoes in the Presence of a Time-Dependent Field Gradient, The Journal of Chemical Physics **42**(1), 288–292 (1965).

[138] W.C. Dewey, Arrhenius relationships from the molecule and cell to the clinic, International Journal of Hyperthermia **25**(1), 3–20 (2009).

[139] K.B. Pauly, C.J. Diederich, V. Rieke, *et al.*, Magnetic Resonance-guided High-intensity Ultrasound Ablation of the Prostate, Topics in Magnetic Resonance Imaging **17**(3), 195–207 (2006).

[140] V.V. Volkov and Y. Zhu, Deterministic phase unwrapping in the presence of noise, Opt. Lett., OL **28**(22), 2156–2158 (2003).

[141] F.M. Fennessy, A. Fedorov, S.N. Gupta, E.J. Schmidt, C.M. Tempany, and R.V. Mulkern, QIN: Practical Considerations in T1 Mapping of Prostate for Dynamic Contrast Enhancement Pharmacokinetic Analyses, Magn Reson Imaging **30**(9), 1224–1233 (2012).

[142] G.P. Liney, A.J. Knowles, D.J. Manton, L.W. Turnbull, S.J. Blackband, and A. Horsman, Comparison of conventional single echo and multi-echo sequences with a fast spin-echo sequence for quantitative T2 mapping: Application to the prostate, Journal of Magnetic Resonance Imaging **6**(4), 603–607 (n.d.).

[143] J.E. Coad, K. Kosari, A. Humar, and T.D. Sielaff, Radiofrequency ablation causes ‘thermal fixation’ of hepatocellular carcinoma: a post-liver transplant histopathologic study, Clinical Transplantation **17**(4), 377–384 (2003).

[144] X. He, S. McGee, J.E. Coad, *et al.*, Investigation of the thermal and tissue injury behaviour in microwave thermal therapy using a porcine kidney model, International Journal of Hyperthermia **20**(6), 567–593 (2004).

[145] O.D. Kripfgans, J.B. Fowlkes, D.L. Miller, O.P. Eldevik, and P.L. Carson, Acoustic droplet vaporization for therapeutic and diagnostic applications, Ultrasound in Medicine & Biology **26**(7), 1177–1189 (2000).

[146] J.Y. Park, M.J. Baek, E.S. Choi, *et al.*, Paramagnetic Ultrasmall Gadolinium Oxide Nanoparticles as Advanced T1 MRI Contrast Agent: Account for Large Longitudinal Relaxivity, Optimal Particle Diameter, and In Vivo T1 MR Images, ACS Nano **3**(11), 3663–3669 (2009).

[147] A.T.M. Anishur Rahman, P. Majewski, and K. Vasilev, Gd2O3 nanoparticles: size-dependent nuclear magnetic resonance, Contrast Media Mol. Imaging **8**(1), 92–95 (2013).

[148] M. Ahrén, L. Selegård, A. Klasson, *et al.*, Synthesis and Characterization of PEGylated Gd2O3 Nanoparticles for MRI Contrast Enhancement, Langmuir **26**(8), 5753–5762 (2010).

[149] R.M. Weisskoff, C.S. Zuo, J.L. Boxerman, and B.R. Rosen, Microscopic susceptibility variation and transverse relaxation: theory and experiment, Magn Reson Med **31**(6), 601–610 (1994).

[150] R.P. Kennan, J. Zhong, and J.C. Gore, Intravascular susceptibility contrast mechanisms in tissues, Magn Reson Med **31**(1), 9–21 (1994).

[151] H. Alavi Tamaddoni, W.W. Roberts, A.P. Duryea, C.A. Cain, and T.L. Hall, Enhanced High-Rate Shockwave Lithotripsy Stone Comminution in an In Vivo Porcine Model Using Acoustic Bubble Coalescence, Journal of Endourology **30**(12), 1321–1325 (2016).

[152] C. Acconcia, B.Y.C. Leung, K. Hynynen, and D.E. Goertz, Interactions between ultrasound stimulated microbubbles and fibrin clots, Appl. Phys. Lett. **103**(5), 053701 (2013).

[153] P.A. Dayton, K.E. Morgan, A.L. Klibanov, G.H. Brandenburger, and K.W. Ferrara, Optical and acoustical observations of the effects of ultrasound on contrast agents, IEEE Transactions on Ultrasonics, Ferroelectrics, and Frequency Control **46**(1), 220–232 (1999).

[154] K.B. Bader and C.K. Holland, Gauging the likelihood of stable cavitation from ultrasound contrast agents, Phys. Med. Biol. **58**(1), 127 (2013).

[155] K.B. Bader, J. Mobley, C.C. Church, and D.F. Gaitan, The effect of static pressure on the strength of inertial cavitation events, The Journal of the Acoustical Society of America **132**(4), 2286–2291 (2012).

[156] K. Radhakrishnan, K.B. Bader, K.J. Haworth, *et al.*, Relationship between cavitation and loss of echogenicity from ultrasound contrast agents, Phys. Med. Biol. **58**(18), 6541 (2013).

[157] K.E. Hitchcock, N.M. Ivancevich, K.J. Haworth, *et al.*, ULTRASOUND-ENHANCED rt-PA THROMBOLYSIS IN AN EX VIVO PORCINE CAROTID ARTERY MODEL, Ultrasound Med Biol **37**(8), 1240–1251 (2011).

[158] U. Lindner, N. Lawrentschuk, R.A. Weersink, *et al.*, Focal Laser Ablation for Prostate Cancer Followed by Radical Prostatectomy: Validation of Focal Therapy and Imaging Accuracy, European Urology **57**(6), 1111–1114 (2010).

[159] J.M. Kelly, A. Amor-Coarasa, A. Nikolopoulou, *et al.*, Dual-Target Binding Ligands with Modulated Pharmacokinetics for Endoradiotherapy of Prostate Cancer, J Nucl Med **58**(9), 1442–1449 (2017).

[160] P. Zhang and T. Porter, An in vitro Study of a Phase-Shift Nanoemulsion: A Potential Nucleation Agent for Bubble-Enhanced HIFU Tumor Ablation, Ultrasound in Medicine & Biology **36**(11), 1856–1866 (2010).

[161] J. Gateau, J.F. Aubry, M. Pernot, M. Fink, and M. Tanter, Combined passive detection and ultrafast active imaging of cavitation events induced by short pulses of high-intensity ultrasound, IEEE Transactions on Ultrasonics, Ferroelectrics, and Frequency Control **58**(3), 517–532 (2011).

[162] H. Hu, S. Xu, Y. Yuan, R. Liu, S. Wang, and M. Wan, Spatial-temporal ultrasound imaging of residual cavitation bubbles around a fluid–tissue interface in histotripsy, The Journal of the Acoustical Society of America **137**(5), 2563–2572 (2015).

[163] B. Arnal, J. Baranger, C. Demene, M. Tanter, and M. Pernot, In vivo real-time cavitation imaging in moving organs, Phys. Med. Biol. **62**(3), 843 (2017).

[164] X. Zhang, R.M. Miller, K.-W. Lin, *et al.*, Real-Time Feedback of Histotripsy Thrombolysis Using Bubble-Induced Color Doppler, Ultrasound in Medicine & Biology **41**(5), 1386–1401 (2015).

[165] R.M. Miller, X. Zhang, A. Maxwell, C. Cain, and Z. Xu, Bubble-induced Color Doppler Feedback for Histotripsy Tissue Fractionation, IEEE Trans Ultrason Ferroelectr Freq Control **63**(3), 408–419 (2016).

[166] J. Chen, B.L. Daniel, C.J. Diederich, *et al.*, Monitoring prostate thermal therapy with diffusion-weighted MRI, Magn. Reson. Med. **59**(6), 1365–1372 (2008).

[167] G.J.L.H. Van Leenders, H. Beerlage, E. Ruijter, J.J.M.C.H. de la Rosette, and C.A. van de Kaa, Histopathological changes associated with high intensity focused ultrasound (HIFU) treatment for localised adenocarcinoma of the prostate, J Clin Pathol **53**(5), 391–394 (2000).

[168] A.M. Kinsey, C.J. Diederich, V. Rieke, *et al.*, Transurethral ultrasound applicators with dynamic multi-sector control for prostate thermal therapy: In vivo evaluation under MR guidance, Med. Phys. **35**(5), 2081–2093 (2008).

[169] N.M. Hijnen, A. Elevelt, J. Pikkemaat, C. Bos, L.W. Bartels, and H. Grüll, The magnetic susceptibility effect of gadolinium-based contrast agents on PRFS-based MR thermometry during thermal interventions, J Ther Ultrasound **1**, 8 (2013).

[170] M. Zhu, Z. Sun, and C.K. Ng, Image-guided thermal ablation with MR-based thermometry, Quantitative Imaging in Medicine and Surgery **7**(3), 356-368–368 (2017).

[171] W.A. N'Djin, C. Mougenot, I. Kobelevskiy, E. Ramsay, M. Bronskill, and R. Chopra, Dual-frequency ultrasound focal therapy for MRI-guided transurethral treatment of the prostate: Study in gel phantom, AIP Conference Proceedings **1503**(1), 212–216 (2012).

[172] W.A. N'Djin, M. Burtnyk, I. Kobelevskiy, S. Hadjis, M. Bronskill, and R. Chopra, Coagulation of human prostate volumes with MRI-controlled transurethral ultrasound therapy: Results in gel phantoms, Med Phys **39**(7), 4524–4536 (2012).

[173] W.A. N'djin, M. Burtnyk, M. Bronskill, and R. Chopra, Investigation of power and frequency for 3D conformal MRI-controlled transurethral ultrasound therapy with a dual frequency multi-element transducer, International Journal Of Hyperthermia: The Official Journal Of European Society For Hyperthermic Oncology, North American Hyperthermia Group **28**(1), 87–104 (2012).

[174] J.E. Kennedy, G.R. ter Haar, and D. Cranston, High intensity focused ultrasound: surgery of the future?, BJR **76**(909), 590–599 (2003).

[175] K.B. Bader, E. Vlaisavljevich, and A.D. Maxwell, For Whom the Bubble Grows: Physical Principles of Bubble Nucleation and Dynamics in Histotripsy Ultrasound Therapy, Ultrasound in Medicine and Biology **45**(5), 1056–1080 (2019).

[176] T.G. Schuster, J.T. Wei, K. Hendlin, R. Jahnke, and W.W. Roberts, Histotripsy Treatment of Benign Prostatic Enlargement Using the Vortx Rx System: Initial Human Safety and Efficacy Outcomes, Urology **114**, 184–187 (2018).

[177] V.A. Salgaonkar, S. Datta, C.K. Holland, and T.D. Mast, Passive cavitation imaging with ultrasound arrays, J Acoust Soc Am **126**(6), 3071–3083 (2009).

[178] C. Crake, F.C. Meral, M.T. Burgess, I.T. Papademetriou, N.J. McDannold, and T.M. Porter, Combined passive acoustic mapping and magnetic resonance thermometry for monitoring phase-shift nanoemulsion enhanced focused ultrasound therapy, Phys Med Biol **62**(15), 6144–6163 (2017).

[179] C.D. Arvanitis and N. McDannold, Integrated ultrasound and magnetic resonance imaging for simultaneous temperature and cavitation monitoring during focused ultrasound therapies, Med Phys **40**(11), (2013).

[180] W.W. Roberts, Development and Translation of Histotripsy: Current Status and Future Directions, Curr Opin Urol **24**(1), 104–110 (2014).

[181] T.L. Hall, J.B. Fowlkes, and C.A. Cain, A real-time measure of cavitation induced tissue disruption by ultrasound imaging backscatter reduction, IEEE Transactions on Ultrasonics, Ferroelectrics, and Frequency Control **54**(3), 569–575 (2007).

[182] A.D. Maxwell, T.-Y. Wang, L. Yuan, A.P. Duryea, Z. Xu, and C.A. Cain, A tissue phantom for visualization and measurement of ultrasound-induced cavitation damage, Ultrasound Med Biol **36**(12), 2132–2143 (2010).

183 J.T. Sutton, N.M. Ivancevich, S.R. Perrin, D.C. Vela, and C.K. Holland, Clot retraction affects the extent of ultrasound-enhanced thrombolysis in an ex vivo porcine thrombosis model, Ultrasound Med Biol **39**(5), 813–824 (2013).

184 K.P. Mercado-Shekhar, R.T. Kleven, H. Aponte Rivera, *et al.*, Effect of Clot Stiffness on Recombinant Tissue Plasminogen Activator Lytic Susceptibility in Vitro, Ultrasound in Medicine & Biology **44**(12), 2710–2727 (2018).

185 T. Hall, C. Cain, G.T. Clement, N.J. McDannold, and K. Hynynen, A Low Cost Compact 512 Channel Therapeutic Ultrasound System For Transcutaneous Ultrasound Surgery, AIP Conference Proceedings **829**(1), 445–449 (2006).

186 K.B. Bader, K.J. Haworth, H. Shekhar, *et al.*, Efficacy of histotripsy combined with rt-PA in vitro, Phys. Med. Biol. **61**(14), 5253 (2016).

187 A.D. Maxwell, C.A. Cain, T.L. Hall, J.B. Fowlkes, and Z. Xu, Probability of cavitation for single ultrasound pulses applied to tissues and tissue-mimicking materials, Ultrasound Med Biol **39**(3), 449–465 (2013).

188 Z. Xu, T.L. Hall, J.B. Fowlkes, and C.A. Cain, Optical and acoustic monitoring of bubble cloud dynamics at a tissue-fluid interface in ultrasound tissue erosion, J Acoust Soc Am **121**(4), 2421–2430 (2007).

189 K.B. Bader, M.J. Crowe, J.L. Raymond, and C.K. Holland, Effect of Frequency-Dependent Attenuation on Predicted Histotripsy Waveforms in Tissue-Mimicking Phantoms, Ultrasound in Medicine & Biology **42**(7), 1701–1705 (2016).

190 G.P. Liney, A.J. Knowles, D.J. Manton, L.W. Turnbull, S.J. Blackband, and A. Horsman, Comparison of conventional single echo and multi-echo sequences with a fast spin-echo sequence for quantitative T2 mapping: application to the prostate, J Magn Reson Imaging **6**(4), 603–607 (1996).

191 N. Otsu, A Threshold Selection Method from Gray-Level Histograms, IEEE Transactions on Systems, Man, and Cybernetics **9**(1), 62–66 (1979).

192 K. Radhakrishnan, K.J. Haworth, S.-L. Huang, M.E. Klegerman, D.D. McPherson, and C.K. Holland, Stability of echogenic liposomes as a blood pool ultrasound contrast agent in a physiologic flow phantom, Ultrasound Med Biol **38**(11), 1970–1981 (2012).

193 J.A. Hanley and B.J. McNeil, The meaning and use of the area under a receiver operating characteristic (ROC) curve., Radiology **143**(1), 29–36 (1982).

194 C.E. Metz, Basic principles of ROC analysis, Seminars in Nuclear Medicine **8**(4), 283–298 (1978).

195 E.R. DeLong, D.M. DeLong, and D.L. Clarke-Pearson, Comparing the Areas under Two or More Correlated Receiver Operating Characteristic Curves: A Nonparametric Approach, Biometrics **44**(3), 837–845 (1988).

196 W.R. Crum, O. Camara, and D.L.G. Hill, Generalized Overlap Measures for Evaluation and Validation in Medical Image Analysis, IEEE Transactions on Medical Imaging **25**(11), 1451–1461 (2006).

[197] A.D. Maxwell, G. Owens, H.S. Gurm, K. Ives, D.D. Myers, and Z. Xu, Noninvasive Treatment of Deep Venous Thrombosis Using Pulsed Ultrasound Cavitation Therapy (Histotripsy) in a Porcine Model, Journal of Vascular and Interventional Radiology **22**(3), 369–377 (2011).

[198] T.-Y. Wang, Z. Xu, T.L. Hall, J.B. Fowlkes, and C.A. Cain, An efficient treatment strategy for histotripsy by removing cavitation memory, Ultrasound Med Biol **38**(5), 753–766 (2012).

[199] A. Shi, Z. Xu, J. Lundt, H.A. Tamaddoni, T. Worlikar, and T.L. Hall, Integrated Histotripsy and Bubble Coalescence Transducer for Rapid Tissue Ablation, IEEE Transactions on Ultrasonics, Ferroelectrics, and Frequency Control 1–1 (2018).

[200] P. Huber, J. Debus, K. Jöchle, *et al.*, Control of cavitation activity by different shockwave pulsing regimes, Phys. Med. Biol. **44**(6), 1427 (1999).

[201] Z. Xu, T.L. Hall, J.B. Fowlkes, and C.A. Cain, Effects of acoustic parameters on bubble cloud dynamics in ultrasound tissue erosion (histotripsy), J. Acoust. Soc. Am. **122**(1), 229–236 (2007).

[202] P.B. Duncan and D. Needham, Test of the Epstein-Plesset model for gas microparticle dissolution in aqueous media: effect of surface tension and gas undersaturation in solution, Langmuir **20**(7), 2567–2578 (2004).

[203] A. Partanen, N. Farr, W. Kreider, *et al.*, Use of MRI to visualize mechanically fractionated lesions generated by boiling histotripsy in tissue Abstract, in (2014).

[204] D.R. Cox, The Regression Analysis of Binary Sequences, Journal of the Royal Statistical Society. Series B (Methodological) **20**(2), 215–242 (1958).

[205] K.-W. Lin, Y. Kim, A.D. Maxwell, *et al.*, Histotripsy beyond the intrinsic cavitation threshold using very short ultrasound pulses: microtripsy, IEEE Trans Ultrason Ferroelectr Freq Control **61**(2), 251–265 (2014).

[206] P. Stoica, Z. Wang, and J. Li, Robust Capon beamforming, IEEE Signal Processing Letters **10**(6), 172–175 (2003).

[207] C. Coviello, R. Kozick, J. Choi, *et al.*, Passive acoustic mapping utilizing optimal beamforming in ultrasound therapy monitoring, The Journal of the Acoustical Society of America **137**(5), 2573–2585 (2015).

[208] M.A. O'Reilly, R.M. Jones, and K. Hynynen, Three-Dimensional Transcranial Ultrasound Imaging of Microbubble Clouds Using a Sparse Hemispherical Array, IEEE Transactions on Biomedical Engineering **61**(4), 1285–1294 (2014).

[209] J.J. Macoskey, S.W. Choi, T.L. Hall, *et al.*, Using the cavitation collapse time to indicate the extent of histotripsy-induced tissue fractionation, Phys Med Biol **63**(5), 055013 (2018).

[210] J.J. Macoskey, X. Zhang, T.L. Hall, *et al.*, Bubble-Induced Color Doppler Feedback Correlates with Histotripsy-Induced Destruction of Structural Components in Liver Tissue, Ultrasound Med Biol **44**(3), 602–612 (2018).

[211] S.P. Allen, T.L. Hall, C.A. Cain, and L. Hernandez-Garcia, Controlling cavitation-based image contrast in focused ultrasound histotripsy surgery, Magn. Reson. Med. **73**(1), 204–213 (2015).

[212] S.P. Allen, L. Hernandez-Garcia, C.A. Cain, and T.L. Hall, MR-based detection of individual histotripsy bubble clouds formed in tissues and phantoms, Magn. Reson. Med. **76**(5), 1486–1493 (2016).

[213] T.D. Khokhlova, M.S. Canney, D. Lee, *et al.*, Magnetic resonance imaging of boiling induced by high intensity focused ultrasound, J. Acoust. Soc. Am. **125**(4), 2420–2431 (2009).

[214] B. Sahiner, A. Pezeshk, L.M. Hadjiiski, *et al.*, Deep learning in medical imaging and radiation therapy, Med Phys **46**(1), e1–e36 (2019).

[215] G.-Y. Wan, Y. Liu, B.-W. Chen, Y.-Y. Liu, Y.-S. Wang, and N. Zhang, Recent advances of sonodynamic therapy in cancer treatment, Cancer Biol Med **13**(3), 325–338 (2016).

[216] H.-C. Zheng, The molecular mechanisms of chemoresistance in cancers, Oncotarget **8**(35), 59950–59964 (2017).

[217] V. Sini, S. Cinieri, P. Conte, *et al.*, Endocrine therapy in post-menopausal women with metastatic breast cancer: From literature and guidelines to clinical practice, Crit. Rev. Oncol. Hematol. **100**, 57–68 (2016).

[218] H.E. Barker, J.T.E. Paget, A.A. Khan, and K.J. Harrington, The Tumour Microenvironment after Radiotherapy: Mechanisms of Resistance and Recurrence, Nat Rev Cancer **15**(7), 409–425 (2015).

[219] L. Tang, F. Wei, Y. Wu, *et al.*, Role of metabolism in cancer cell radioresistance and radiosensitization methods, J Exp Clin Cancer Res **37**, (2018).

[220] J.B. Ammori, L.M. Colletti, M.M. Zalupski, *et al.*, Surgical resection following radiation therapy with concurrent gemcitabine in patients with previously unresectable adenocarcinoma of the pancreas, J Gastrointest Surg **7**(6), 766–772 (2003).

[221] A.P. McHale, J.F. Callan, N. Nomikou, C. Fowley, and B. Callan, Sonodynamic Therapy: Concept, Mechanism and Application to Cancer Treatment, in *Therapeutic Ultrasound*, edited by J.-M. Escoffre and A. Bouakaz (Springer International Publishing, Cham, 2016), pp. 429–450.

[222] P. Riesz and T. Kondo, Free radical formation induced by ultrasound and its biological implications, Free Radical Biology and Medicine **13**(3), 247–270 (1992).

[223] P. Riesz, D. Berdahl, and C.L. Christman, Free radical generation by ultrasound in aqueous and nonaqueous solutions., Environ Health Perspect **64**, 233–252 (1985).

[224] S. Umemura, N. Yumita, R. Nishigaki, and K. Umemura, Mechanism of cell damage by ultrasound in combination with hematoporphyrin, Jpn. J. Cancer Res. **81**(9), 962–966 (1990).

[225] Y. Harada, K. Ogawa, Y. Irie, *et al.*, Ultrasound activation of TiO2 in melanoma tumors, J Control Release **149**(2), 190–195 (2011).

[226] J. Rooze, Cavitation in gas-saturated liquids, (2012).

[227] S. Hilgenfeldt, S. Grossmann, and D. Lohse, Sonoluminescence light emission, Physics of Fluids **11**(6), 1318–1330 (1999).

[228] A. Fujishima, X. Zhang, and D.A. Tryk, TiO2 photocatalysis and related surface phenomena, Surface Science Reports **63**(12), 515–582 (2008).

[229] C. McEwan, J. Owen, E. Stride, *et al.*, Oxygen carrying microbubbles for enhanced sonodynamic therapy of hypoxic tumours, J Control Release **203**, 51–56 (2015).

[230] P. Yuan and D. Song, MRI tracing non-invasive TiO2-based nanoparticles activated by ultrasound for multi-mechanism therapy of prostatic cancer, Nanotechnology **29**(12), 125101 (2018).

[231] E. Vlaisavljevich, Y.Y. Durmaz, A. Maxwell, M. ElSayed, and Z. Xu, Nanodroplet-Mediated Histotripsy for Image-guided Targeted Ultrasound Cell Ablation, Theranostics **3**(11), 851–864 (2013).

[232] G.J. Anthony, V. Bollen, S. Hendley, T. Antic, S. Sammet, and K.B. Bader, Assessment of histotripsy-induced liquefaction with diagnostic ultrasound and magnetic resonance imaging *in vitro* and *ex vivo*, Phys Med Biol (2019).

[233] T.J. Mason, J.P. Lorimer, D.M. Bates, and Y. Zhao, Dosimetry in sonochemistry: the use of aqueous terephthalate ion as a fluorescence monitor, Ultrasonics Sonochemistry **1**(2), S91–S95 (1994).

[234] A.D. Maxwell, P.V. Yuldashev, W. Kreider, *et al.*, A Prototype Therapy System for Transcutaneous Application of Boiling Histotripsy, IEEE Transactions on Ultrasonics, Ferroelectrics, and Frequency Control **64**(10), 1542–1557 (2017).

[235] L. Villeneuve, L. Alberti, J.-P. Steghens, J.-M. Lancelin, and J.-L. Mestas, Assay of hydroxyl radicals generated by focused ultrasound, Ultrasonics Sonochemistry **16**(3), 339–344 (2009).

[236] G.J. Price, F.A. Duck, M. Digby, W. Holland, and T. Berryman, Measurement of radical production as a result of cavitation in medical ultrasound fields, Ultrason Sonochem **4**(2), 165–171 (1997).

[237] K.B. Bader, S. Hendley, G.J. Anthony, and V. Bollen, Observation and modulation of the dissolution of histotripsy-induced bubble clouds with high-frame rate plane wave imaging, Phys. Med. Biol. (2019).

[238] Q. Tang, J. Cui, Z. Tian, *et al.*, Oxygen and indocyanine green loaded phase-transition nanoparticle-mediated photo-sonodynamic cytotoxic effects on rheumatoid arthritis fibroblast-like synoviocytes, Int J Nanomedicine **12**, 381–393 (2017).

[239] Z. Li, J. Han, L. Yu, *et al.*, Synergistic Sonodynamic/Chemotherapeutic Suppression of Hepatocellular Carcinoma by Targeted Biodegradable Mesoporous Nanosonosensitizers, Advanced Functional Materials **28**(26), 1800145 (2018).

[240] J.J. Kwan, R. Myers, C.M. Coviello, *et al.*, Ultrasound-Propelled Nanocups for Drug Delivery, Small **11**(39), 5305–5314 (2015).

[241] V. Belova, D.A. Gorin, D.G. Shchukin, and H. Möhwald, Controlled Effect of Ultrasonic Cavitation on Hydrophobic/Hydrophilic Surfaces, ACS Appl. Mater. Interfaces **3**(2), 417–425 (2011).

[242] G. Canavese, A. Ancona, L. Racca, *et al.*, Nanoparticle-assisted ultrasound: A special focus on sonodynamic therapy against cancer, Chem Eng J **340**, 155–172 (2018).

[243] F. Winterroth, Z. Xu, T.-Y. Wang, *et al.*, Examining and Analyzing Subcellular Morphology of Renal Tissue Treated by Histotripsy, Ultrasound in Medicine & Biology **37**(1), 78–86 (2011).

[244] A. Kosar, M. Sesen, O. Oral, Z. Itah, and D. Gozuacik, Bubbly Cavitating Flow Generation and Investigation of Its Erosional Nature for Biomedical Applications, IEEE Transactions on Biomedical Engineering **58**(5), 1337–1346 (2011).

[245] W. Hiraoka, H. Honda, L.B. Feril, N. Kudo, and T. Kondo, Comparison between sonodynamic effect and photodynamic effect with photosensitizers on free radical formation and cell killing, Ultrasonics Sonochemistry **13**(6), 535–542 (2006).

[246] I. Rosenthal, J.Z. Sostaric, and P. Riesz, Sonodynamic therapy—a review of the synergistic effects of drugs and ultrasound, Ultrasonics Sonochemistry **11**(6), 349–363 (2004).

[247] H. Ma, A. Brennan, and S.A. Diamond, Photocatalytic reactive oxygen species production and phototoxicity of titanium dioxide nanoparticles are dependent on the solar ultraviolet radiation spectrum, Environmental Toxicology and Chemistry **31**(9), 2099–2107 (2012).

[248] D. Srinivasan and L.V. Holroyd, Optical Spectrum of the Sonoluminescence Emitted by Cavitated Water, Journal of Applied Physics **32**(3), 446–449 (1961).

[249] J. Wang, Y. Guo, B. Liu, *et al.*, Detection and analysis of reactive oxygen species (ROS) generated by nano-sized TiO2 powder under ultrasonic irradiation and application in sonocatalytic degradation of organic dyes, Ultrason Sonochem **18**(1), 177–183 (2011).

[250] K.B. Bader and V. Bollen, The influence of gas diffusion on bubble persistence in shock-scattering histotripsy, J Acoust Soc Am **143**(6), EL481–EL486 (2018).

[251] T. Tuziuti, S. Hatanaka, K. Yasui, T. Kozuka, and H. Mitome, Influence of dissolved oxygen content on multibubble sonoluminescence with ambient-pressure reduction, Ultrasonics **40**(1–8), 651–654 (2002).

[252] A. Carreau, B.E. Hafny-Rahbi, A. Matejuk, C. Grillon, and C. Kieda, Why is the partial oxygen pressure of human tissues a crucial parameter? Small molecules and hypoxia, J Cell Mol Med **15**(6), 1239–1253 (2011).

[253] K.B. Bader, The influence of medium elasticity on the prediction of histotripsy-induced bubble expansion and erythrocyte viability, Phys. Med. Biol. **63**(9), 095010 (2018).

[254] J. Wang, J. Wu, Z. Zhang, *et al.*, Sonocatalytic damage of bovine serum albumin (BSA) in the presence of nanometer anatase titanium dioxide (TiO2), Ultrasound in Medicine & Biology **32**(1), 147–152 (2006).

[255] J. Wang, B. Guo, X. Zhang, Z. Zhang, J. Han, and J. Wu, Sonocatalytic degradation of methyl orange in the presence of TiO2 catalysts and catalytic activity comparison of rutile and anatase, Ultrasonics Sonochemistry **12**(5), 331–337 (2005).

[256] Y. Guo, C. Cheng, J. Wang, *et al.*, Detection of reactive oxygen species (ROS) generated by TiO2(R), TiO2(R/A) and TiO2(A) under ultrasonic and solar light irradiation and application in degradation of organic dyes, Journal of Hazardous Materials **192**(2), 786–793 (2011).

[257] M. Buchalska, M. Kobielusz, A. Matuszek, M. Pacia, S. Wojtyła, and W. Macyk, On Oxygen Activation at Rutile- and Anatase-TiO2, ACS Catal. **5**(12), 7424–7431 (2015).

[258] V. Bolis, C. Busco, M. Ciarletta, *et al.*, Hydrophilic/hydrophobic features of TiO2 nanoparticles as a function of crystal phase, surface area and coating, in relation to their potential toxicity in peripheral nervous system, Journal of Colloid and Interface Science **369**(1), 28–39 (2012).

[259] F. Pellegrino, L. Pellutiè, F. Sordello, *et al.*, Influence of agglomeration and aggregation on the photocatalytic activity of TiO2 nanoparticles, Applied Catalysis B: Environmental **216**, 80–87 (2017).

[260] S.S. Mano, K. Kanehira, S. Sonezaki, and A. Taniguchi, Effect of Polyethylene Glycol Modification of TiO2 Nanoparticles on Cytotoxicity and Gene Expressions in Human Cell Lines, Int J Mol Sci **13**(3), 3703–3717 (2012).

[261] D. Selli and C.D. Valentin, Ab Initio Investigation of Polyethylene Glycol Coating of TiO2 Surfaces, J Phys Chem C Nanomater Interfaces **120**(51), 29190–29201 (2016).

[262] J. Yu, W. Wang, B. Cheng, and B.-L. Su, Enhancement of Photocatalytic Activity of Mesporous TiO2 Powders by Hydrothermal Surface Fluorination Treatment, J. Phys. Chem. C **113**(16), 6743–6750 (2009).

[263] K.K. Griendling, R.M. Touyz, J.L. Zweier, *et al.*, Measurement of Reactive Oxygen Species, Reactive Nitrogen Species, and Redox-Dependent Signaling in the Cardiovascular System: A Scientific Statement From the American Heart Association, Circ. Res. **119**(5), e39-75 (2016).

[264] Y.T. Didenko, D.N. Nastich, S.P. Pugach, Y.A. Polovinka, and V.I. Kvochka, The effect of bulk solution temperature on the intensity and spectra of water sonoluminescence, Ultrasonics **32**(1), 71–76 (1994).

[265] Y. Wang, Y. Liu, H. Wu, J. Zhang, Q. Tian, and S. Yang, Functionalized Holmium-Doped Hollow Silica Nanospheres for Combined Sonodynamic and Hypoxia-Activated Therapy, Advanced Functional Materials **29**(3), 1805764 (2019).

[266] M. de Smet, S. Langereis, S. van den Bosch, and H. Grüll, Temperature-sensitive liposomes for doxorubicin delivery under MRI guidance, J Control Release **143**(1), 120–127 (2010).

[267] H. Wei, O.T. Bruns, M.G. Kaul, *et al.*, Exceedingly small iron oxide nanoparticles as positive MRI contrast agents, Proc Natl Acad Sci U S A **114**(9), 2325–2330 (2017).

[268] K.B. Ghaghada, M. Ravoori, D. Sabapathy, J. Bankson, V. Kundra, and A. Annapragada, New dual mode gadolinium nanoparticle contrast agent for magnetic resonance imaging, PLoS ONE **4**(10), e7628 (2009).

[269] D.R. Messroghli, A. Radjenovic, S. Kozerke, D.M. Higgins, M.U. Sivananthan, and J.P. Ridgway, Modified Look-Locker inversion recovery (MOLLI) for high-resolution T1 mapping of the heart, Magn Reson Med **52**(1), 141–146 (2004).

[270] S. Giri, Y.-C. Chung, A. Merchant, *et al.*, T2 quantification for improved detection of myocardial edema, J Cardiovasc Magn Reson **11**, 56 (2009).